VELOCITY ANALYSIS FOR LATERALLY HETEROGENEOUS ANISOTROPIC MEDIA

by

Andrés Pech

A thesis submitted to the Faculty and the Board of Trustees of the Colorado School of Mines in partial fulfillment of the requirements for the degree of Doctor of Philosophy (Geophysics).

Golden, Colorado

Date _____

Signed: _____
Andrés Pech

Approved: _____
Dr. Ilya Tsvankin
Professor of Geophysics
Thesis Advisor

Golden, Colorado

Date _____

_____
Dr. Terence K. Young
Professor and Head
Department of Geophysics

ABSTRACT

Oil, gas, and geothermal reservoirs, and overlying strata are often composed of anisotropic rocks. Proper treatment of anisotropy during the processing of seismic data not only helps to avoid distortions in reservoir imaging, but also provides estimates of the anisotropic coefficients, which carry valuable information about lithology and fracture networks. Accurate estimation of the velocity model is one of the most difficult steps in imaging of seismic data from anisotropic media.

Here, I introduce a velocity-analysis method for anisotropic models that can be called *stacking-velocity tomography*. This technique is designed to invert normal-moveout (NMO) ellipses, zero-offset traveltimes, and reflection time slopes of P- and S-waves for interval anisotropic parameters and shapes of reflection interfaces. Examination of a wide range of anisotropic models makes it possible to establish the conditions needed for stable parameter estimation.

Results here show that, in many cases, it is possible to build anisotropic velocity models from azimuthally-varying hyperbolic moveouts of P- and S-waves alone. For example, the inversion of P-wave NMO velocities makes it possible to estimate the anisotropic parameters of a physical model that includes a bending transversely isotropic (TI) layer with a tilted symmetry axis. However, there are some notable exceptions such as horizontally layered orthorhombic and TI media with vertical axis of symmetry, for which anisotropic parameter estimation requires independent knowledge of the vertical velocities or reflector depth.

I also present a general analytic expression for the quartic moveout coefficient A_4 that is responsible for the magnitude of nonhyperbolic moveout of pure (non-converted) modes. This expression takes into account reflection-point dispersal on irregular interfaces and is valid for arbitrarily anisotropic, heterogeneous media. All quantities needed to compute A_4 can be evaluated during the tracing of a single (zero-offset) ray, so long-spread moveout can be modeled without time-consuming multi-offset, multi-azimuth ray tracing. Analysis of the azimuthal dependence of A_4 for tilted TI media shows that P-wave nonhyperbolic moveout can help to constrain the orientation of the symmetry axis.

TABLE OF CONTENTS

LIST OF FIGURES

ACKNOWLEDGMENTS

I wish to thank my thesis advisor, Ilya Tsvankin, and my committee members, Vladimir Grechka, Catherine Skokan, John Scales, Max Peeters and John Warme for their advice and support. I would like to extend my thanks to CONACYT and the Center for Wave Phenomena (CWP) for funding my work.

I am greatly indebted to my advisor Ilya Tsvankin for his support and guidance during my studies.

I would like to acknowledge the guidance I received from Vladimir Grechka during the first three years of my studies.

I thank John Scales for teaching me inverse theory.

I would like to express my gratitude to Max Peeters for helping me to understand the link between petrophysics and seismic exploration.

I would like to extend my thanks to John Warme for helping me to understand the links among geology, petroleum engineering, and seismic exploration.

I would like to thank Ken Larner for giving me the opportunity to be a member of the Center for Wave Phenomena.

Special thanks go to Sergey Fomel and Andreas Rüger for their many useful comments about nonhyperbolic moveout.

Thanks also go to Marty Terrell for reviewing this thesis.

I wish to thank my wife, Aida Alejandra, and my daughter, Aida Andrea, for their unconditional support.

Finally, I thank my parents and brother for supporting me throughout my studies.

Chapter 1

INTRODUCTION

Proper treatment of vertical transverse isotropy (VTI), the most commonly used anisotropic model for sedimentary basins, can be important in velocity analysis and imaging of reflection data. The kinematics of P-waves in VTI media is controlled by the vertical velocity V_{P0} and Thomsen's (1986) anisotropic coefficients ϵ and δ (Tsvankin, 1996); the parameter δ governs the kinematics of P-waves near the symmetry axis, and the parameter ϵ controls P-wave propagation away from the symmetry axis. Estimation of these parameters from reflection data is a major problem in building accurate velocity models for seismic imaging.

Inversion of P-wave data in VTI media has been addressed in a number of recent publications, including Bube and Meadows (1997), Grechka and Tsvankin (1998a), Bartel et al. (1998), Le Stunff and Grenié (1998), Le Stunff and Jeannot (1998), and Sexton and Williamson (1998). *Time-domain* imaging for vertical transverse isotropy is largely based on the result of Alkhalifah and Tsvankin (1995), who proved that P-wave reflection traveltimes in laterally homogeneous VTI media above a dipping interface depend on just two parameters – the normal-moveout (NMO) velocity from a horizontal (zero-dip) reflector,

$$V_{\rm nmo}(0) = V_{P0}\sqrt{1+2\,\delta}\,, \tag{1.0.1}$$

and the anellipticity coefficient,

$$\eta \equiv \frac{\epsilon - \delta}{1 + 2\,\delta}\,. \tag{1.0.2}$$

Whereas $V_{\rm nmo}(0)$ and η provide enough information for time processing, they are insufficient for resolving the vertical velocity V_{P0} and reflector depth. Therefore, surface P-wave data do not constrain the depth scale in VTI media, needed, for example, in prestack depth migration.

The two-parameter description of P-wave time-domain signatures, however, breaks down in the presence of lateral heterogeneity above the reflector (Alkhalifah et al., 1998; Grechka and Tsvankin, 1999b). Grechka and Tsvankin (2002a) developed a Dix-type averaging procedure for NMO velocities in laterally heterogeneous anisotropic media and applied it to moveout analysis for vertical transverse isotropy. Their results show that the NMO velocity of reflected P–arrivals that cross dipping intermediate interfaces depends on the individual values of V_{P0}, ϵ, and δ, rather than just on the combinations $V_{\rm nmo}(0)$ and η. Le Stunff et al. (2001) presented an example of successful inversion of P-wave traveltimes for the parameters V_{P0}, ϵ, and δ in a model that included a dipping VTI layer overlying a purely isotropic medium. The inversion becomes much better constrained if P-waves are combined with S- or PS-waves. Here, I develop a methodology for velocity analysis of combined P- and S-wave data in laterally heterogeneous anisotropic media.

Chapter 2 introduces stacking-velocity tomography for P-wave data in VTI models composed of homogeneous layers separated by plane dipping interfaces. The analysis shows that 3-D wide-azimuth P-wave moveout data from N non-intersecting interfaces constrain up to $3N - 1$ combinations of the interval parameters $V_{P0,n}$, ϵ_n,

δ_n, where $n = 1, \ldots, N$. Hence, to determine the interval values $V_{P0,n}$, ϵ_n, and δ_n uniquely and reconstruct the model in depth, at least one of the parameters has to be known *a priori*. The inversion is generally better posed if the subsurface contains faults or if the interfaces are curved (but the layers are still homogeneous).

Chapter 3 includes an extension of the theory of NMO-velocity surfaces (Grechka and Tsvankin, 1998b) to anisotropic media with irregular interfaces. I employ singular value decomposition and actual inversion (stacking-velocity tomography) of P-wave reflection data to show that, for some VTI models with smooth curved interfaces, parameter estimation in depth using P-wave traveltimes can be accomplished without any *a priori* information.

Chapter 4 extends the anisotropic velocity analysis to multicomponent data. A number of previous case studies involving multicomponent land and offshore data demonstrated that mode (P-to-S) conversions can supplement or even replace pure-mode reflections in such applications as imaging beneath gas clouds (e.g., Granli et al., 1999; Thomsen, 1999) and characterization of fractured reservoirs (e.g., Pérez et al., 1999). Processing of PS-waves, however, is complicated by the strong influence of seismic anisotropy on their signatures. For example, the velocity anisotropy of SV- and PSV-waves in TI media is controlled mostly by the coefficient

$$\sigma \equiv \left(\frac{V_{P0}}{V_{S0}}\right)^2 (\epsilon - \delta)\,, \tag{1.0.3}$$

which is typically much larger than the parameters ϵ and δ governing P-wave data (V_{P0} and V_{S0} are the vertical P- and S-wave velocities, respectively). Mis-ties between PP and PS sections routinely produced by conventional isotropic imaging methods (e.g., Nolte et al., 1999) indicate the need for joint anisotropic velocity analysis of

PP and PS reflection events.

As shown by Tsvankin and Grechka (2000, 2002) for TI media with a vertical symmetry axis (VTI), wide-azimuth reflection traveltimes of PP - and PSV-waves from a single mildly dipping reflector are sufficient for estimating all relevant parameters (V_{P0}, V_{S0}, ϵ, and δ). If the reflector is horizontal, however, joint inversion of PP and PSV moveout data is nonunique, even if uncommonly long offsets are available (Grechka and Tsvankin, 2002c).

Chapter 4 introduces the methodology of anisotropic multicomponent stacking-velocity tomography and describes its application to TI media with an arbitrary tilt of the symmetry axis. Rather than working with PS data directly, I combine them with PP data to compute the traveltimes of the pure SS (SV or SH for TI media) reflections from the same interface using the algorithm of Grechka and Tsvankin (2002b). The reconstruction of SS traveltimes is entirely data-driven and does not require precise knowledge of the velocity model. This procedure makes it possible to avoid inherent problems of PS-wave velocity analysis caused by the asymmetry of PS moveout with respect to zero offset on CMP (common-midpoint) and CCP (common-conversion-point) gathers, conversion-point dispersal, and polarity reversals.

In contrast to the more complicated moveout of mode conversions, reflection traveltime of pure SS-waves is symmetric with respect to zero offset and, for moderate offset-to-depth ratios, can be described by the NMO ellipse (Grechka and Tsvankin, 1998b). Hence, the theory of the NMO ellipses and NMO-velocity surfaces (Grechka and Tsvankin, 2002a) is directly applicable to SS-wave moveout.

The tomographic algorithm operates with the NMO ellipses, zero-offset traveltimes, and reflection slopes (measured on zero-offset time sections) of PP-waves and the

reconstructed SS-waves. I examine a wide range of homogeneous TI models with a tilted symmetry axis and establish the conditions needed for stable parameter estimation. Then I apply the method to layered TI models to estimate the interval medium parameters and the shapes of interfaces from multicomponent reflection data.

Chapter 5 discusses anisotropic parameter estimation for a physical model that contains a bending transversely isotropic shale layer with the symmetry axis orthogonal to the layer's boundaries. This physical model was built by Leslie and Lawton (1996) to simulate typical reflection data acquired in overthrust areas of the Alberta Foothills in Canada. Several recent publications demonstrated that the presence of TTI (transverse isotropy with tilted symmetry axis) formations in overthrust areas may cause serious problems in imaging of exploration targets. Ignoring the influence of transverse isotropy and applying conventional velocity-analysis and migration techniques leads to mispositioning of reflectors beneath TTI layers and inferior quality of seismic sections (Leslie and Lawton, 1996, 1998; Vestrum et al., 1999). Vestrum et al. (1999) showed on both model and field data that higher-quality images of both dipping and horizontal features in the overthrust environment are produced by migration algorithms capable of handling TTI media. The main difficulty, however, is in evaluating the anisotropic parameters from surface reflection data, especially in structurally complex areas. Using the general theory of normal moveout in laterally heterogeneous media developed by Grechka and Tsvankin (2002a), I demonstrate that P-wave NMO velocities and zero-offset traveltimes can be inverted for the full set of the anisotropic parameters of the TTI layer. Information about the anisotropic parameter ϵ is contained in the moveout of a reflected wave that crosses one of the dipping TI blocks.

Chapter 6 describes an extension of stacking-velocity tomography to more compli-

cated orthorhombic media believed to be typical for naturally fractured oil and gas reservoirs (Schoenberg and Helbig, 1997; Bakulin et al., 2000). Wide-azimuth reflection traveltimes of PP-waves and two split converted waves (PS_1 and PS_2) are shown to be sufficient for constraining the anisotropic parameters for a relatively wide range of orthorhombic models. First, I establish the conditions needed to estimate the vertical velocities and Tsvankin's (1997c) anisotropic coefficients of a single dipping orthorhombic layer and, therefore, fully reconstruct this model in the depth domain. Then, I proceed with parameter estimation for orthorhombic media composed of multiple homogeneous layers separated by plane or curved interfaces. Numerical tests indicate that although for a certain class of such layered models the inversion of multicomponent data is theoretically possible, it may not be sufficiently stable. *A priori* constraints on the vertical velocities help to reduce the errors in the estimated anisotropic coefficients.

Chapter 7 is devoted to an analytic description of P-wave long-spread moveout in TI media with an arbitrary orientation of the symmetry axis. In conventional seismic data processing, reflection moveout of pure modes is typically assumed to be hyperbolic, at least for spreadlengths not exceeding reflector depth. However, the presence of heterogeneity (either lateral or vertical) or anisotropy causes deviations from hyperbolic moveout that sometimes cannot be ignored even for offsets-to-depth ratios smaller than unity (e.g., Al-Dajani and Tsvankin, 1998). Insufficient understanding of nonhyperbolic moveout and practical difficulties in analyzing long-offset data often force seismic processors to mute out the nonhyperbolic portion of the moveout curve. Long-spread moveout, however, has proved to be useful in a number of applications, such as anisotropic parameter estimation, suppression of multiples, and large-angle AVO analysis.

A detailed overview of existing results on nonhyperbolic moveout analysis in anisotropic media can be found in Tsvankin (2001). Most earlier work on the contribution of anisotropy to long-spread moveout (e.g., Hake et al., 1984; Byun and Corrigan, 1990; Muir et al., 1993) is restricted to transversely isotropic models with a vertical symmetry axis (VTI). Tsvankin and Thomsen (1994) developed a general nonhyperbolic moveout equation based on the normal-moveout (NMO) velocity V_{nmo} and the quartic moveout coefficient A_4 of the $t^2(x^2)$–function. In contrast to the conventional Taylor series, the Tsvankin-Thomsen equation converges at offsets approaching infinity, which ensures its high accuracy in the intermediate offset range (i.e., for offsets two to three times the reflector depth) important in reflection seismology. A particularly convenient form of this equation for P-waves in VTI media was suggested by Alkhalifah and Tsvankin (1995). The equation of Alkhalifah and Tsvankin (1995) has been widely used for estimating the parameter η from P-wave long-spread traveltimes (e.g., Alkhalifah, 1997; Toldi et al., 1999).

The behavior of nonhyperbolic moveout becomes much more complicated if the medium is azimuthally anisotropic. Al-Dajani and Tsvankin (1998) derived the quartic moveout coefficient for TI media with a horizontal symmetry axis (HTI) and extended the Tsvankin-Thomsen equation to horizontally layered HTI media. A different method based on spherical harmonics was employed by Sayers and Ebrom (1997) to describe long-spread P-wave moveout in an azimuthally anisotropic layer. None of these schemes works in the presence of reflection-point dispersal.

Non-vertical symmetry axis creates an azimuthally anisotropic model without a horizontal symmetry plane, where nonhyperbolic moveout is influenced by reflection-point dispersal. I present analytic expressions for the quartic moveout term for both horizontal and dipping reflectors and study the azimuthal dependence of nonhyperbolic

moveout as a function of reflector dip and symmetry-axis orientation. Strong azimuthal variations of nonhyperbolic moveout (e.g., it completely vanishes in certain azimuthal directions) may be used to constrain anisotropic parameter-estimation algorithms operating with wide-azimuth reflection traveltimes.

Chapter 2

PARAMETER ESTIMATION IN LAYERED VTI MEDIA WITH PLANE DIPPING INTERFACES

2.1 Analytic background

2.1.1 VTI model and data for inversion

Consider a model composed of N homogeneous VTI layers (some of them may be isotropic) separated by plane dipping non-intersecting interfaces (Figure 2.1). The model parameters responsible for P-wave kinematics include the interval vertical velocities $V_{P0,n}$, anisotropic coefficients ϵ_n and δ_n, and the interface dips ϕ_n, azimuths ψ_n, and depths z_n, (for example, under the coordinate origin **O**). Thus, the model vector

$$\mathbf{m} \equiv \{V_{P0,n},\, \epsilon_n,\, \delta_n,\, \phi_n,\, \psi_n,\, z_n\}\,, \quad (n = 1, \ldots, N) \tag{2.1.1}$$

is characterized by $6N$ independent quantities. It is convenient to split the vector $\mathbf{m}$ into two vectors $\mathbf{l}$ and $\mathbf{i}$, where $\mathbf{l}$ contains the layer parameters,

$$\mathbf{l} \equiv \{V_{P0,n},\, \epsilon_n,\, \delta_n\}\,, \quad (n = 1, \ldots, N)\,, \tag{2.1.2}$$

and $\mathbf{i}$ describes the interfaces,

$$\mathbf{i} \equiv \{\phi_n,\, \psi_n,\, z_n\}\,, \quad (n = 1,\, \ldots,\, N)\,. \tag{2.1.3}$$

Clearly, each vector ($\mathbf{l}$ and $\mathbf{i}$) has $3N$ components.

Velocity analysis of 3-D multi-azimuth P-wave data recorded at common midpoints (CMP) with coordinates $\mathbf{Y} = [Y_1,\, Y_2]$ provides estimates of the one-way zero-offset reflection traveltimes $\tau_0(\mathbf{Y},\, n)$ from all interfaces and the corresponding NMO velocities $V_{\rm nmo}(\alpha)$, where α is the azimuth. Azimuthally-dependent NMO velocity of any pure mode is described by an ellipse that can be expressed in terms of the 2×2 symmetric matrix $\mathbf{W}$ (Grechka and Tsvankin, 1998b):

$$V_{\rm nmo}^{-2}(\alpha) = W_{11} \cos^2\alpha + 2\, W_{12} \sin\alpha \cos\alpha + W_{22} \sin^2\alpha\,, \tag{2.1.4}$$

where

$$W_{ij} = \tau_0 \left.\frac{\partial^2 \tau}{\partial x_i \partial x_j}\right|_{\mathbf{Y}} = \tau_0 \left.\frac{\partial p_i}{\partial x_j}\right|_{\mathbf{Y}}\,, \qquad (i, j = 1, 2)\,. \tag{2.1.5}$$

Here $\tau(x_1,\, x_2)$ is the one-way traveltime from the zero-offset reflection point to the location $\mathbf{x}\,\{x_1,\, x_2\}$ at the surface, τ_0 is the one-way zero-offset traveltime, and p_i are the components of the slowness vector corresponding to the ray recorded at the point $\mathbf{x}$.

The matrices $\mathbf{W}(\mathbf{Y},\, n)$ can be obtained from azimuthal velocity analysis based on the hyperbolic moveout equation, parameterized by the NMO ellipse, as described by Grechka and Tsvankin (1999b). From zero-offset (or stacked) time sections, one can pick the slopes of the reflection events, thus giving estimates of the ray parameters $\mathbf{p}(\mathbf{Y},\, n) = [p_1(\mathbf{Y},\, n),\, p_2(\mathbf{Y},\, n)]$ of the zero-offset ray for reflector n.

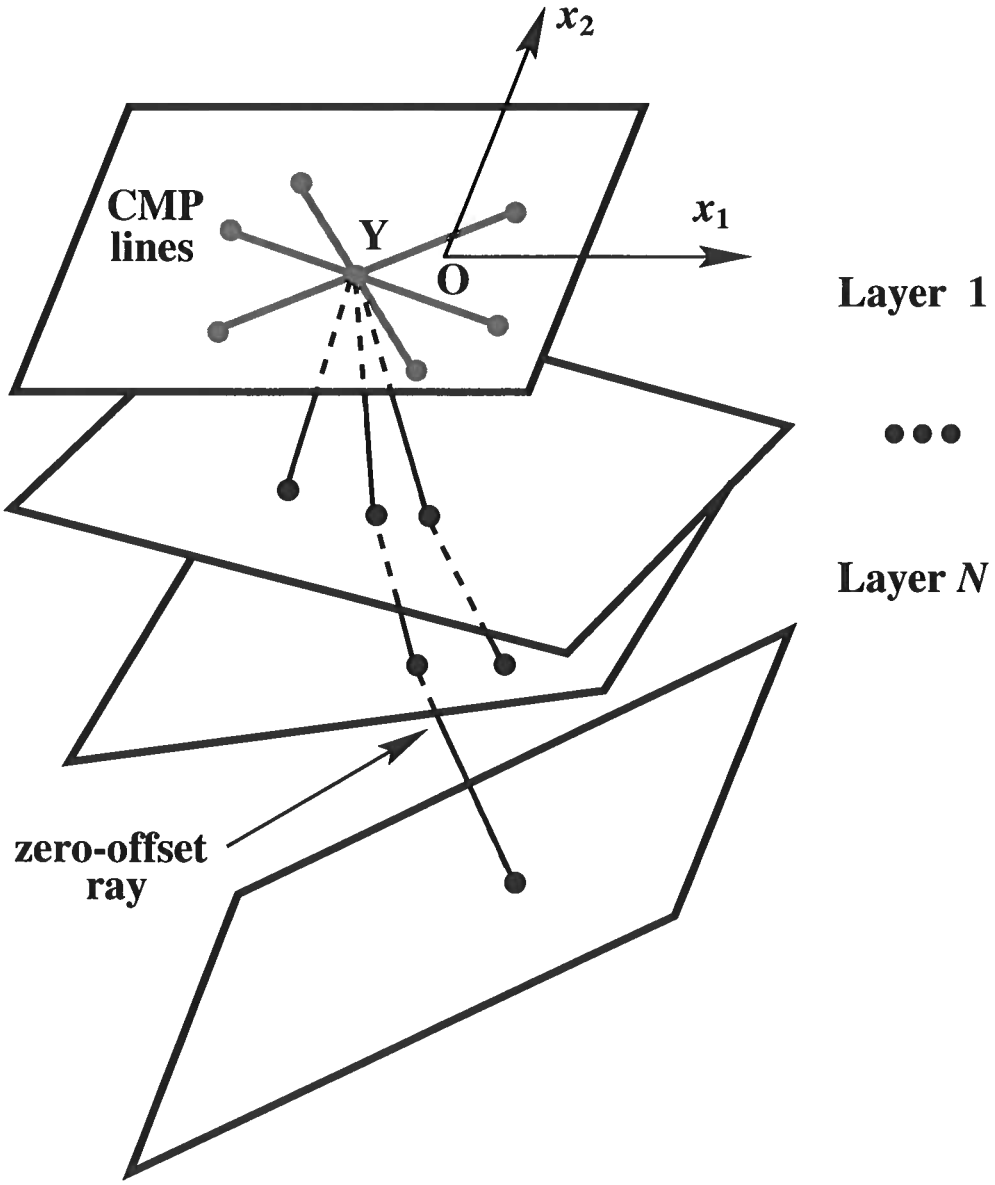

FIG. 2.1. Schematic depiction of zero-offset raypaths for a stack of VTI layers separated by plane dipping interfaces.

Since the layers in the model are homogeneous and the interfaces are plane (Figure 2.1), the slowness components $p_1(\mathbf{Y}, n)$, $p_2(\mathbf{Y}, n)$ are independent of the CMP coordinate $\mathbf{Y}$. Taking into account that

$$\frac{\partial \tau_0(\mathbf{Y}, n)}{\partial Y_j} = p_j(n)\,, \quad (j = 1, 2)\,, \tag{2.1.6}$$

we can express the zero-offset traveltimes $\tau_0(\mathbf{Y}, n)$ as *linear* functions of Y_j:

$$\tau_0(\mathbf{Y}, n) = \tau_0(\mathbf{O}, n) + p_1(n)\, Y_1 + p_2(n)\, Y_2\,. \tag{2.1.7}$$

Here $\tau_0(\mathbf{O}, n)$ are the traveltimes recorded at the coordinate origin $\mathbf{O}$. Using equation (2.1.7), the input traveltime data $\mathbf{d}(\mathbf{Y}, n)$ can be represented as

$$\mathbf{d}(\mathbf{Y}, n) \equiv \{\tau_0(\mathbf{O}, n),\, p_1(n),\, p_2(n),\, W_{11}(\mathbf{Y}, n),\, W_{12}(\mathbf{Y}, n),\, W_{22}(\mathbf{Y}, n)\}\,, \tag{2.1.8}$$

where $n = 1, \ldots, N$.

The feasibility of the inversion for $\mathbf{m}$ is controlled by the character of the spatial variation of the effective NMO ellipses $\mathbf{W}(\mathbf{Y}, n)$.

2.1.2 Effective NMO ellipse

In the model treated here (Figure 2.1), zero-offset ray trajectories from the same interface are parallel to each other at different CMP locations $\mathbf{Y}$. As a result, the interval slownesses, group-velocity vectors, and the matrices $\mathbf{W}_n$ are independent of the CMP coordinate $\mathbf{Y}$, whereas the interval traveltimes $\tau_{0,n}(\mathbf{Y})$ are *linear* functions of $\mathbf{Y}$. Therefore, the difference between the NMO ellipses $\mathbf{W}(\mathbf{O}, n)$ and $\mathbf{W}(\mathbf{Y}, n)$

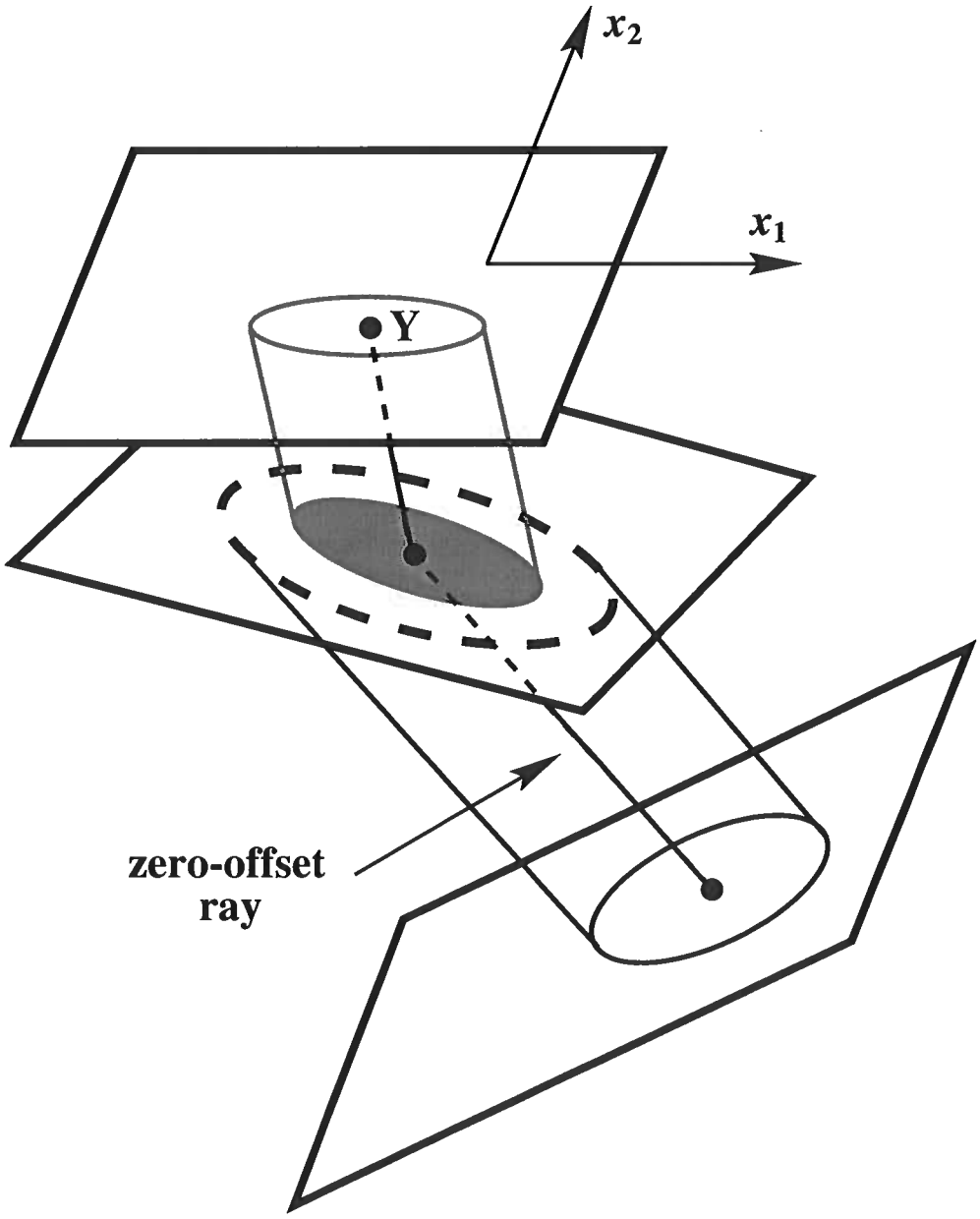

FIG. 2.2. The generalized Dix-type formula averages the intersections of the interval NMO-velocity cylinders with the model interfaces along the zero-offset raypath.

measured at points $\mathbf{O}$ and $\mathbf{Y}$ has a purely geometric nature related to the variations in the length of the interval ray segments. This suggests that the dependence of $\mathbf{W}(\mathbf{Y}, n)$ on $\mathbf{Y}$ provides no information about the model parameters not contained in the NMO ellipses $\mathbf{W}(\mathbf{O}, n)$. This statement is supported by numerical results below.

Thus, the data vector (2.1.8) can be written as

$$\mathbf{d}(\mathbf{Y}, n) = \{\mathbf{d}(\mathbf{O}, n), \mathbf{Y} - \mathbf{O}\}. \tag{2.1.9}$$

2.2 Feasibility of parameter estimation

It is clear from equation (2.1.9) that although traveltime data from different common midpoints may be useful in practice to suppress noise, they give the same information about the medium parameters as the data vector

$$\mathbf{d}(\mathbf{O}, n) = \{\tau_0(\mathbf{O}, n), \mathbf{p}(n), \mathbf{W}(\mathbf{O}, n)\} \tag{2.2.10}$$

at any single CMP. Thus, analyzing the dependence of the vector $\mathbf{d}(\mathbf{O}, n)$ on the parameter vector $\mathbf{m}$ [equation (2.1.1)] should be sufficient for evaluating the feasibility of the inversion. For brevity, henceforth the CMP coordinate will be omitted.

For an N-layered VTI model, the vectors $\mathbf{d}$ (data) and $\mathbf{m}$ (model) contain $6N$ components each. Therefore, the vector $\mathbf{m}$ can be obtained from the data $\mathbf{d}$ only if all components of $\mathbf{d}$ are independent. Unfortunately, this is not the case for VTI media. The P-wave NMO ellipse $\mathbf{W}(1)$ from a dipping reflector overlaid by a homogeneous VTI medium provides only two equations for the medium parameters because its orientation is fixed by the reflector azimuth ψ_1 (Grechka and Tsvankin, 1998b):

$$\tan\psi_1 = \frac{p_2(1)}{p_1(1)} = \frac{W_{22}(1) - W_{11}(1) + \sqrt{[W_{22}(1) - W_{11}(1)]^2 + 4\,W_{12}^2(1)}}{2\,W_{12}(1)}. \qquad (2.2.11)$$

Specifically, the semi-axes of the NMO ellipse in the first layer constrain the zero-dip NMO velocity $V_{\rm nmo}(0)$ and the anellipticity coefficient η. As a result, the data vector in the top layer contains only five components. Singular-value decomposition (SVD) analysis performed below shows that this is the *only* relationship among the components of the data vector, if all interfaces have different strikes.

The goal of the tomographic algorithm introduced here is to estimate the anisotropic subsurface model using wide-azimuth measurements of stacking (moveout) velocities on moderate-length CMP spreads (i.e., spreads close to the reflector depth). Therefore, this approach can be classified as *anisotropic stacking-velocity tomography*. Although limiting the input data to stacking velocities excludes the far-offset information from analysis, it has important advantages over conventional tomography. First, azimuthally-varying moveout velocity, described by the NMO ellipse, can be computed by tracing only one zero-offset ray per common midpoint and per reflector, which makes anisotropic tomography computationally feasible (Grechka and Tsvankin, 1999b). Second, even for lower-symmetry systems NMO ellipses can be described by semi-analytic expressions providing valuable insight into the parameter combinations constrained by a certain set of input data (e.g., Grechka and Tsvankin, 1999a). Third, stacking-velocity tomography can be performed locally on the horizontal scale of a single CMP gather, and the velocity field can be estimated separately for relatively small blocks containing several adjacent common midpoints. Within each block, the layers can be treated as homogeneous, and the interfaces can be approximated by simple smooth surfaces, such as low-order polynomials. Then global smoothing can be applied to build the laterally varying anisotropic velocity field and

reflecting interfaces.

For inversion purposes, it is convenient to split the vector $\mathbf{d}(\mathbf{O}, n)$ into two parts. For a given ("trial") set of the interval VTI parameters $\mathbf{l}_n$ [equation (2.1.2)], the observed values of $\tau_0(n)$ and the horizontal slownesses $p_1(n)$, $p_2(n)$ can be used to compute values for the depths, dips, and azimuths of the interfaces $\mathbf{i}_n$ [equation (2.1.3)]. Indeed, knowledge of the parameters of the first layer $\tilde{\mathbf{l}}_1$ is sufficient for computing the vertical slowness component from the Christoffel equation and obtaining the slowness vector $\mathbf{p}(1)$. Since the slowness vector of the zero-offset ray is orthogonal to the reflector, the vector $\mathbf{p}(1)$ defines the reflector normal. Then one can find the group-velocity vector (ray) in the first layer and use the traveltime $\tau_0(1)$ to compute the depth z_1 of the first reflector.

Once the first interface has been reconstructed, the slowness vector in the second layer can be obtained from Snell's law and used to find the orientation of the second reflector. The zero-offset traveltime of the reflection from the second interface gives an estimate of the reflector depth, etc. Continuing this procedure downward yields the dips, strikes (or azimuths), and depths for all interfaces of the trial model. Clearly, any errors in the input data or trial layer parameters $\tilde{\mathbf{l}}_n$ will distort the computed interfaces $\tilde{\mathbf{i}}_n$.

The best-fit vector of the layer parameters $\mathbf{l}_n$ is found by inverting the NMO ellipses $\mathbf{W}(n)$ because the rest of the input data has already been used to determine the interfaces. Therefore, to study the feasibility of the inversion procedure it is sufficient to perform SVD analysis of the $3N \times 3N$ matrix of Frechét derivatives

$$\mathcal{F} = \frac{\partial \mathbf{W}(n)}{\partial \mathbf{l}_k}, \quad (k, n = 1, \ldots, N). \tag{2.2.12}$$

Here we assume that the vector $\mathbf{i}$, which specifies the interfaces, is such that the computed traveltimes and horizontal slowness components for each trial model exactly match those in the data. We compute the NMO ellipses using the formalism described in Grechka and Tsvankin (2002a).

Figure 2.3 shows a typical result of SVD analysis of the NMO ellipses with respect to the parameters $\mathbf{l} = \{V_{P0,1}, \epsilon_1, \delta_1, V_{P0,2}, \epsilon_2, \delta_2\}$ in a two-layer model. While the last singular value is always equal to zero, the other five do not vanish if the azimuths of the interfaces are different (see the curves marked by squares, diamonds, and triangles). The presence of two vanishing singular values when the strikes of both interfaces coincide (the circles in Figure 2.3) is not surprising, because in this case the axes of the NMO ellipse from the bottom of the model are aligned with the dip and strike directions (i.e., the model becomes 2-D), and there is one less independent data component.

The model from Figure 2.3 can be used to support the statement that the inversion results are independent of the CMP location. Therefore, it is indeed sufficient to carry out the inversion using the NMO ellipses from all interfaces measured at a single CMP.

To get a more quantitative assessment of the feasibility of the inversion for the model from Figure 2.3, we performed a series of SVD analyzes of the matrix W_{ij} for different values of the dip (ϕ_1) and azimuth (ψ_1) of the first interface. The results, displayed in Figure 2.4, indicate that it should be possible to estimate five parameter combinations for any choice of ϕ_1 and ψ_1, with the exception of $\psi_1 = 0°$, $180°$ and $\phi_1 = 0°$. In the first two cases, the two reflectors are co-oriented, and the 3-D model becomes 2-D, which reduces the number of equations to four. In the third case ($\phi_1 = 0°$),

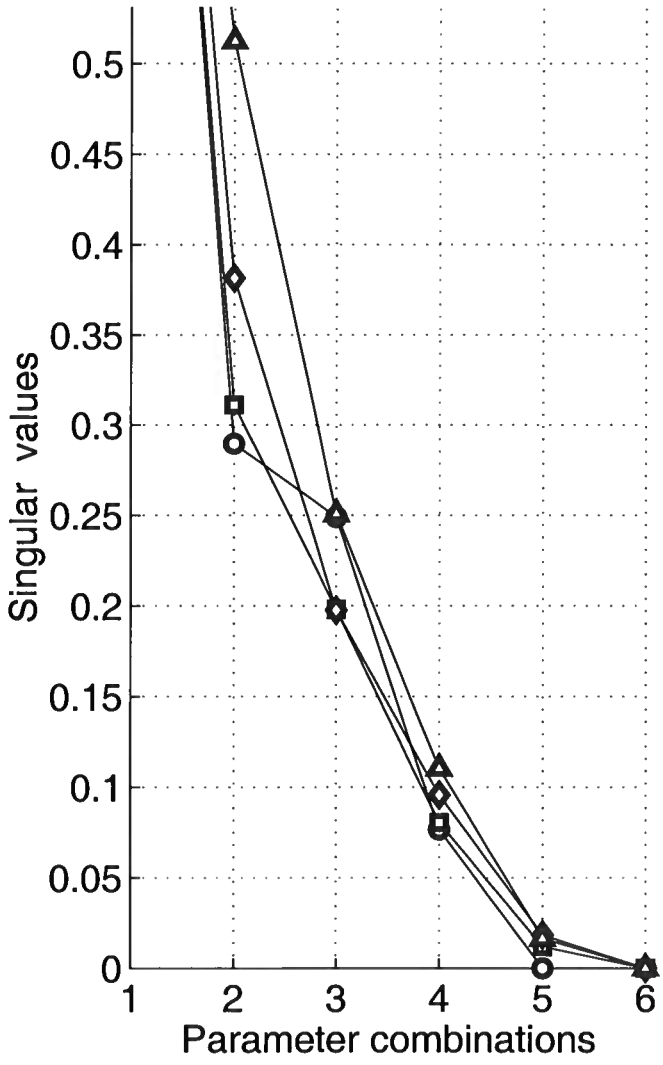

FIG. 2.3. SVD analysis for a two-layer VTI model with the parameters $V_{P0,1} = 2$ km/s, $\epsilon_1 = 0.15$, $\delta_1 = 0.05$, $V_{P0,2} = 3$ km/s, $\epsilon_2 = 0.25$, $\delta_2 = 0.10$. The singular values are normalized by the greatest one. The interface depths under the CMP location $\mathbf{O} = [0, 0, 0]$ are $z_1 = 1$ km and $z_2 = 3$ km, the dips $\phi_1 = 40°$ and $\phi_2 = 20°$, and the azimuth of the bottom interface is $\psi_2 = 0°$. The curves correspond to different azimuths of the intermediate (first) interface: $\circ$ ($\psi_1 = 0°$), $\square$ ($\psi_1 = 30°$), $\diamond$ ($\psi_1 = 60°$) and $\triangle$ ($\psi_1 = 90°$).

the first layer is horizontal, and the NMO ellipse $W(1)$ degenerates into a circle that constrains just one combination of the medium parameters.

The observations drawn from Figures 2.3 and 2.4 can be extended to an arbitrary number of VTI layers. The NMO ellipses constrain at a maximum $3N - 1$ combinations of the $3N$ interval parameters $\{V_{P0,n}, \epsilon_n, \delta_n\}$ $(n = 1, \ldots, N)$, provided the model interfaces have different azimuths. Otherwise, P-wave traveltimes contain less information about the medium. For instance, if the azimuths of all interfaces are identical, the model degenerates into 2-D, and the NMO ellipses from different reflectors are co-oriented. Thus, only their semi-axes constrain the layer parameters, and the number of independent equations reduces to $2N$. In the limiting case of horizontal layers, the NMO ellipses become circles defined by the N interval zero-dip NMO velocities. Hence, unambiguous inversion is impossible without additional information; some practical possibilities are discussed below.

2.3 Parameter estimation using *a priori* information

2.3.1 Specifying one of the parameters

The results of the previous section suggest that *a priori* knowledge of a single layer parameter may be sufficient to overcome the ambiguity. For example, it might be possible to estimate the vertical velocity $V_{P0,1}$ in the top layer using a shallow borehole and then obtain the anisotropic parameters ϵ_1 and δ_1 from the NMO ellipse $\mathbf{W}(1)$. According to the SVD results, this should be sufficient for estimating the remaining medium parameters.

To verify this conclusion, we performed several numerical tests, with typical results

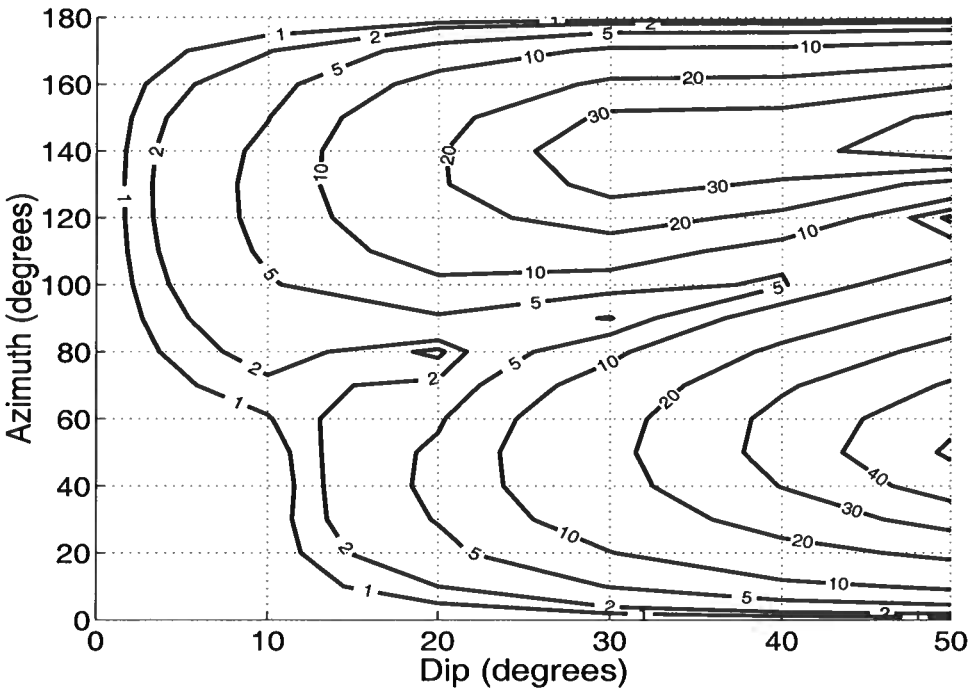

FIG. 2.4. Contours of the fifth eigenvalue (multiplied by 1000) as a function of the dip ϕ_1 and azimuth ψ_1 of the intermediate interface in a two-layer VTI model. The parameters $V_{P0,1}$, ϵ_1, δ_1, $V_{P0,2}$, ϵ_2, δ_2, z_1, z_2, ϕ_2, and ψ_2 are the same as those in Figure 2.3.

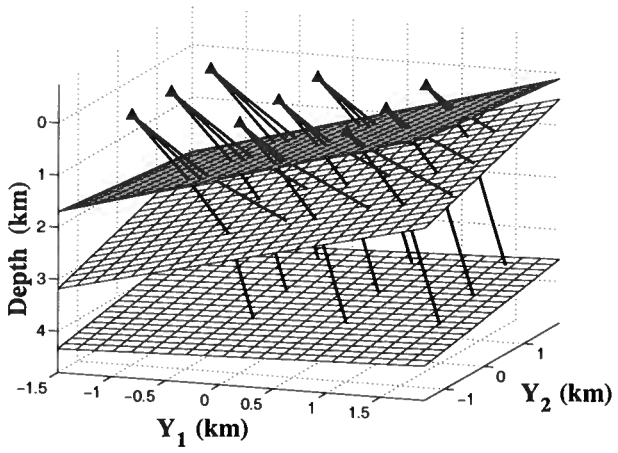

FIG. 2.5. Zero-offset P-wave rays in the three-layer VTI model from Table 1.

listed in Table 1. We traced reflected rays through a three-layer VTI model for nine CMP locations (Figure 2.5 and Table 1), added Gaussian noise to the computed NMO velocities and zero-offset traveltimes, and obtained the layer parameters by least-squares fitting of the NMO ellipses. Although, as discussed above, multiple common midpoints do not provide new information for the inversion, they help to stabilize results in the presence of random noise.

To constrain the inversion, the parameter $\delta_1 = 0.04$ was assumed to be known, which allowed the other parameters to be estimated with good accuracy (Table 1). The errors generally increase with depth, which can be expected from Dix-type algorithms. The low accuracy for the parameter ϵ_3 in the bottom layer is associated with insufficient angle coverage of the reflected rays.

	$V_{P0,1}$ (km/s)	ϵ_1	δ_1	$V_{P0,2}$ (km/s)	ϵ_2	δ_2	$V_{P0,3}$ (km/s)	ϵ_3	δ_3
Correct	1.00	0.08	0.04	2.00	0.20	0.10	3.00	0.10	0.05
Inverted	0.99	0.09	–	2.02	0.18	0.09	2.96	0.18	0.07

	z_1 (km)	ϕ_1 (deg)	ψ_1 (deg)	z_2 (km)	ϕ_2 (deg)	ψ_2 (deg)	z_3 (km)	ϕ_3 (deg)	ψ_3 (deg)
Correct	1.00	30.0	–10.0	2.00	30.0	30.0	4.00	10.0	70.0
Inverted	1.00	29.8	–10.0	1.98	29.9	30.4	3.98	10.3	70.5

Table 1. Comparison of the correct and inverted parameters of a three-layer VTI model (see Figure 2.5). The standard deviations of Gaussian noise added to the NMO velocities and zero-offset traveltimes are 2.0% and 0.5%, respectively.

The choice of δ_1 as the known parameter was arbitrary; holding any other interval parameter at the correct value produces similar quality results. Thus, one can therefore reconstruct the entire model if the vertical velocity $V_{P0,n}$ or one of the anisotropic coefficients (ϵ_n or δ_n) in any layer, is known; in principle, the interval anisotropic parameter can be obtained from vertical seismic profile (VSP) data or well log data. In the case of well log data, it is necessary to apply several corrections to the response of the borehole tools; for instance, we need to take into account the effects caused by the invasion zone (Peeters et al., 1999). The presence of the invasion zone makes the parameter estimation from well log data difficult. The inversion procedure also works well in the special case of isotropy, i.e., when ϵ_n and δ_n are set to zero in one or more layers.

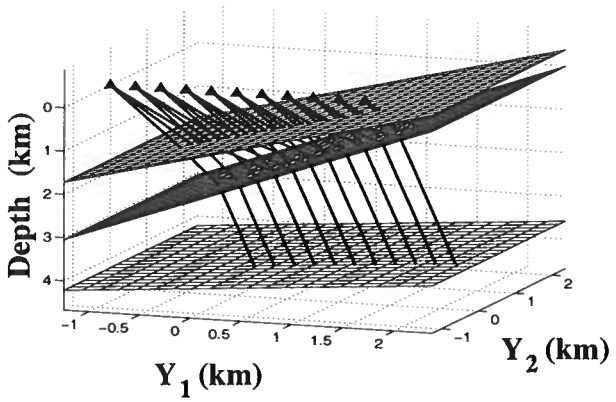

FIG. 2.6. Zero-offset rays in a three-layer VTI model. All interfaces have the same azimuth $\psi_1 = \psi_2 = \psi_3 = 0°$.

2.3.2 Specifying vertical velocity in 2-D models

We also examined the case when all interfaces in the three-layer medium discussed above have the same azimuth. The axes of the NMO ellipses W(1), W(2), and W(3) in such a model are parallel to the dip and strike directions, so the moveout data provide only six equations (two semi-axes for each ellipse). With a total of nine medium parameters (three per layer); thus, three parameters have to be specified in advance. One possibility, examined in the test from Figure 2.6 and Table 2, is to assume that the vertical velocities in the model are known, for example, from vertical seismic profile (VSP) data. We modeled zero-offset traveltimes and NMO ellipses for several CMP locations distributed along the dip direction (Figure 2.6) and again performed inversion of noise-contaminated data. With the vertical velocities in each layer, $V_{P0,1} = 1$ km/s, $V_{P0,2} = 2$ km/s, and $V_{P0,3} = 3$ km/s, assumed to be known. The inverted interval parameters ϵ_n and δ_n are in close agreement with the actual values (Table 2). Comparable accuracy was achieved in a number of other tests in which the number of layers and the level of noise were varied.

	$V_{P0,1}$ (km/s)	ϵ_1	δ_1	$V_{P0,2}$ (km/s)	ϵ_2	δ_2	$V_{P0,3}$ (km/s)	ϵ_3	δ_3
Correct	1.00	0.08	0.04	2.00	0.20	0.10	3.00	0.10	0.05
Inverted	–	0.08	0.04	–	0.19	0.10	–	0.08	0.05

Table 2. Comparison of the correct and inverted values of parameters for the three-layer VTI model shown in Figure 2.6. The standard deviations of the Gaussian noise added to the traveltimes and NMO velocities are 1.0% and 2.0%, respectively.

2.3.3 Specifying a relationship between ϵ and δ

Another way to reduce the number of unknowns is to impose an empirical relationship between ϵ and δ, such as those discussed by Ryan-Grigor (1998), in at least one layer. We found that making ϵ a known function of δ [i.e., $\epsilon = \epsilon(\delta)$] generally makes the parameter estimation unique. Let us assume, for example, that the relation between the interval ϵ_n and δ_n is linear ($\delta_n = k_n \epsilon_n$), with the coefficients k_n known *a priori*. Figure 2.7 displays the contours of the smallest singular value (the singular values are all normalized to unity) for a two-layer VTI model in which $\delta_1 = k_1 \epsilon_1$ and $\delta_2 = k_2 \epsilon_2$ (in principle, specifying k_1 alone would be sufficient). Although this singular value was computed as a function of k_1 and k_2, the axes in Figure 2.7 are labeled in terms of the anellipticity coefficients $\eta_n \equiv (\epsilon_n - \delta_n)/(1+2\,\delta_n)$ (for weak anisotropy, $\eta_n \approx \epsilon_n - \delta_n$) to demonstrate that the only vanishing singular value corresponds to elliptical anisotropy of the *whole* model ($\eta_1 = \eta_2 = 0$). If either $\eta_1 \neq 0$ or $\eta_2 \neq 0$, none of the eigenvalues goes to zero, and the inversion becomes feasible. This is illustrated by the satisfactory inversion results for the model with $\eta_1 = \eta_2 = 0.05$ in Table 3.

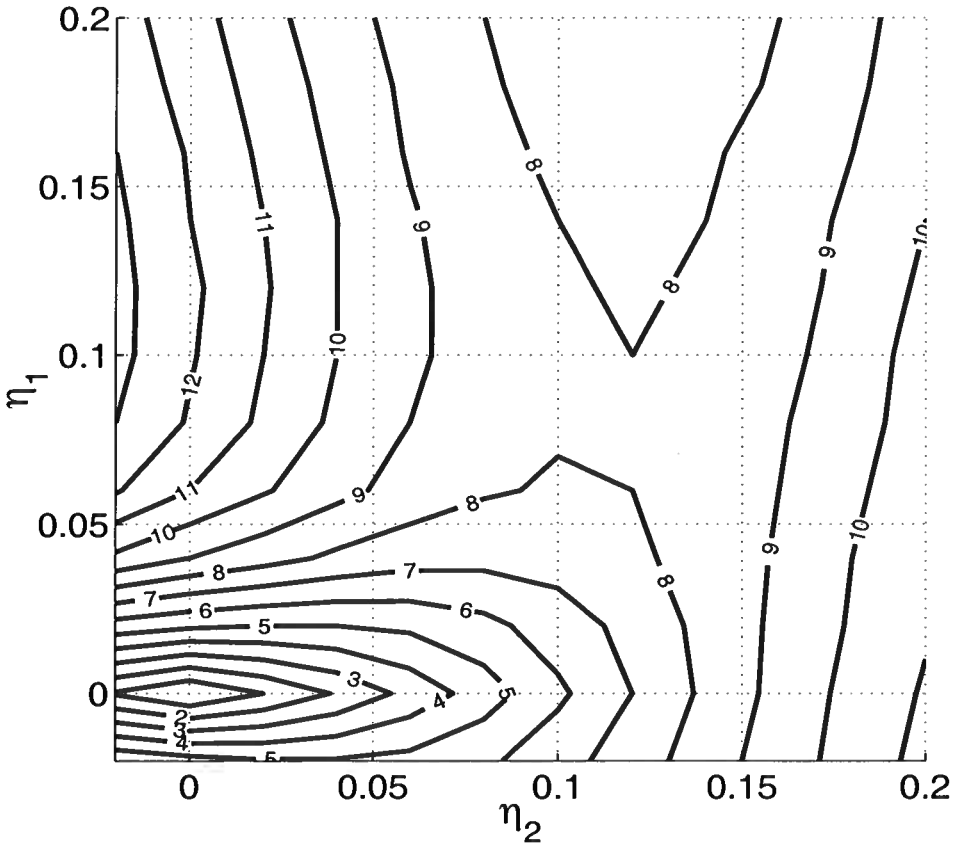

FIG. 2.7. Contours of the smallest singular value (multiplied by 1000) for a two-layer VTI model. The relevant model parameters are $V_{P0,1} = 1$ km/s, $\epsilon_1 = 0.20$, $\delta_1 = k_1 \epsilon_1$, $V_{P0,2} = 2$ km/s, $\epsilon_2 = 0.20$, $\delta_2 = k_2 \epsilon_2$, $\phi_1 = 30°$, $\psi_1 = 30°$, $\phi_2 = 50°$, $\psi_2 = 0°$, $z_1 = 1$ km, $z_2 = 3$ km. The coefficients k_1 and k_2 vary from 0 to 1.1.

	$V_{P0,1}$ (km/s)	ϵ_1	$V_{P0,2}$ (km/s)	ϵ_2
Correct	1.00	0.20	2.00	0.20
Inverted	0.98	0.18	1.98	0.17

Table 3. Comparison of the correct and inverted values of parameters for the two-layer VTI model from Figure 2.7. k_1 and k_2 are such that $\eta_1 = \eta_2 = 0.05$. NMO velocities, computed at 200 CMP locations, were contaminated by Gaussian noise with a standard deviation of 2%.

One special case when this approach does *not* help is elliptical anisotropy. Even if all layers are known to be elliptically anisotropic ($k_n = 1$, $\epsilon_n = \delta_n$), and the number of relevant VTI parameters reduces to $2N$, the $3N - 1$ equations for the NMO ellipses do not have a unique solution. This conclusion is in agreement with the results of Dellinger and Muir (1988) obtained using linear transformations (stretching) of the isotropic wave equation.

2.4 Models with curved interfaces or faults

A priori information may not be needed at all for models with nonplanar reflectors in some of the layers. Variable reflector dip causes reflected rays to span more spatial directions, which helps to constrain the anisotropic velocity model. While media with irregular interfaces are discussed in detail in Chapter 3, here we show how additional dips can remove the nonuniqueness in the parameter estimation.

Suppose, for example, that the intermediate interface in the two-layer VTI model from

Figure 2.3 is bent in such a way that it has two plane portions with the same dip $\phi_1 = 40°$ but different azimuths $\psi_1 = 30°$ and $\psi_1 = 90°$. Recording reflections, from the bottom of the model, that cross both portions of the intermediate interface yields an additional NMO ellipse (i.e., three more equations). The absence of vanishing singular values for this problem (Figure 2.8; the smallest singular value is 0.02) indicates that all parameters can be resolved uniquely. Here all the layers are assumed to be homogeneous.

Parameter estimation may also become feasible if the model contains a dipping fault plane (such as in Figure 2.9) and the data include reflections from both the fault and layer boundaries. A similar model was used by Alkhalifah and Tsvankin (1995), who developed a dip-moveout inversion method to estimate the interval values of η from surface P-wave data. Alkhalifah and Tsvankin (1995), however, assumed that each zero-offset reflected ray crosses only *horizontal* interfaces on its way to the surface.

In the models analyzed above (e.g., Figure 2.9), intermediate interfaces are dipping, which introduces dependence of NMO ellipses from both horizontal and dipping reflectors on the interval values of ϵ and δ. Even for 2-D media with fault planes in some of the layers, it may be possible to determine all relevant VTI parameters. For example, the semi-axes of the three NMO ellipses corresponding to the zero-offset rays marked in Figure 2.9 provide us with six equations. SVD analysis reveals no zero singular values, which indicates that the interval parameters can be found in a unique fashion (Figure 2.10). Still, the inverse problem is not as well-posed as that for 3-D models because the smallest singular value in Figure 2.10 is just 0.0014 compared to 0.02 in Figure 2.8.

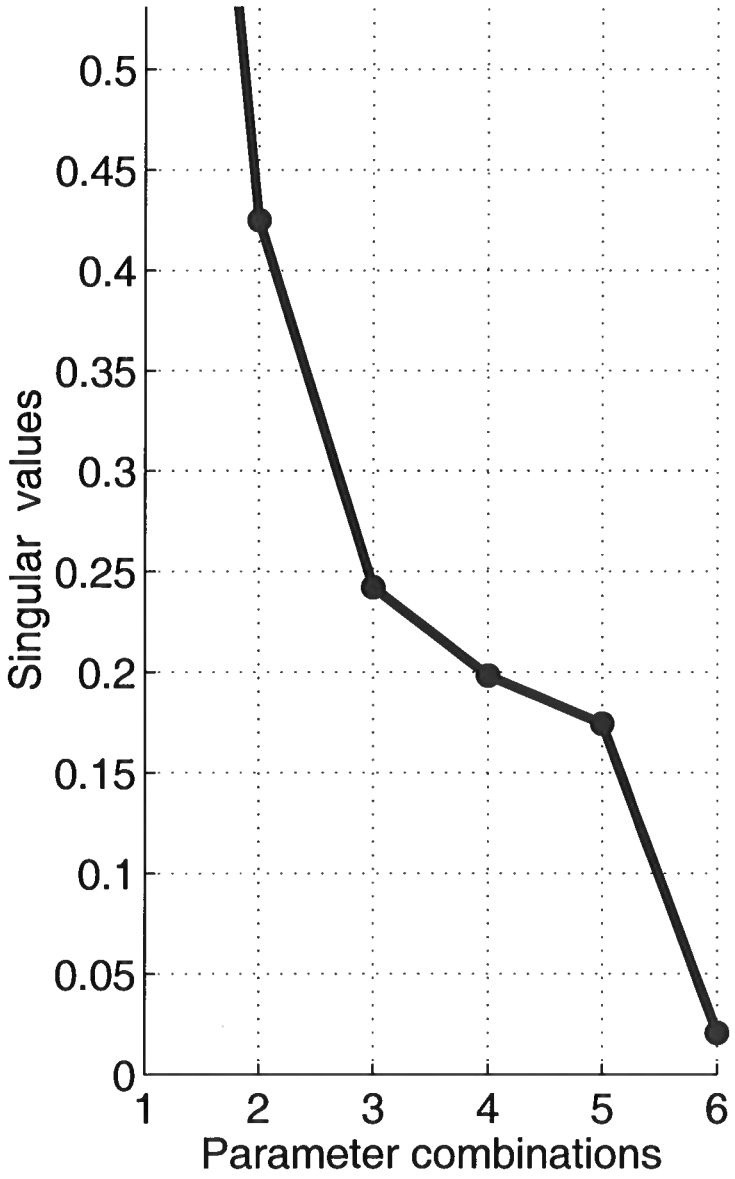

FIG. 2.8. SVD analysis for a two-layer VTI model similar to the one in Figure 2.3. This time, however, the intermediate interface contains two segments with the same dip $\phi_1 = 40°$ but different azimuths $\psi_1 = 30°$ and $\psi_1 = 90°$.

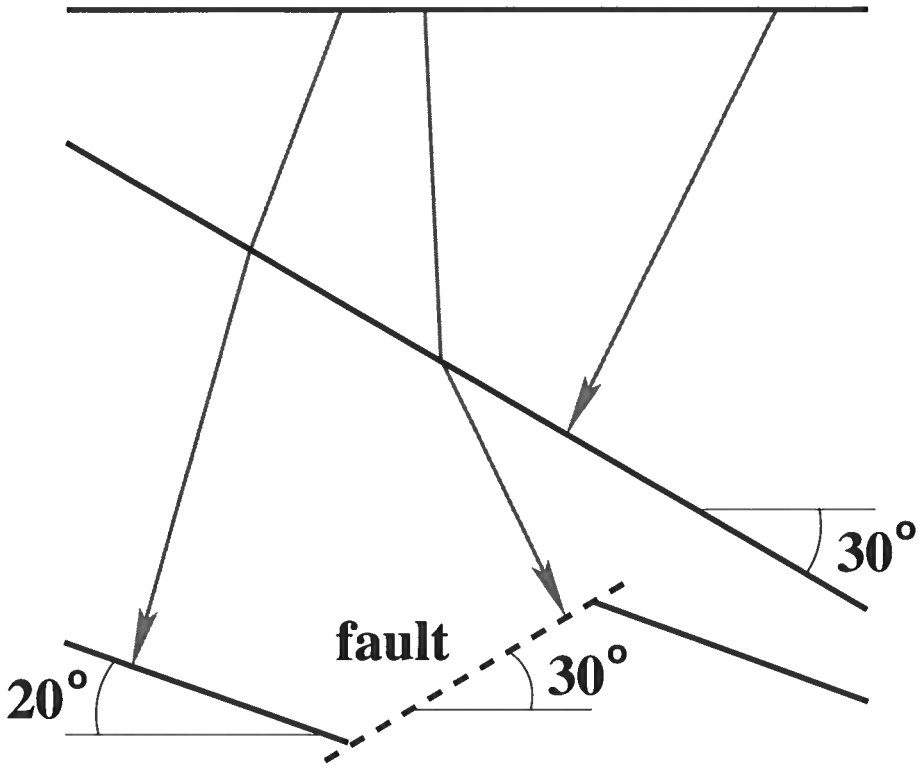

FIG. 2.9. The presence of fault-plane reflections in a layered VTI medium might be sufficient to obtain the model in depth from P-wave reflection data.

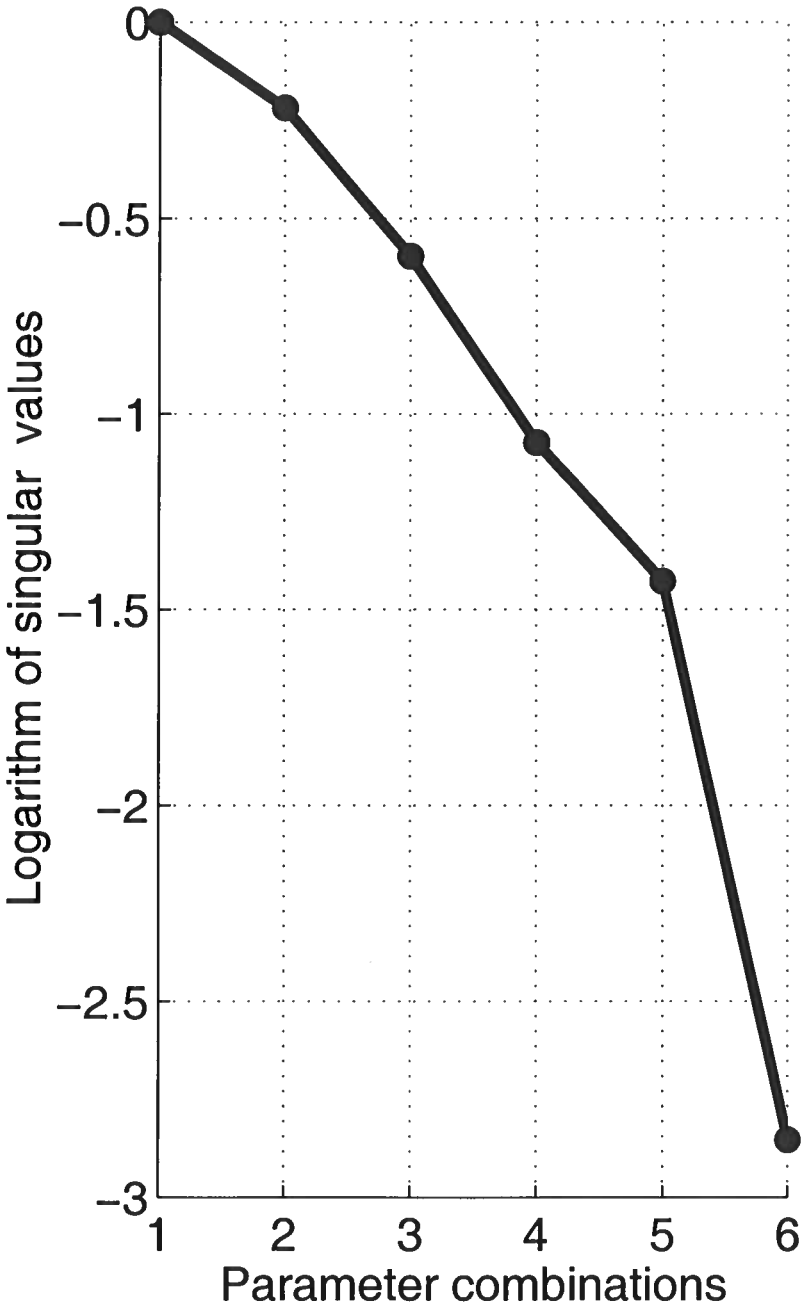

FIG. 2.10. SVD analysis for the VTI model from Figure 2.9. The layer parameters are the same as those in Figure 2.3.

2.5 Summary

P-wave NMO ellipses measured from multi-azimuth 3-D reflection data over layered VTI media depend on all three relevant interval Thomsen parameters ($V_{0,n}$, ϵ_n and δ_n) if the overburden contains dipping interfaces. Here, we examined the inversion of P-wave traveltime data for the interval VTI parameters, the orientation (dip and azimuth), and depth of the interfaces. For each trial model the objective function, which has to be minimized during the inversion, is obtained in two steps. First, P-wave zero-offset traveltimes and reflection slopes (horizontal slownesses) are used to find the dip, azimuth, and depth of all interfaces and reconstruct the trial model in depth. Second, one computes the effective NMO ellipses of reflection events and defines the objective function as a measure of the difference between the modeled ellipses and those recovered from the data. This is an iterative scheme. We call this methodology "P-wave stacking-velocity tomography."

If the interfaces have different azimuths and do not cross each other, the P-wave NMO ellipses in an N-layer model yield $3N-1$ independent equations for the $3N$ interval VTI parameters $V_{0,n}$, ϵ_n, and δ_n. The spatial variation of the NMO ellipses for this model does not provide any additional information for the inversion procedure. Therefore, in general, surface 3-D P-wave data alone are generally insufficient to determine the unknown VTI parameters and reconstruct the interfaces in a unique fashion. For 2-D models with co-oriented interfaces, the axes of all NMO ellipses are parallel to the dip and strike directions, and the number of independent equations reduces to $2N$.

This ambiguity, however, can be overcome if a *single* parameter in any layer is known *a priori*. For example, in many cases a subsurface layer may be assumed to be isotropic

($\epsilon_j = \delta_j = 0$), or the vertical velocity in it may be estimated in a shallow borehole. The inversion can also be made unique by introducing a certain relationship between the parameters (e.g., between ϵ and δ) in at least one of the layers. The only model for which this approach fails to remove the ambiguity in the inversion of P-wave data is elliptical anisotropy ($\epsilon_n = \delta_n$). For 2-D models it is necessary to specify one parameter per layer before the inversion; for instance, the vertical velocities may be known from VSP measurements.

The VTI parameters are generally better constrained by P-wave reflection data if the medium contains a fault plane or curved interfaces. For some types of models with intersecting interfaces the inversion does not require any *a priori* information.

Chapter 3

PARAMETER ESTIMATION IN LAYERED VTI MEDIA WITH CURVED INTERFACES

In Chapter 2, we evaluated the feasibility of parameter estimation for VTI media composed of homogeneous layers separated by planar dipping interfaces. If the interfaces do not intersect each other, unambiguous inversion for the depth model requires minimal *a priori* information, such as knowledge of a single VTI parameter in one of the layers. Here, we study the inversion of P-wave reflection traveltimes for more complicated VTI models, which contain *irregular* interfaces.

First, we extend the theory of NMO-velocity surfaces (Grechka and Tsvankin, 2002a) to anisotropic media with irregular interfaces and develop an efficient algorithm for modeling multi-azimuth and multi-offset reflection traveltimes. Then, we employ singular value decomposition and actual inversion of P-wave reflection data to show that for some VTI models with smooth curved interfaces parameter estimation in depth can be accomplished without any *a priori* information.

3.1 NMO velocity in anisotropic media with irregular interfaces

3.1.1 NMO velocity on a curved CMP line

The NMO ellipse $\mathbf{W}$ recorded in the plane $\mathcal{P}$ can be viewed as the intersection of the NMO-velocity surface $\mathbf{U}$ with $\mathcal{P}$ (Grechka and Tsvankin, 2002a):

$$\mathbf{W} = \mathbf{U} \bigcap \mathcal{P}. \tag{3.1.1}$$

If the CMP line $\boldsymbol{\sigma}$ is curved, as in acquisition from non-flat topography (e.g., Gray et al., 1999), its curvature will influence the value of NMO velocity $V_{\rm nmo}(\boldsymbol{\sigma})$. The expression for $V_{\rm nmo}(\boldsymbol{\sigma})$ is derived in Appendix E:

$$V_{\rm nmo}^{-2}(\boldsymbol{\sigma}) = \mathcal{L}\,\mathbf{U}\,\mathcal{L}^{\mathbf{T}} + \tau_0\,\mathbf{p}\cdot\mathcal{K}, \tag{3.1.2}$$

where

$$\mathcal{K} \equiv \left.\frac{d^2\boldsymbol{\sigma}(h)}{dh^2}\right|_{h=0} \tag{3.1.3}$$

is the second-order derivative of the radius-vector $\boldsymbol{\sigma}$ with respect to half-offset h; it is evaluated at the common-midpoint (zero offset). Depending on the sign of the dot product $\mathbf{p}\cdot\mathcal{K}$, the line curvature can either increase or reduce the NMO velocity.

3.1.2 Dix-type averaging in media with irregular interfaces

Equation (3.1.2) can be applied to the CMP line $\boldsymbol{\sigma}$ that lies on any irregular surface $\mathbf{s}$. The NMO velocity $V_{\rm nmo}(\mathbf{s},\ell)$ along direction ℓ on $\mathbf{s}$ is given by

$$V_{\rm nmo}^{-2}(\mathbf{s},\ell) = \ell\ (\mathbf{W} + \tau_0\,\mathbf{p}\cdot\boldsymbol{\kappa})\ \ell^{\mathbf{T}}\,, \tag{3.1.4}$$

where $\mathbf{W}$ is the NMO ellipse obtained as the intersection of the NMO-velocity surface $\mathbf{U}$ with the plane $\mathcal{P}$ tangent to $\mathbf{s}$ at $\mathbf{Y}$. In equation (3.1.4) it is assumed that the slowness vector $\mathbf{p}$ is continuous across $\mathbf{s}$. The matrix

$$\boldsymbol{\kappa}_{ij} = \left.\frac{\partial^2\mathbf{s}}{\partial h_i\,\partial h_j}\right|_{h_1=h_2=0}, \quad (i,j=1,2) \tag{3.1.5}$$

is composed of the second-order derivatives of $\mathbf{s}(h_1,\ h_2)$ with respect to the half-offsets h_1 and h_2; the values $h_1 = h_2 = 0$ correspond to the CMP location.

If $\mathbf{s}$ represents the boundary between two layers, the NMO ellipse is discontinuous across the tangent plane $\mathcal{P}$, with the jump depending on the difference between the slowness vectors above ($\mathbf{p}^{(+)}$) and below ($\mathbf{p}^{(-)}$) surface $\mathbf{s}$. As shown in Appendix G, equation (3.1.4) leads to the following expression for the NMO ellipse $\mathbf{W}^{(+)}$ on the "positive" side of the interface:

$$\mathbf{W}^{(+)} = \mathbf{W}^{(-)} - \tau_0\,\left(\mathbf{p}^{(+)} - \mathbf{p}^{(-)}\right)\cdot\boldsymbol{\kappa}\,, \tag{3.1.6}$$

where the term $\left[\tau_0\,\left(\mathbf{p}^{(+)} - \mathbf{p}^{(-)}\right)\cdot\boldsymbol{\kappa}\right]$ represents a correction for the interface curvature.

The above results make it possible to generalize the Dix-type averaging procedure of Grechka and Tsvankin (2002a) to media with irregular interfaces. Suppose the model above the reflector contains N homogeneous layers, and we know the NMO-velocity cylinder in the layer immediately above the reflector. Slicing this cylinder by the plane tangent to the $N-1$th interface at the intersection point of the zero-offset ray yields the NMO ellipse $\mathbf{W}_{n-1}^{(-)}$. Applying equation (3.1.6), one finds the ellipse

$\mathbf{W}_{n-1}^{(+)}$ corrected for the interface curvature and then substitutes it into the Dix-type averaging equation:

$$[\mathbf{W}(N)]^{-1} \sum_{n=1}^{N} \tau_{0,n} = \sum_{n=1}^{N} \left[\mathbf{W}_n^{(+)}\right]^{-1} \tau_{0,n}\,, \tag{3.1.7}$$

where $\mathbf{W}(N)$ is the effective NMO ellipse at the earth's surface, and $\tau_{0,n}$ are the interval zero-offset traveltimes. Application of equation (3.1.7) involves projecting the NMO-velocity cylinders onto the planes tangent to the layer interfaces following the methodology of Grechka and Tsvankin (2002a).

Equation (3.1.7) allows us to compute the effective NMO ellipse $\mathbf{W}$, which can be obtained from 3-D multi-azimuth reflection data. Since it is necessary to trace only one (zero-offset) ray per common midpoint, the hyperbolic portion of pure-mode reflection moveout can be modeled without the time-consuming calculation of multi-offset and multi-azimuth traveltimes.

3.2 Parameter estimation using P-wave reflection traveltimes

3.2.1 Model representation and data for inversion

The above theory of NMO ellipses is a convenient tool for traveltime modeling that can be efficiently used in parameter-estimation algorithms. The inversion methodology introduced here operates exclusively with surface P-wave data acquired in wide-azimuth 3-D surveys. The input data include the zero-offset P-wave traveltimes $\tau_0(n)$, the reflection slopes in orthogonal directions (horizontal slownesses) $\mathbf{p}(n) = [p_1(n), p_2(n)]$, and the NMO ellipses $\mathbf{W}(n)$ measured for all interfaces ($n = 1, \ldots, N$). As shown in

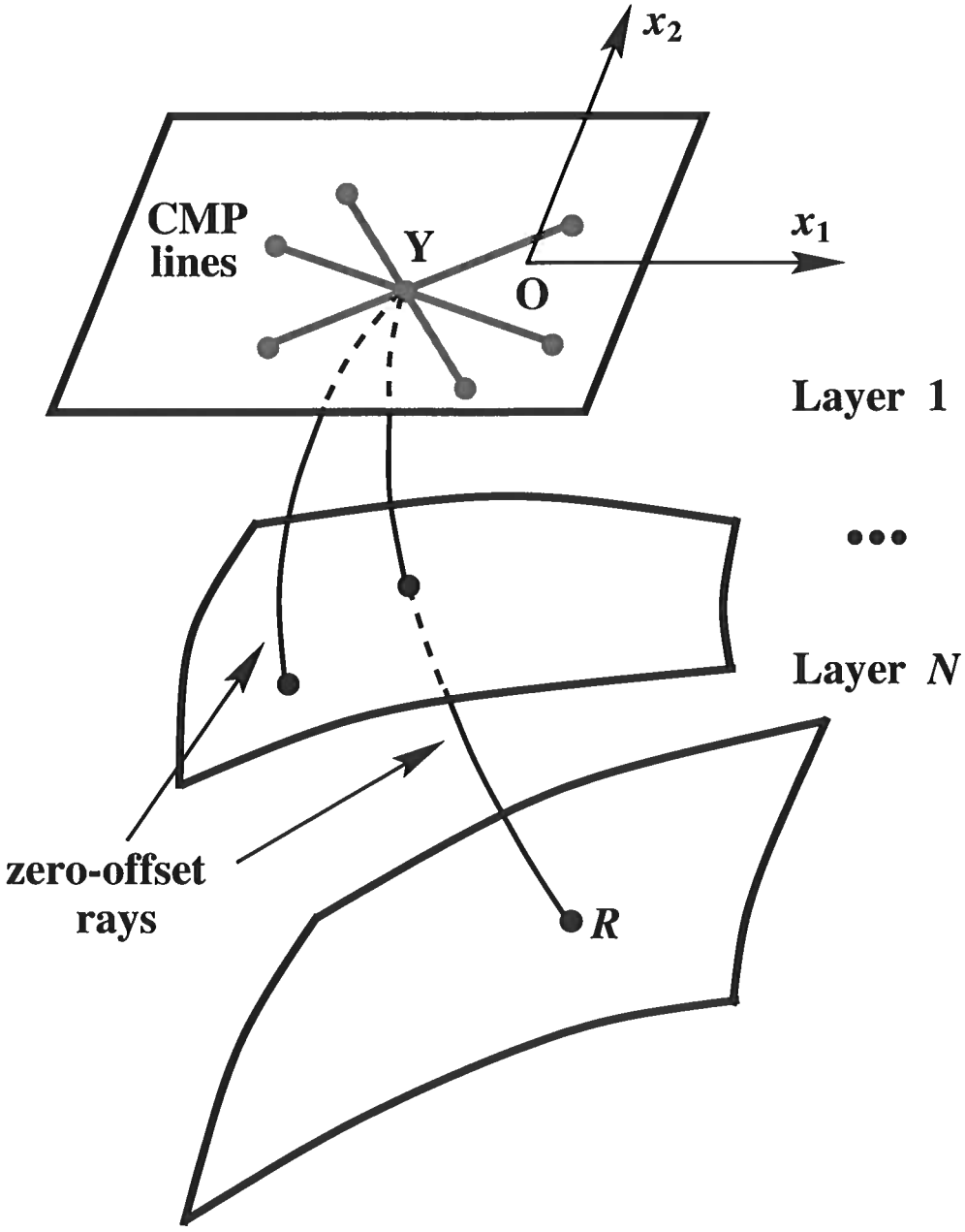

FIG. 3.1. Multi-azimuth CMP recording over a layered VTI model with irregular interfaces.

Chapter 2, this set of input parameters *does not* constrain the interval values of V_{P0}, ϵ, and δ if the VTI layers are homogeneous and separated by planar non-intersecting boundaries. Here, however, the interfaces are allowed to be irregular while the layers are still assumed to be homogeneous.

The goal is to determine whether or not the data

$$\mathbf{d}(\mathbf{Y},\, n) \equiv \{\tau_0(\mathbf{Y},\, n),\, \mathbf{p}(\mathbf{Y},\, n),\, \mathbf{W}(\mathbf{Y},\, n)\}\,, \tag{3.2.8}$$

acquired at a number of CMP locations $\mathbf{Y} = [Y_1, Y_2]$, can be inverted for all relevant model parameters

$$\mathbf{m} \equiv \{V_{P0,n},\, \epsilon_n,\, \delta_n,\, \zeta_{j_1 j_2, n}\}\,, \tag{3.2.9}$$

$$(n = 1,\, \ldots,\, N;\; j_1 = 1,\, \ldots,\, J_1;\; j_2 = 1,\, \ldots,\, J_2)\,.$$

Here $V_{P0,n}$, ϵ_n, δ_n are the interval VTI parameters, and $\boldsymbol{\zeta}_n$ are the matrices of the coefficients describing the depths $z_n(Y_1, Y_2)$ of the model interfaces.

Since the quantities $\boldsymbol{\zeta}_n$ have to be estimated from the data, some simplification in the inversion procedure can be achieved by adopting a linear relationship between $z_n(Y_1, Y_2)$ and $\zeta_{j_1 j_2, n}$. In principle, this requirement can be satisfied by representing the interfaces in terms of arbitrary basis functions $B_{j_1}(Y_1)$ and $B_{j_2}(Y_2)$:

$$z_n(Y_1, Y_2) = \sum_{j_1=1}^{J_1} \sum_{j_2=1}^{J_2} \zeta_{j_1 j_2, n}\, B_{j_1}(Y_1)\, B_{j_2}(Y_2)\,. \tag{3.2.10}$$

For simplicity, here we elected to implement the polynomial function,

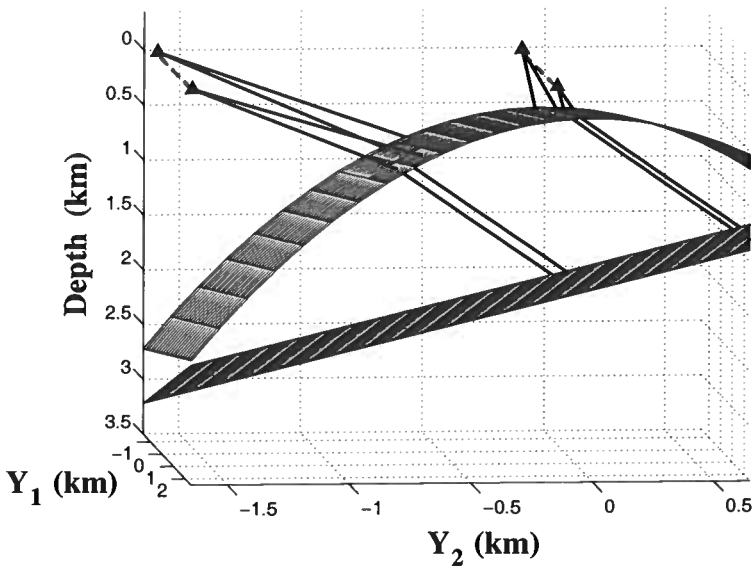

FIG. 3.2. Zero-offset rays in the two-layer VTI model used in SVD analysis. CMP locations are marked by triangles. The relevant layer parameters are $V_{P0,1} = 1$ km/s, $\epsilon_1 = 0.20$, $\delta_1 = 0.10$, $V_{P0,2} = 2$ km/s, $\epsilon_2 = 0.15$, $\delta_2 = 0.05$. The interfaces are described by 2-D quadratic polynomials, so $\boldsymbol{\zeta}_1$ and $\boldsymbol{\zeta}_2$ are 3×3 matrices.

$$z_n(Y_1, Y_2) = \sum_{j_1=1}^{J_1} \sum_{j_2=1}^{J_2} \zeta_{j_1 j_2, n}\, Y_1^{j_1-1}\, Y_2^{j_2-1}\,. \tag{3.2.11}$$

3.2.2 Feasibility of the inversion

For models with planar interfaces, the dependence of the data vector (3.2.8) on the CMP coordinate $\mathbf{Y}$ does not provide any new information about the model parameters (Chapter 2). This is no longer the case in the presence of interface curvature because zero-offset reflection rays change direction with the CMP location. Therefore, the spatial variation of the data may help to constrain the inversion and determine the depth scale of the model.

Similar to the approach outlined in Chapter 2, the zero-offset traveltimes $\tau_0(n)$ and

the reflection slopes $\mathbf{p}(n)$ can be used to estimate the shapes of the interfaces $z_n(\mathbf{Y})$ for any given estimate of the layer parameters

$$\mathbf{l} = \{V_{P0,n},\, \epsilon_n,\, \delta_n\}\,, \quad (n = 1, \ldots, N)\,. \tag{3.2.12}$$

This is achieved by tracing zero-offset rays downward and computing the coordinates of the reflection points and the corresponding interface normals.

In contrast to media with planar interfaces, the number of common midpoints and their spatial distribution determines the ability to reconstruct the irregular interfaces. Since the slowness vector of each zero-offset ray is orthogonal to the reflector at the reflection point R (Figure 3.1), it provides the orientation (i.e., the azimuth and polar angle) of the unit normal $\mathbf{b}_n(R)$ to the reflecting interface. In addition, the zero-offset traveltime yields the depth of the reflection point R. Thus, the triplet $\{\tau_0(n, \mathbf{Y}),\, p_1(n, \mathbf{Y}),\, p_2(n, \mathbf{Y})\}$ at CMP location $\mathbf{Y}$ provides three constraints on the quantities $\zeta_{j_1 j_2, n}$ specifying the reflector $z_n(\mathbf{Y})$ [equation (3.2.11)]. This implies that the number M of common midpoints required to obtain $J_1 \times J_2$ coefficients $\boldsymbol{\zeta}_n$ has to satisfy the inequality

$$M \geq \frac{J_1\, J_2}{3}\,. \tag{3.2.13}$$

For example, four common midpoints ($M = 4$) in Figure 3.2 should be sufficient for reconstructing the $J_1 \times J_2 = 3 \times 3 = 9$ coefficients that define each model interface. One can solve the equations for the coefficients $\boldsymbol{\zeta}_n$ by least squares using the data from all available CMP locations.

Since the traveltimes $\tau_0(n, \mathbf{Y})$ and slopes $\mathbf{p}(n, \mathbf{Y})$ are used to obtain $z_n(\mathbf{Y})$, the layer parameters $\mathbf{l}$ [equation (3.2.12)] will be found from the NMO ellipses $\mathbf{W}(n)$. To show

that the NMO ellipses may constrain the layer parameters uniquely, let us present an example of singular value decomposition (SVD) analysis for the two-layer VTI model shown in Figure 3.2. The ellipses measured from two reflectors at four CMP locations (triangles in Figure 3.2) provide $2 \times 4 \times 3 = 24$ equations for the six components of the vector $\mathbf{l}$.

Thus, the feasibility of the inversion can be ascertained by applying SVD to the 24×6 matrix $\mathcal{F}$ of Frechét derivatives,

$$\mathcal{F} = \frac{\partial \mathbf{W}(n, \mathbf{Y})}{\partial \mathbf{l}}, \tag{3.2.14}$$

computed for the correct values of model parameters $\mathbf{m}$. Since none of the singular values vanishes (Figure 3.3), the input data provide sufficient information for parameter estimation, and this VTI model can be fully reconstructed in the depth domain from P-wave reflection traveltimes.

Clearly, it is not *always* possible to obtain VTI parameters using just P-wave data. For example, as the curvature of the intermediate interface in Figure 3.2 decreases, the model approaches that with planar interfaces where at least one singular value is zero (Chapter 2).

3.3 Numerical examples

To confirm the SVD results, we carried out actual inversion of P-wave data for the model in Figure 3.2 in the presence of noise. Reflection traveltimes were computed for 240 common midpoints placed every 25 m along the two dashed lines between the triangles in Figure 3.2. This provided an overdetermined system of $240 \times 3 = 720$ equa-

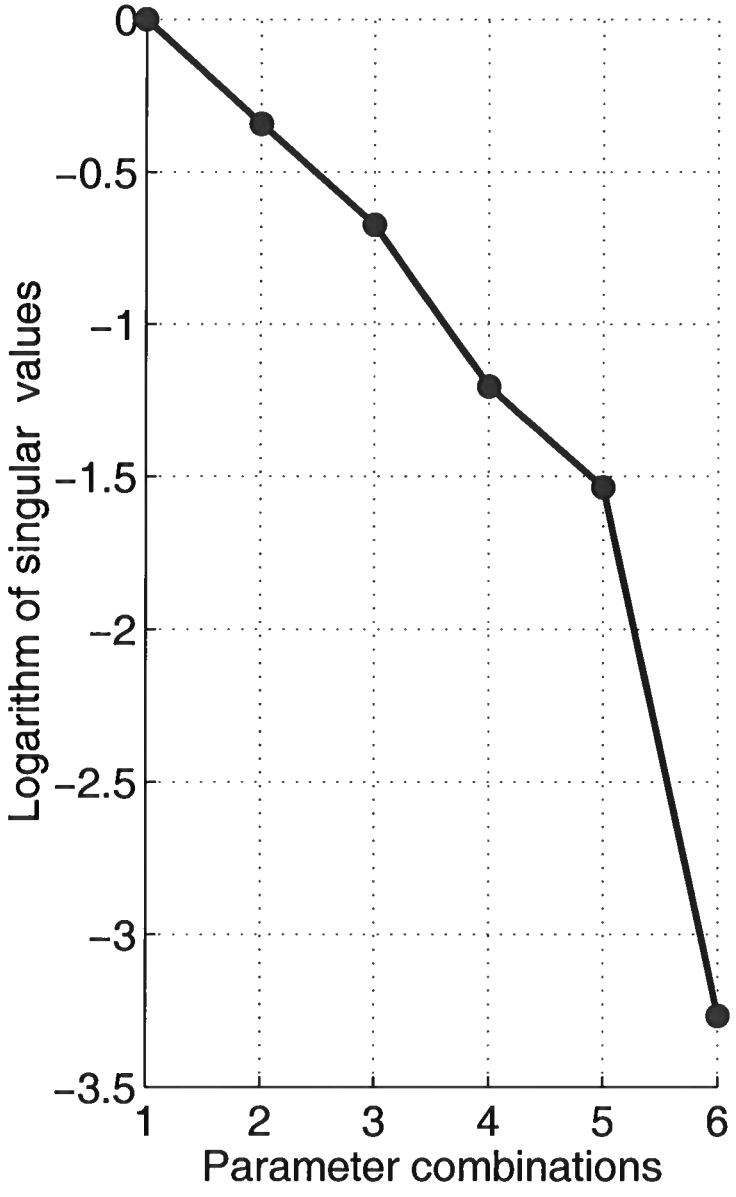

FIG. 3.3. Normalized singular values for the model from Figure 3.2.

	$V_{P0,1}$ (km/s)	ϵ_1	δ_1	$V_{P0,2}$ (km/s)	ϵ_2	δ_2
Correct	1.00	0.20	0.10	2.00	0.15	0.05
Inverted	1.02	0.17	0.07	2.05	0.11	0.03

Table 1. Inversion results for the two-layer VTI model from Figure 3.2. The standard deviations of Gaussian noise added to the NMO velocities and zero-offset traveltimes are 2.0% and 1.0%, respectively.

	$V_{P0,1}$ (km/s)	ϵ_1	δ_1	$V_{P0,2}$ (km/s)	ϵ_2	δ_2	$V_{P0,3}$ (km/s)	ϵ_3	δ_3
Correct	1.80	0.20	0.10	2.00	0.15	0.05	2.30	0.10	0.03
Inverted	1.77	0.23	0.12	1.97	0.17	0.07	2.26	0.12	0.05

Table 2. Inversion results for the three-layer VTI model from Figure 3.4. The errors in the inverted quantities are due to Gaussian noise added to the zero-offset traveltimes and NMO velocities. The standard deviations of the noise are 1.0% (for the traveltimes) and 2.0% (for the velocities).

tions for reconstructing the interface parameters $\boldsymbol{\zeta}_n$. Gaussian noise was added to the modeled NMO velocities and zero-offset traveltimes, and the parameter vector $\mathbf{m}$ was obtained [equation (3.2.9)] using least-squares fitting of the data $\mathbf{d}$ [equation (3.2.8)]. Comparison of the results of this test with the actual parameters (Table 1) shows that all three parameters in both layers were found with good accuracy.

Another example, this time for a three-layer VTI model with a more complicated shape of the interfaces is shown in Figure 3.4 and Table 2. The data vector $\mathbf{d}(\mathbf{Y}, n)$ was determined from the traveltimes computed at 600 common midpoints located along two lines with a spacing of 15 m. The accuracy of parameter estimation on noise-contaminated data (Table 2) is comparable to that in the example from Table 1. Therefore, in this case, P-wave reflection traveltimes provide sufficient information for the inversion in the depth domain.

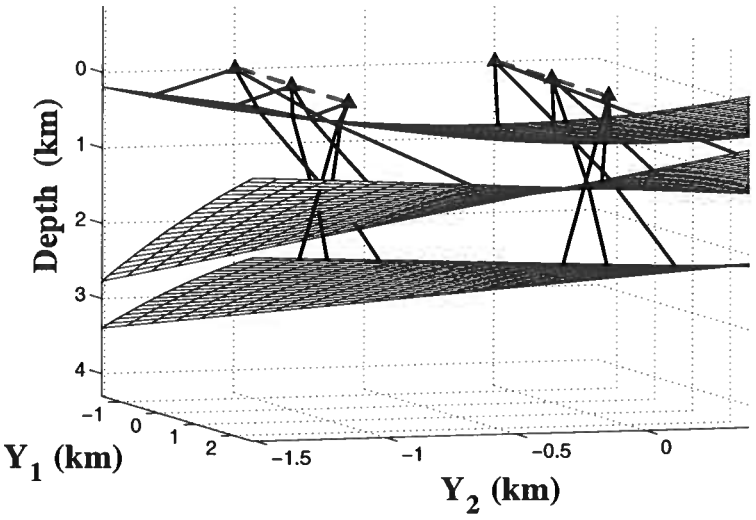

FIG. 3.4. The three-layer VTI model used in the inversion with several zero-offset rays. Common midpoints are located on the two gray dashed lines.

3.4 Summary

Here, we applied P-wave moveout inversion to more complicated VTI media with irregular interfaces. To compute azimuthally dependent NMO velocity in such models, we extended the theory of NMO-velocity surfaces (Grechka and Tsvankin, 2002a) by deriving a correction for the interface curvature. The new methodology generates NMO ellipses over arbitrary anisotropic media with irregular interfaces by tracing a *single* zero-offset ray per CMP. This modeling algorithm, which is several orders of magnitude faster than 3-D two-point ray tracing, provides a foundation for efficient traveltime inversion.

We studied the feasibility of the interval-parameter estimation using singular value decomposition (SVD) followed by the tomographic-style inversion of noisy data. The input parameters for the inversion include P-wave zero-offset traveltimes and az-

imuthally dependent NMO velocities (i.e., NMO ellipses) acquired at a number of common midpoints over the study area. In contrast to media with planar interfaces discussed in Chapter 2, in some cases, for VTI models with irregular interfaces it is possible to reconstruct the model in depth from P-wave reflection traveltimes alone. Interface curvature increases the angle coverage of reflected rays, which helps to constrain the parameters of the anisotropic velocity field. Only if the anisotropy is close to elliptical, does the depth scale become poorly constrained by P-wave data regardless of the interface shape, which agrees with the results of Dellinger and Muir (1988).

The most critical assumption that ensured the success of the inversion procedure is that the model is composed of *homogeneous* layers. Allowing for a variation in the VTI parameters within some of the layers may prevent us from resolving the three principal components of the model: anisotropy, irregular interfaces, and lateral velocity variation. Even for isotropic models with irregular interfaces and laterally varying velocity, the traveltime inversion is generally nonunique (Goldin, 1986).

Although this "stacking-velocity tomography" of PP data excludes the far-offset information (i.e., nonhyperbolic moveout) from analysis, this approach has important advantages over conventional reflection tomography. The first advantage is related to the computational efficiency. Since the NMO ellipse (and, therefore, the multiazimuth, multioffset hyperbolic moveout as a whole) can be computed by tracing only one zero-offset ray for each reflection event at a given CMP location, the number of rays to be computed in forward modeling is reduced by at least an order of magnitude. This makes anisotropic traveltime tomography computationally feasible. Another advantage deals with the more complicated but likewise more important issue of uniqueness of anisotropic traveltime tomography. Due to the multi-parameter nature

of anisotropic media, it is often difficult to determine directly from the traveltimes which parameters (or parameter combinations) are constrained in a given acquisition geometry. In contrast, the NMO velocities, which are described by semi-analytical expressions for arbitrary anisotropy (Grechka et al., 1999a), provide a much simpler way of approaching this problem. Also, the weak anisotropy approximations of the NMO velocities give an easy-to-use tool for examining the sensitivity of the traveltime data to various anisotropic coefficients (see the expressions for SV-waves in the next chapter.)

Chapter 4

PARAMETER ESTIMATION IN TI MEDIA USING PP AND PS OR SS DATA

In contrast to the more complicated moveout of mode conversions, reflection traveltime of pure SS-waves is symmetric with respect to zero offset and, for moderate offset-to-depth ratios, can be described by the NMO ellipse (Grechka and Tsvankin, 2000). Hence, the theory of the NMO ellipses and NMO-velocity surfaces (Grechka et al., 1999b; Grechka and Tsvankin, 2002a) is directly applicable to SS-wave moveout.

The methodology of Chapter 2 is generalized here for the combination of conventional-spread PP and SS data. The tomographic algorithm operates with the NMO ellipses, zero-offset traveltimes, and reflection slopes (measured on zero-offset time sections) of PP-waves and the reconstructed SS-waves. We examine a wide range of homogeneous TI models with a tilted symmetry axis (including horizontal transverse isotropy, or HTI) and establish the conditions needed for stable parameter estimation. Then we apply the method to layered TI models to estimate the interval medium parameters and the shapes of interfaces from multicomponent reflection data.

4.1 Multicomponent stacking-velocity tomography

The goal of the tomographic algorithm introduced here is to estimate the anisotropic subsurface model using wide-azimuth measurements of stacking velocities of PP- and SS-waves on moderate-length CMP spreads (i.e., spreadlengths that are smaller than the reflector depth).

We implement the multicomponent tomographic procedure for TI media composed of homogeneous layers separated by plane or smooth curved interfaces. The algorithm includes the following main steps:

1. Picking PP and PS traveltimes from pre-stack 3-D data volumes and identifying the PP and PS events reflected from the same interface. In general, both split converted waves (PS_1 and PS_2) can be used.

2. Computing the traveltimes of the pure SS reflections from PP and PS data using the method of Grechka and Tsvankin (2002b).

3. Performing azimuthal velocity analysis to obtain the NMO ellipses of the PP- and SS-waves.

4. Inverting of the NMO ellipses, zero-offset traveltimes, and reflection slopes for the interval anisotropic parameters by extending the approach of Chapter 2 to multicomponent data.

The data vector used in the inversion for an N-layered TI medium is given by

$$\boldsymbol{d}(Q, \boldsymbol{Y}, n) \equiv \{\tau_Q(\boldsymbol{Y}, n), \boldsymbol{p}_Q(\boldsymbol{Y}, n), \boldsymbol{W}_Q(\boldsymbol{Y}, n)\}, \tag{4.1.1}$$

where $Q = PP$ or SS is the mode type (only $SVSV$-waves are included in the algo-

rithm described in this chapter), $\boldsymbol{Y} = [Y_1, Y_2]$ is the CMP coordinate, $n = 1, 2, ..., N$ is the reflector number, τ is the zero-offset traveltime, $\boldsymbol{p}$ is the reflection slope on zero-offset time sections, and $\boldsymbol{W}$ are the 2×2 matrices (Grechka and Tsvankin, 1998b) describing the NMO ellipses.

The goal is to find the model vector $\boldsymbol{m}$ that contains the interval medium parameters and the coefficients of the polynomials used to describe the model interfaces. For TI media with an unknown tilt of the symmetry axis, the inversion of PP- and $SVSV$-waves can be used to estimate six interval parameters – the symmetry-direction P- and S-wave velocities V_{P0} and V_{S0}, anisotropic coefficients ϵ and δ, and two angles responsible for the symmetry-axis orientation.

In general, the parameter-estimation algorithm is organized in the same way as that introduced for PP-waves in Chapter 2 (Grechka et al., 2002a). For a given set of trial interval anisotropic parameters, the zero-offset traveltimes τ_Q and the reflection slopes $\boldsymbol{p}_Q$ are used to compute the one-way zero-offset rays for all reflection events. Then the interfaces for the trial model are reconstructed by fitting 2-D polynomials to the termination points of the zero-offset rays. Finally, the interval parameters are obtained by minimizing the objective function

$$\mathcal{F}(\boldsymbol{m}) \equiv \sum_{Q,\boldsymbol{Y},n} ||\boldsymbol{W}_Q^{\text{calc}}(\boldsymbol{Y}, n, \boldsymbol{m}) - \boldsymbol{W}_Q^{\text{meas}}(\boldsymbol{Y}, n)|| \,. \tag{4.1.2}$$

The norms in the function (4.1.2) contain the differences between the computed and measured NMO ellipses $\boldsymbol{W}$ for all modes and all reflectors at each CMP location.

4.2 Inversion of PP and SS data for a homogeneous TI medium

Consider the model of a single homogeneous TI layer with a planar lower boundary (horizontal or dipping) and arbitrary orientation of the symmetry axis. The problem addressed here is whether or not wide-azimuth reflection traveltimes of PP- and SS-waves (i.e., SV reflections reconstructed from PP and PSV data) can be inverted for the symmetry-direction velocities V_{P0} and V_{S0}, the parameters ϵ and δ, and the axis orientation. It is convenient to study the feasibility of parameter estimation by applying the weak-anisotropy approximation to the NMO ellipses and zero-offset traveltimes.

The analysis has to be performed for P-waves only, because any kinematic signature of SV-waves for weak transverse isotropy can be obtained from the corresponding P-wave signature by making the following substitutions: $V_{P0} \rightarrow V_{S0}$, $\delta \rightarrow \sigma$, and $\epsilon \rightarrow 0$ (Tsvankin, 2001; see Table 1). A similar substitution rule for SH-waves is $V_{P0} \rightarrow V_{S0}$, $\delta \rightarrow \gamma$, and $\epsilon \rightarrow \gamma$. SH-wave anisotropy, however, is elliptical, and most kinematic signatures can be obtained in closed form without applying the weak-anisotropy approximation.

4.2.1 VTI layer

In the weak-anisotropy limit, the substitution rules for different modes hold for the processing parameters as well. Alkhalifah and Tsvankin (1995) showed that P-wave time processing in VTI media with a laterally homogeneous overburden above the target reflector is governed by the zero-dip P-wave NMO velocity

P	SV	SH
Kinematic parameters		
V_{P0}	V_{S0}	V_{S0}
ϵ	0	γ
δ	σ	γ
Processing parameters (VTI)		
η	$-\sigma$	0
$V_{P,\mathrm{nmo}}$	$V_{SV,\mathrm{nmo}}$	$V_{SH,\mathrm{nmo}}$

Table 1. Correspondence between the parameters responsible for the kinematic signatures of P-, SV-, and SH-waves in weakly anisotropic TI media.

$$V_{\mathrm{nmo},P} = V_{P0}\sqrt{1+2\,\delta} \tag{4.2.3}$$

and the anellipticity coefficient

$$\eta \equiv \frac{\epsilon-\delta}{1+2\,\delta}\,. \tag{4.2.4}$$

Note that this result is valid for any strength of velocity anisotropy. Time processing of SV-waves for weakly anisotropic VTI media is then controlled by the zero-dip SV-wave NMO velocity

$$V_{\mathrm{nmo},SV} = V_{S0}\sqrt{1+2\,\sigma} \tag{4.2.5}$$

and the parameter $-\sigma/(1+2\sigma)$, which plays the role of η. Time processing of elliptically anisotropic SH-waves requires just the NMO velocity

$$V_{\mathrm{nmo},SH} = V_{S0}\sqrt{1+2\,\gamma} \tag{4.2.6}$$

because the quantity corresponding to η goes to zero. This result stems from the fact that isotropic time-processing algorithms are entirely valid for elliptical anisotropy (Dellinger and Muir, 1988; Alkhalifah and Tsvankin, 1995).

Suppose the data include multi-azimuth (3-D) traveltimes of PP- and PSV-reflections from a planar dipping interface below a homogeneous VTI layer. Without losing generality, the dip plane of the reflector is assumed to coincide with the coordinate plane $[x_1, x_3]$ (i.e., the x_1-axis points in the dip direction). Applying the methodology of Grechka and Tsvankin (2002b), one reconstructs the traveltimes of the pure SS ($SVSV$) reflections and uses azimuthal moveout analysis (Grechka and Tsvankin, 1999b) to obtain the NMO ellipses of both PP- and SS-waves.

Since the model is symmetric with respect to the dip plane, the axes of the NMO ellipses have to be aligned within the dip and the strike directions (Grechka and Tsvankin, 1998b). The linearized approximations for the semi-axes of the PP-wave NMO ellipse are given by (Alkhalifah and Tsvankin, 1995; Grechka and Tsvankin, 1998b):

$$V^2_{\text{nmo},P,\text{dip}}(p_{P,1}) = \frac{V^2_{\text{nmo},P}}{1-y_P}\left[1+\frac{2\,\eta\,y_P}{1-y_P}\left(6-9\,y_P+4\,y_P^2\right)\right] \tag{4.2.7}$$

and

$$V^2_{\text{nmo},P,\text{strike}}(p_{P,1}) = V^2_{\text{nmo},P}\left[1+2\,\eta\,y_P\,(2-y_P)\right]\,, \tag{4.2.8}$$

where

$$y_P \equiv p^2_{P,1}\,V^2_{\text{nmo},P}\,.$$

$p_{P,1}$ is the horizontal slowness component of the PP-wave zero-offset ray (or the dip component of the reflection slope), and the strike component $p_{P,2} = 0$. Equations (4.2.7) and (4.2.8) can be inverted for the zero-dip NMO velocity $V_{\text{nmo},P}$ and

the anisotropic coefficient η if the reflector dip (expressed through the slope $p_{P,1}$) is not too small. The inversion of the PP-wave NMO ellipse using the exact equations is discussed by Grechka and Tsvankin (1998b), who find that the dip should exceed 25° to ensure stable estimation of η.

The weak-anisotropy approximations for the dip and strike components of the SV-wave NMO velocity can be obtained directly from equations (4.2.7) and (4.2.8) using the conversion rule from Table 1:

$$V^2_{\text{nmo},P,\text{dip}}(p_{SV,1}) = \frac{V^2_{SV,\text{nmo}}}{1-y_{SV}}\left[1-\frac{2\,\sigma\,y_{SV}}{1-y_{SV}}\left(6-9\,y_{SV}+4\,y^2_{SV}\right)\right], \tag{4.2.9}$$

$$V^2_{\text{nmo},SV,\text{strike}}(p_{SV,1}) = V^2_{\text{nmo},SV}\left[1-2\,\sigma\,y_{SV}\,(2-y_{SV})\right]. \tag{4.2.10}$$

Here

$$y_{SV} = p^2_{SV,1}\,V^2_{\text{nmo},SV},$$

$p_{SV,1}$ is the horizontal slowness component of the SS-wave zero-offset ray (or the dip component of the reflection slope), and the strike component $p_{SV,2} = 0$.

Similar to the parameter estimation for PP-waves described above, equations (4.2.9) and (4.2.10) can be inverted for $V_{\text{nmo},SV}$ and σ. Furthermore, substituting $V_{\text{nmo},SV}$ and σ into equation (4.2.5) yields the shear-wave vertical velocity V_{S0}. Then the zero-offset traveltime and the reflection slope of the SS reflection can be used to reconstruct the depth and dip of the reflector.

Next, let us demonstrate that adding this information to the traveltimes of PP-waves is sufficient for estimating the vertical velocity V_{P0} and the anisotropic coefficients ϵ

and δ. We can find δ from $V_{\mathrm{nmo},P}$ and V_{P0}, and ϵ from η. The equation of a planar reflecting interface can be written in the form

$$\boldsymbol{b} \cdot (\boldsymbol{x} - \boldsymbol{r}_P) = 0\,, \tag{4.2.11}$$

where $\boldsymbol{b}$ is the unit vector normal to the reflector, and $\boldsymbol{r}_P$ defines the PP-wave zero-offset reflection point. Similarly, for the zero-offset SS ray reflected from the point $\boldsymbol{r}_{SV}$, one has

$$\boldsymbol{b} \cdot (\boldsymbol{x} - \boldsymbol{r}_{SV}) = 0\,. \tag{4.2.12}$$

Combining equations (4.2.11) and (4.2.12) yields

$$\boldsymbol{b} \cdot \boldsymbol{r}_P = \boldsymbol{b} \cdot \boldsymbol{r}_{SV}\,. \tag{4.2.13}$$

The vector $\boldsymbol{b}$ can be replaced in equation (4.2.13) by the normalized (so that the magnitude is equal to unity) slowness vectors of the zero-offset PP and SS rays because the slowness (or phase-velocity) vectors of pure-mode reflections at zero offset are orthogonal to the reflector. Also, the vectors $\boldsymbol{r}_P$ and $\boldsymbol{r}_{SV}$ can be expressed through the group-velocity vectors of the PP- and SS-waves by putting the origin of the coordinate system at the CMP location. Further linearization of equation (4.2.13) in the anisotropic parameters leads to

$$\begin{aligned} &\tau_P\, V_{\mathrm{nmo},P} \left[1 - \delta \left(1 - p_{P,1}^2\, V_{\mathrm{nmo},P}^2\right) + \eta\, p_{P,1}^4\, V_{\mathrm{nmo},P}^4\right] = \\ &\tau_{SV}\, V_{\mathrm{nmo},SV} \left[1 - \sigma \left(1 - p_{SV,1}^2\, V_{\mathrm{nmo},SV}^2 + p_{SV,1}^4\, V_{\mathrm{nmo},SV}^4\right)\right]\,, \end{aligned} \tag{4.2.14}$$

where τ_P and τ_{SV} are the zero-offset traveltimes of the PP- and SS-arrivals. Note that the quantities on the left- and right-hand sides of equation (4.2.14) comply with the

conversion rule in Table 1. The result equivalent to equation (4.2.14) can be obtained by using Snell's law for the zero-offset P- and SV-rays instead of equations (4.2.11) and (4.2.12).

Although the parameters $V_{\mathrm{nmo},P}$, $V_{\mathrm{nmo},SV}$, η, and σ, which can be obtained from the PP- and SS-wave NMO ellipses [equations (4.2.7)–(4.2.10)], are sufficient to find the vertical velocities V_{P0}, V_{S0} and the coefficients ϵ and δ, the inversion of the PP-wave NMO ellipse requires reflector dips of at least 25° (Alkhalifah and Tsvankin, 1995; Grechka and Tsvankin, 1998b). The NMO ellipse of the SS-wave is more sensitive to dip than is that of the PP-wave because of relatively large values of σ. Supplementing equations (4.2.7)–(4.2.10) with equation (4.2.14) adds another constraint on the anisotropic parameters and helps to obtain an accurate result for dips less than 25°. Indeed, the numerical tests below confirm that dips as small as 15° are sufficient for stable estimation of the VTI parameters for this simple model.

Figure 4.1 illustrates application of the methodology to noise-contaminated wide-azimuth PP and SS ($SVSV$) traveltimes (the SS traveltimes are supposed to have been computed from the PP and SS data) generated for a homogeneous VTI layer with the lower boundary dipping at 15°. We perform nonlinear inversion (the Gauss-Newton method) based on the exact equations for the NMO ellipses, zero-offset traveltimes, and reflection slopes using the objective function given in equation (4.1.2). The dots in Figure 4.1 mark the estimated VTI parameters for different realizations of the noise added to the input data. The standard deviations in the inverted parameters (2% for V_{P0} and V_{S0}, 0.03 for ϵ, and 0.02 for δ) indicate that the noise does not get amplified by the parameter-estimation procedure, so the inversion is reasonably stable. In the presence of higher levels of noise in the data, it can be difficult to estimate the anisotropic parameters. Note that the estimated values of ϵ and δ

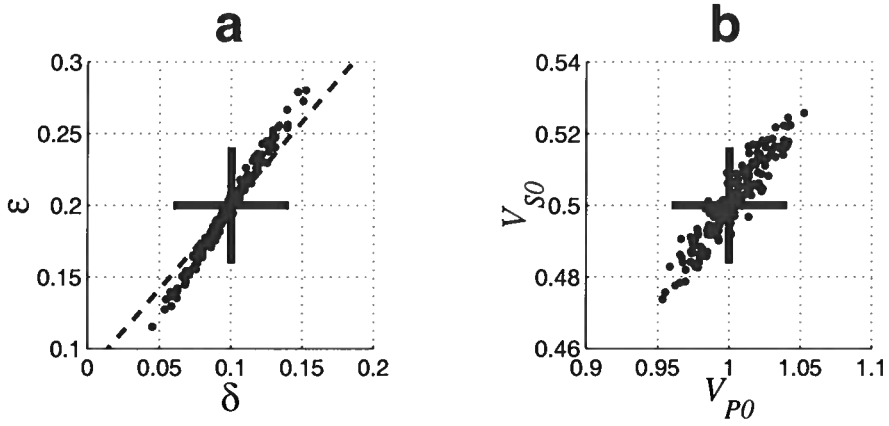

FIG. 4.1. Results (dots) of the joint inversion of PP and SS ($SVSV$) data for a single VTI layer above a planar dipping reflector. The correct layer parameters are marked by the crosses, the reflector dip is 15°, and the velocities are given in km/s. The dashed line on plot (a) corresponds to the correct value of η. The data were contaminated by Gaussian noise with standard deviations equal to 2% for the NMO velocities and 1% for the zero-offset traveltimes and reflection slopes.

cluster near the line of the correct parameter $\eta \approx \epsilon - \delta$ because the difference $\epsilon - \delta$ is well-constrained by both PP and SS traveltimes (Tsvankin and Grechka, 2000, 2002).

The only parameter of VTI media that cannot be obtained from P and SV data is γ – the anisotropic coefficient responsible for the elliptical anisotropy of SH-waves. Tsvankin and Grechka (2000, 2002) showed that γ can be determined from converted PSH-waves, which are generated for all azimuthal directions outside the dip plane. The methodology introduced here can be applied to the estimation of γ from the NMO ellipses of pure SH-wave reflections computed from PP and PSH data. Thus, with the combination of P-, PSV-, and PSH-wave reflection traveltimes, one can estimate all five VTI parameters and build the VTI model in the depth domain.

4.2.2 HTI layer

Contreras et al. (1999) studied the inversion of wide-azimuth PP data for HTI media and showed that the symmetry-direction velocity V_{P0}, the coefficients ϵ and δ (or $\epsilon^{(V)}$ and $\delta^{(V)}$; see Tsvankin, 1997b), and the azimuth β of the horizontal symmetry axis can be found from the PP-wave NMO ellipses from a horizontal and a dipping reflector. However, the need to use two different dips for each depth interval makes this algorithm difficult to implement in practice. In contrast, the approach presented here is designed to estimate the HTI parameters using the NMO ellipses of PP- and $SS(SVSV)$-waves from a single reflector that can be either horizontal or dipping. Note that by "SV-wave" we always mean the mode polarized in the plane formed by the slowness vector and the symmetry axis. If the symmetry axis is horizontal or tilted, this plane is no longer necessarily vertical, but we still prefer to keep the notation commonly used for VTI media.

The inversion for a *horizontal* HTI layer confirms the results of Tsvankin (1997b) who pointed out that the combination of wide-azimuth PP- and SS-wave moveout data is sufficient for estimating the symmetry-direction velocities V_{P0} and V_{S0} and the parameters ϵ and δ. For this model, the velocities V_{P0} and V_{S0} can be found directly from surface data because they are equal to the corresponding NMO velocities measured in the direction orthogonal to the symmetry axis (i.e., in the isotropy plane). Typical results of inverting noise-contaminated PP and SS traveltimes for the parameters of a horizontal HTI layer are shown in Figure 4.2. The standard deviations in all estimated parameters, including the azimuth β of the symmetry axis (not shown on the plot), are quite small; the deviation in β is 0.6°.

To examine the inversion for *dipping* interfaces, we adapted for SS-waves the weak-

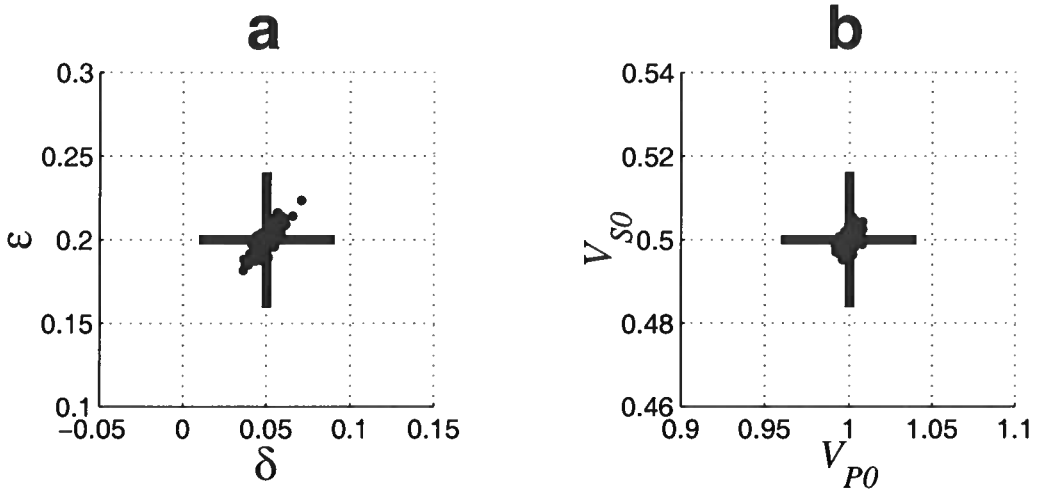

FIG. 4.2. Results of the inversion (dots) of PP and SS traveltime data for a horizontal HTI layer using the exact equations for the NMO ellipses. The data were contaminated by noise with the same standard deviations as those in Figure 4.1. The correct layer parameters are marked by the crosses. V_{P0} and V_{S0} are the velocities in the symmetry-axis direction in km/s.

anisotropy approximations for PP-wave NMO ellipses given by Contreras et al. (1999). Both the theoretical analysis and the inversion based on the exact equations (see Figure 4.3) show that the parameter estimation remains stable for the whole range of dips from 0° to 90°.

The dots of the estimated parameter values in Figure 4.3 form smaller clouds than those in Figure 4.1, which indicates that the inversion of dipping events for HTI media is more stable than that for VTI media. As discussed above, for a horizontal VTI layer the inversion for V_{P0}, V_{S0}, ϵ, and δ cannot be performed at all. It should also be mentioned that the inversion algorithm for HTI media converges much more rapidly to the correct model than it does for VTI media.

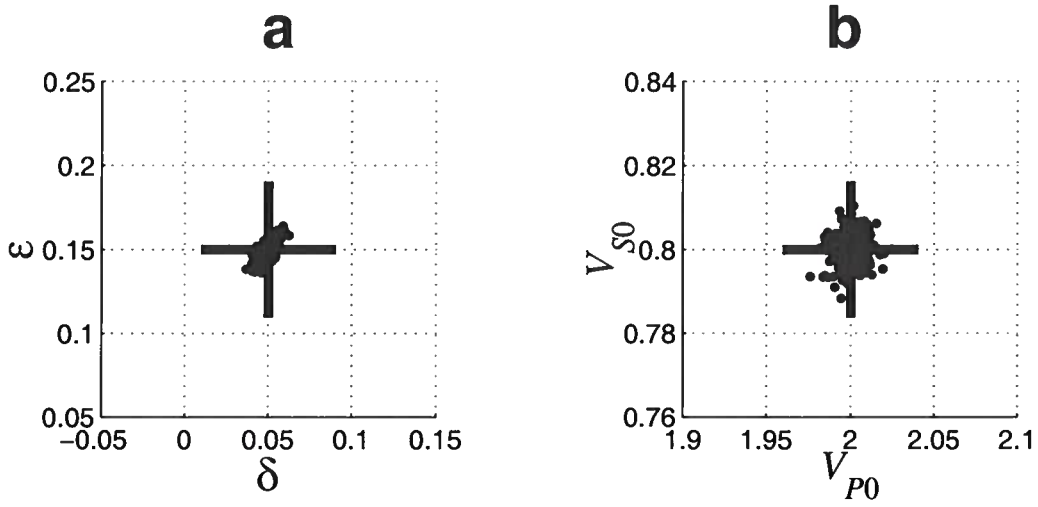

FIG. 4.3. Same as Figure 4.2 but for an HTI layer with the lower boundary dipping at 25°. The azimuth of the symmetry axis with respect to the dip plane is $\beta = 40°$; the standard deviation in β is 0.8°.

4.2.3 TTI layer

The parameter-estimation problem for transverse isotropy with a tilted symmetry axis (TTI media) includes only one additional unknown compared to the HTI case – the tilt ν. This, however, makes the inversion substantially more ill-posed than that for HTI media because the pure-mode NMO ellipses are nonlinear functions of ν, even for weak anisotropy. Grechka and Tsvankin (2000) found a nonlinear dependence on the tilt in the weak-anisotropy approximations for the PP-wave NMO ellipse in TTI media. Therefore, the misfit (objective) function for the NMO ellipses that has to be minimized in the nonlinear inversion may have local minima, even for weak anisotropy. The multimodal nature of the misfit function may require several inversions starting from different points in the model space.

The schematic summary of the numerical results in Figure 4.4 illustrates the influence

of the tilt of the symmetry axis and reflector dip on the uniqueness of parameter estimation in TTI media. This plot should not be interpreted in a strict quantitative sense because the criteria used to identify the areas of unique and nonunique inversion are somewhat loose. In general, the line dividing those areas corresponds to standard deviations in ϵ and δ of about 0.03 (for the errors in the input data given in the caption of Figure 4.1). However, the quality of the inversion results also depends on parameters not shown in Figure 4.4 such as the magnitude of ϵ and δ and the azimuth of the symmetry axis. In particular, the inversion becomes more stable with increasing absolute values of ϵ and δ.

It should be emphasized that in generating Figure 4.4 we assumed that the orientation of the symmetry axis is unknown, even if the model is HTI or VTI. Therefore, the stability of the inversion results for both VTI and HTI is lower than in the two previous sections on VTI and HTI media where the tilt of the symmetry axis was fixed at the correct value. Still, Figure 4.4 shows that even if the HTI model is not assumed in advance, it can be accurately reconstructed from reflection data despite some problems caused by the more complicated topology (e.g., multiple local minima) of the objective function. Even when the objective function has complex structure, it is possible to apply more sophisticated tools to find the global optima (Scales et al., 1992).

In contrast, when the tilt of the symmetry axis is small (i.e., the model is close to VTI) and unknown, the inversion remains ambiguous for all reflector dips. As the symmetry axis deviates further from the vertical, the inversion becomes more stable (for a fixed dip) and can be performed for an increasingly wide range of dips (Figure 4.4). For HTI media (see above) the inversion is feasible even for a horizontal reflector and without *a priori* knowledge of the tilt.

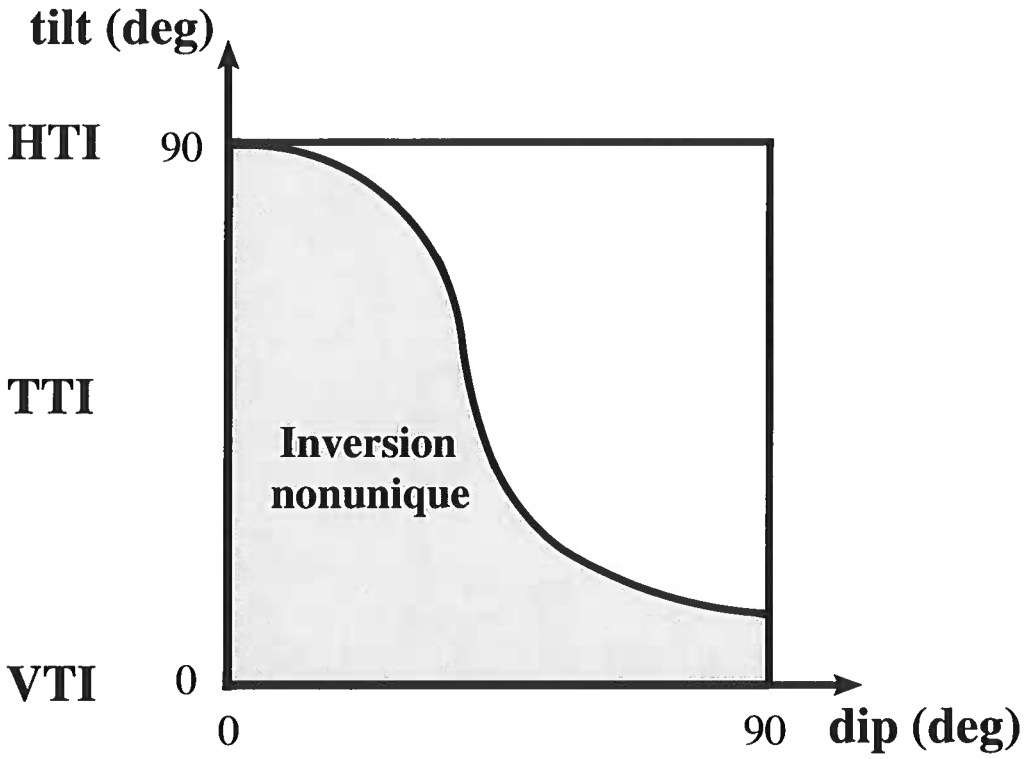

FIG. 4.4. Uniqueness of depth-domain parameter estimation in TI media for the full range of reflector dips and tilt angles of the symmetry axis. The tilt and azimuth of the symmetry axis were unknown (i.e., they were estimated from the inversion) for all models, including VTI and HTI media.

Figure 4.5 displays inversion results typical for models located within the area of nonuniqueness in Figure 4.4 near the area's boundary. As in the previous examples, we inverted the NMO ellipses, zero-offset traveltimes, and reflection slopes of the PP- and SS-waves after contaminating the input data with Gaussian noise. Although the obtained parameters scatter around the correct values, the standard deviations (4% in V_{P0} and V_{S0}, 0.05 in ϵ, 0.04 in δ, 1.5° in β, and 0.8° in ν) indicate a substantial error amplification in the estimation of V_{P0}, V_{S0}, ϵ, and δ.

The stability of the inversion for TTI models may be enhanced by including SH-wave NMO ellipses and zero-offset traveltimes to the input data. The traveltimes

of pure SH reflections can be obtained using PSH converted waves generated for source-receiver azimuths outside of the vertical symmetry plane(s) of the model.

Thus, multicomponent (PP and PS), multiazimuth reflection data can be inverted for the parameters of homogeneous TI media for a range of reflector dips and tilts of the symmetry axis. The highest stability is observed for near-horizontal orientations of the symmetry axis, while for a vertical and tilted symmetry axis the inversion generally becomes more stable with increasing dip.

4.3 Parameter estimation for layered TI media

Here, the multicomponent tomographic procedure is applied to TI models containing homogeneous layers with arbitrary orientation of the symmetry axis separated by smooth curved interfaces. Suppose the input data include wide-azimuth traveltimes of PP- and PSV-waves reflected from two interfaces of the VTI model in Figure 4.6. After computing the traveltimes of the pure SS reflections using the $PP + PS = SS$ method (Grechka and Tsvankin, 2002b), one collects the PP and SS data into CMP gathers for azimuthal velocity analysis. Estimating the PP- and SS-wave NMO ellipses and zero-offset traveltimes at four CMP locations (Figure 4.6) yields the data vector from equation (4.1.1). Then for each trial set of interval anisotropic parameters one finds the interfaces and computes the objective function, which is then minimized in the nonlinear inversion algorithm.

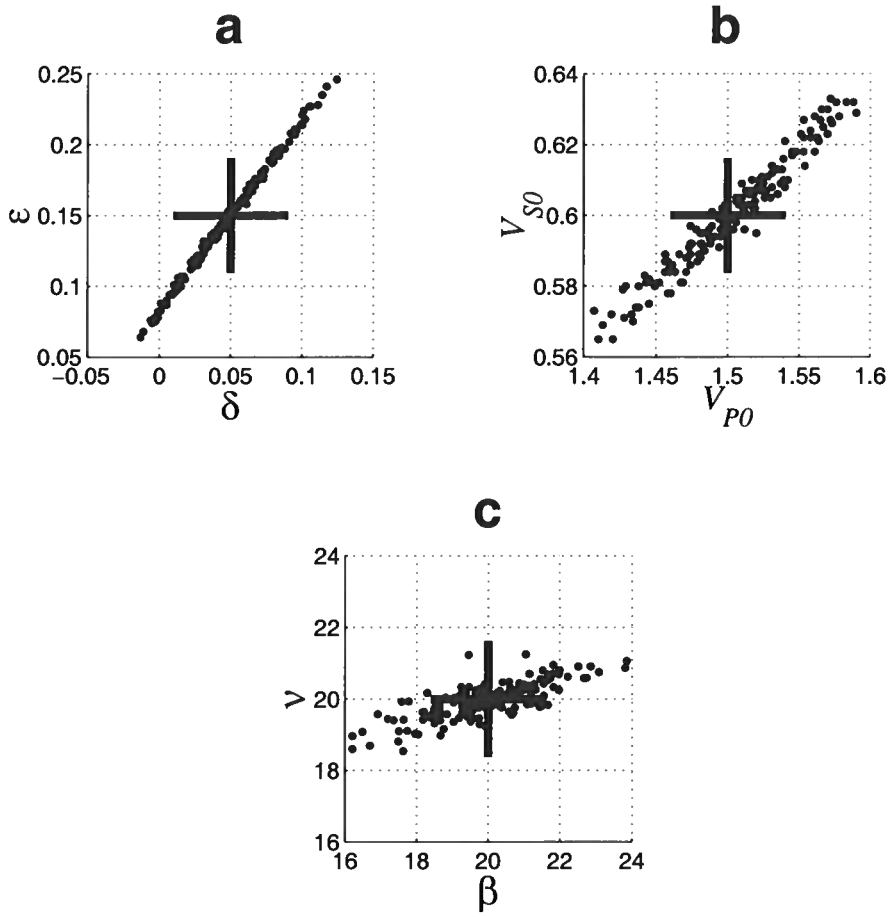

FIG. 4.5. Results of the inversion (dots) of PP and SS traveltime data for a dipping TTI layer (the dip is 30°). The data were contaminated by noise with the same standard deviations as those in Figure 4.1. The correct layer parameters are marked by the crosses. The velocities in the symmetry-axis direction V_{P0} and V_{S0} are in km/s, the tilt ν and azimuth β of the symmetry axis are in degrees (β is measured with respect to the dip plane).

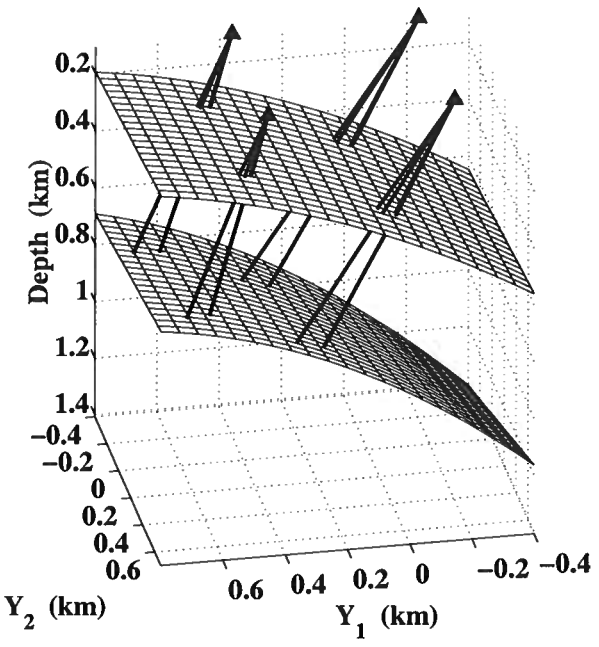

FIG. 4.6. Zero-offset rays of the PP- and $SS(SVSV)$-waves recorded at four CMP locations over a model composed of two homogeneous VTI layers. The layer parameters are: $V_{P0,1} = 2.0$ km/s, $V_{S0,1} = 0.8$ km/s, $\epsilon_1 = 0.15$, $\delta_1 = 0.05$; $V_{P0,2} = 2.5$ km/s, $V_{S0,2} = 0.9$ km/s, $\epsilon_2 = 0.20$, $\delta_2 = 0.10$.

4.3.1 Numerical examples

The input data from Figure 4.6 were distorted by Gaussian noise with standard deviation of 2% for the NMO velocities and 1% for the zero-offset traveltimes and reflection slopes. The inversion results for 100 realizations of the input data in Figure 4.7 indicate that the noise does not get amplified by the parameter-estimation procedure. The standard deviations in the inverted parameters are less than 1% for V_{P0} and V_{S0} (not shown), and about 0.01 for ϵ and δ.

Note that neither of the interfaces in the model from Figure 4.6 has steep segments. In agreement with the results for a single layer, the high sensitivity of the SS-wave

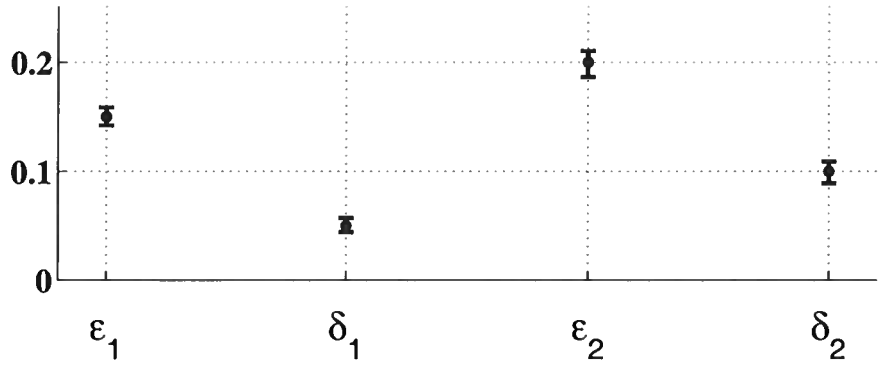

FIG. 4.7. Results of stacking-velocity tomography for the model in Figure 4.6. The dots mark the exact values of the anisotropic parameters, the bars correspond to the ± standard deviation in each parameter.

NMO ellipse to reflector dip and the addition of the ratio of the zero-offset PP and SS traveltimes [equation (4.2.14)] ensures the stability of the joint inversion of wide-azimuth PP and SS data for dips of 15°-20°. Including the NMO ellipses of the SH-waves may help to constrain the anisotropic coefficient γ and build a complete VTI model in depth.

Figures 4.8 and 4.9 show the tomographic inversion of multicomponent data for a more complicated model that includes VTI, HTI and TTI layers. Despite the larger error bars for deeper horizons, the overall stability of the algorithm is satisfactory. A general increase in errors with depth, caused by the relatively small contribution of the deeper layers to the reflection traveltimes from their lower boundaries, is typical for all kinematic inversion algorithms. Also, although we do not differentiate the Dix-type formula explicitly to obtain the interval anisotropic coefficients, errors in the parameters of the upper layers still propagate into the inversion results for the deeper part of the section.

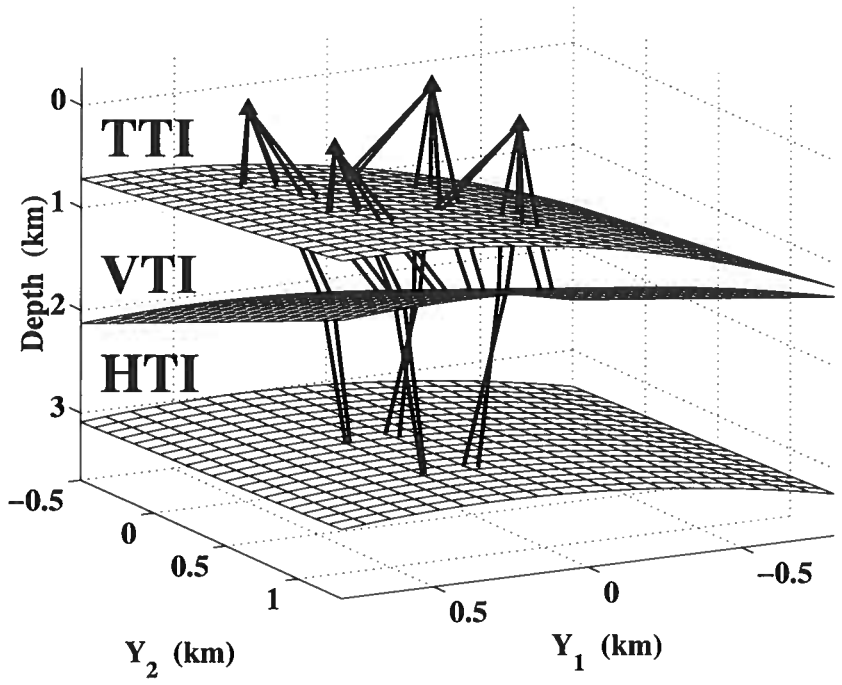

FIG. 4.8. Zero-offset rays of the PP- and $SS(SVSV)$-waves for a model composed of TTI, VTI and HTI layers.

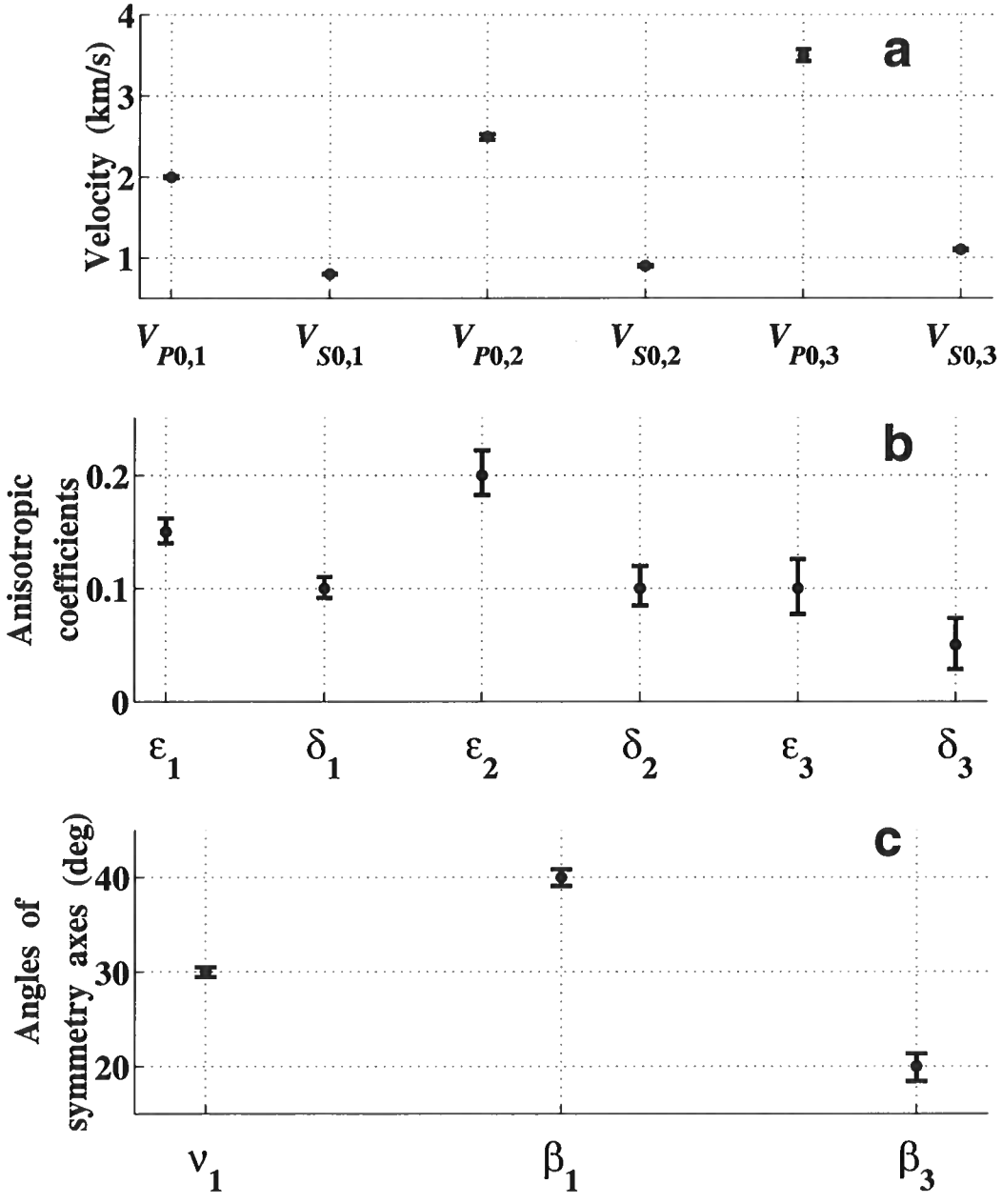

FIG. 4.9. Results of stacking-velocity tomography for the model in Figure 4.8.

4.3.2 Influence of errors in the symmetry type

In the examples discussed above, we assumed that the type of anisotropy (i.e., anisotropic symmetry) in each layer was known in advance. Since this is not typically the case in practice, it is instructive to examine the inversion of error-free data using an intentionally incorrect anisotropic symmetry in one of the layers.

We specified a TI model composed of two VTI layers on top of an HTI layer (Figure 4.10) with the interval parameters listed in the top row of Table 2. Then the tomographic parameter estimation was performed under the erroneous assumption that the bottom (HTI) layer has VTI symmetry (the second row in Table 2). As expected, the inversion produced seriously distorted values of the symmetry-direction velocities $V_{P0,3}$ and $V_{S0,3}$ and the anisotropic coefficients ϵ_3 and δ_3. It is interesting that the parameters of the two upper layers are also inaccurate because the error in the bottom layer gets distributed throughout the whole model to minimize the objective function (4.1.2). Hence, errors can propagate not only downward (accumulate with depth) but also upward, albeit with a substantially smaller amplification.

An implication of this observation is that it might be preferable to perform tomographic inversion in a layer-stripping mode, starting with estimation of the parameters of the subsurface layer using the most shallow PP and PS reflections. Then, fixing the obtained values, one can determine the interval parameters of the second layer by inverting the traveltimes from its bottom, and the parameter-estimation procedure continues downward. In addition to eliminating upward error propagation from the deeper layers, the stripping approach is computationally efficient because only a few unknowns need to be found at each stage (i.e., for each layer). The main shortcoming of layer stripping is its implicit reliance on the assumption that the reflections from

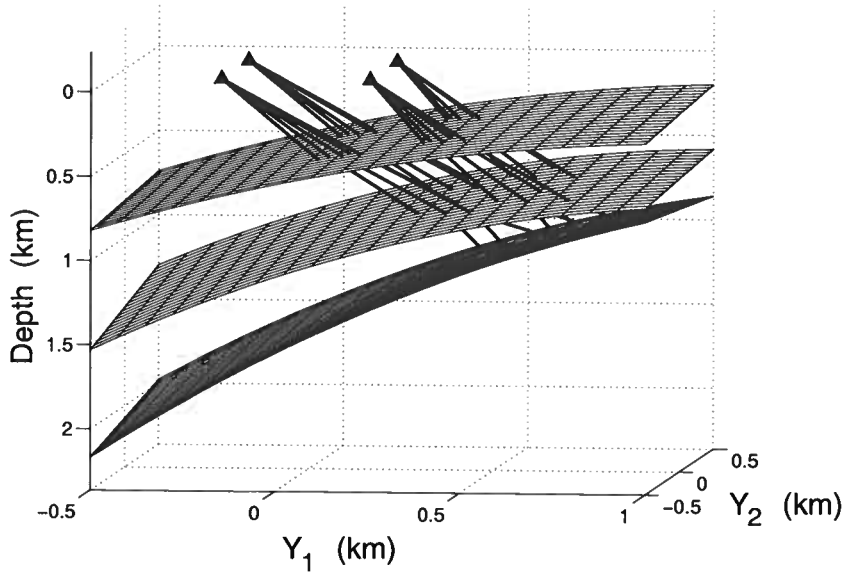

FIG. 4.10. Zero-offset rays of the PP- and $SS(SVSV)$-waves for a model composed of two VTI layers on top of an HTI layer. The interval parameters are listed in the top row of Table 2.

$V_{P0,1}$	$V_{S0,1}$	ϵ_1	δ_1	β_1	$V_{P0,2}$	$V_{S0,2}$	ϵ_2	δ_2	$V_{P0,3}$	$V_{S0,3}$	ϵ_3	δ_3	β_3
Correct model parameters													
2.00	0.80	0.15	0.05	–	2.50	0.90	0.20	0.10	3.50	1.10	0.20	0.05	30
Inversion assuming the bottom layer to be VTI													
1.98	0.79	0.16	0.06	–	2.53	0.90	0.18	0.09	3.00	1.28	0.35	0.34	–
Inversion assuming the top layer to be HTI													
2.23	0.94	0.01	0.03	101	2.61	0.92	0.15	0.02	3.55	0.92	0.24	−0.09	34

Table 2. Correct parameters of the model composed of two VTI layers on top of an HTI layer (top row) and the inversion results based on erroneous assumptions about the symmetry in one of the layers.

the bottom of the layer contain full information about the layer parameters. Since this is not always the case for PP-waves in TI media (Le Stunff et al., 2001; Grechka et al., 2002a), one can expect that for some models the layer-stripping method may create ambiguity in the joint inversion of PP and PS data.

In the second test, the top (VTI) layer was assumed to have HTI symmetry. Then, in addition to the expected significant errors in the parameters of the top layer, we also obtained distorted parameters in both bottom layers (see the third row in Table 2). This test underscores the importance of choosing the right type of anisotropy in the overburden, because any errors in the shallow part of the section will propagate through the whole model.

An alternative to *assuming* a specific type of anisotropy is to adopt the more general tilted TI (or even orthorhombic) model from the outset of the inversion. The correct type of anisotropy can then be identified from the determined orientation of the symmetry axis (for TTI media) or relationships between the estimated anisotropic coefficients (for orthorhombic media). However, the need to estimate the tilt of the symmetry axis often reduces the stability of the algorithm, especially for models close to VTI.

4.3.3 Influence of heterogeneity

Accurate reconstruction of vertical and lateral velocity variations is the main challenge in reflection tomography. For example, even for isotropic media certain types of vertical velocity variations within layers can never be resolved from the reflection traveltimes, no matter how the inversion is performed (e.g., Goldin, 1986). Given the complexity of this problem for anisotropic media, the discussion here is limited to

a numerical example illustrating the errors in the estimated anisotropic parameters caused by heterogeneity unaccounted for in the inversion.

Suppose we attempt to estimate the parameters of the VTI overburden for the model from Table 2 (Figure 4.10) using only the reflections from the second interface. The effective parameters of the overburden then change both vertically (since it actually consists of two layers) and laterally (because the first interface is not horizontal). While the vertical variations of the VTI parameters cannot be resolved without including reflections from the first interface, one can try to estimate the lateral parameter variations by performing the inversion for a range of CMP coordinates Y_1 (Figure 4.10).

The data $\boldsymbol{d}(Q, \boldsymbol{Y}, n)$ [equation (4.1.1)] were generated for $Q = P, SV$, $n = 2$ and CMP coordinates $Y_1 = [-0.6, -0.4, \ldots, 0.8, 1.0]$ km, $Y_2 = [-0.2, 0.2]$ km. In each inversion, we used four adjacent common midpoints (that form the corners of a rectangle) and assigned the estimated anisotropic coefficients to the center of the rectangle. Treating the overburden as a single homogeneous VTI layer yields the parameters displayed in Figure 4.11. Clearly, all estimated quantities change laterally because the variations in the dip and depth of the interfaces make the overburden laterally heterogeneous. It is interesting that while the effective vertical velocities V_{P0} and V_{S0} (Figure 4.11a, b) can be regarded as certain averages of the interval velocities, the best-fit anisotropic coefficients ϵ and δ often lie *outside* the range of the corresponding interval coefficients (Figure 4.11c, d).

This result, which seems to be puzzling, can be explained by the fact that we operate with a variety of different averages in stacking-velocity tomography. The "average," or effective parameters produced by the tomographic inversion process are not nec-

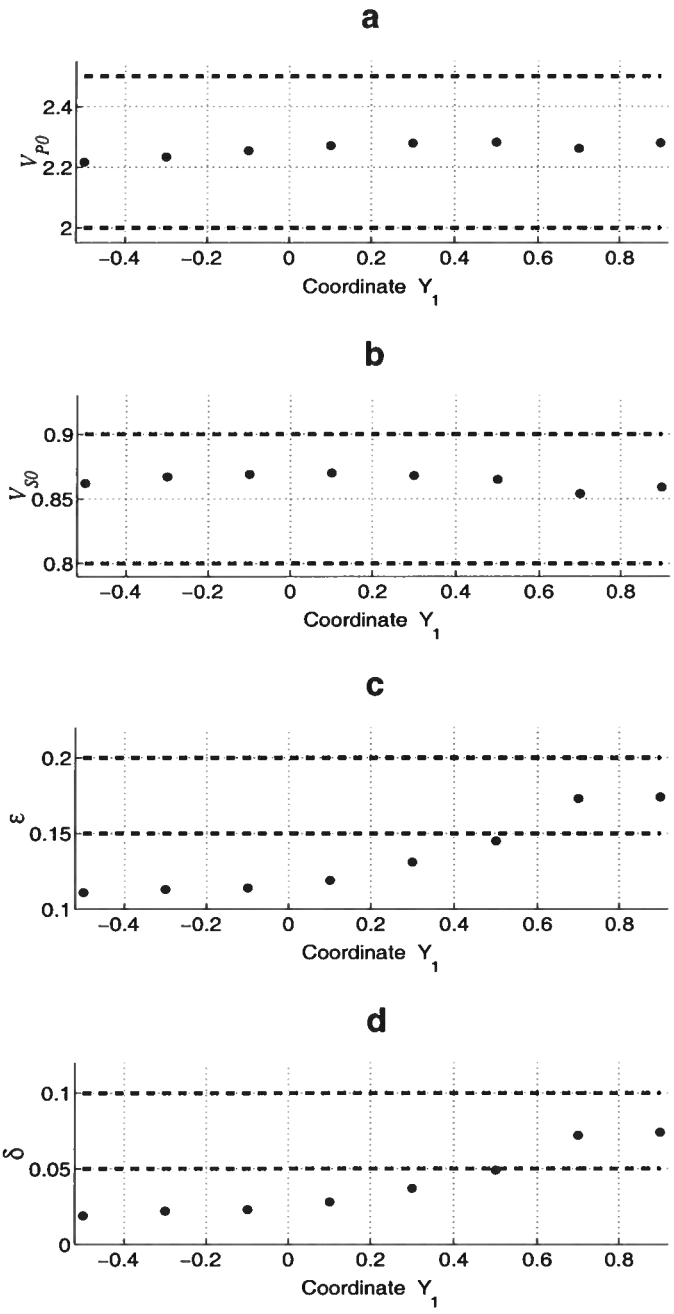

FIG. 4.11. Effective parameters (dots) of the VTI overburden estimated using the reflections from the second interface in Figure 4.10. The correct parameters of the VTI layers that make up the overburden are marked by the dashed lines. The coordinate Y_1 (in km) is defined in the text.

essarily bounded by the minimum and maximum interval values. As an example, in Appendix H it is shown that the effective anisotropic coefficient δ derived from the PP-wave NMO velocity for a stack of plane homogeneous VTI layers can often exceed the maximum interval coefficient δ_n. In the special case of isotropy, when all $\delta_n = 0$, the effective δ above vertically heterogeneous media is always positive (Grechka and Tsvankin, 2002d). The model in Figures 4.10 and 4.11 contains curved interfaces, and the averaging procedure is more complicated than that in Appendix H. The results, however, are similar in that in both cases the effective values lie outside of the range of the corresponding interval quantities.

The results in Figure 4.11 can be considered as a consequence of upscaling, performed implicitly to obtain effective values of the anisotropic parameters. Replacing the actual heterogeneous medium with the homogeneous model providing the best fit to the data may result in effective properties that cannot be obtained by straightforward arithmetic averaging of the corresponding interval (local) properties.

4.4 Summary

This chapter extends stacking-velocity tomography to multicomponent (P and S) data. The tomographic algorithm is designed to invert wide-azimuth traveltimes of P and S-wave reflections for the interval parameters of transversely isotropic media. Although the method does not operate directly with converted PS-waves, it can still be applied in multicomponent ocean-bottom surveys. Prior to the velocity analysis, PS data are combined with the PP-wave moveout from the same interface to compute the reflection traveltimes of SS-waves using the model-independent kinematic technique of Grechka and Tsvankin (2002b).

The SS traveltime, in contrast to the more complicated moveout of converted waves, is symmetric with respect to zero offset and (on conventional-length spreads) can be described by the NMO velocity. Azimuthal semblance analysis of PP and SS traveltimes on CMP gathers produces the NMO ellipses (i.e., azimuthally varying stacking velocities) and zero-offset traveltimes that serve as the input to the tomographic inversion.

Here, the multicomponent tomography was implemented for a stack of transversely isotropic layers separated by smooth interfaces. The detailed analysis for a homogeneous TI medium and numerical testing for layered models show that for a range of reflector dips and tilt angles of the symmetry axis, the combination of PP and PSV (or $SVSV$) data can be used to build anisotropic models for depth processing. The most notable exception is horizontally layered VTI media, for which even long-spread (nonhyperbolic) moveout of PP- and PSV-waves does not constrain the vertical velocities (Grechka and Tsvankin, 2002c).

The chapter also discusses upscaling, which is one of the most complicated issues in estimating the elastic properties of the subsurface. we demonstrated with simple examples that the values of the so-called effective parameters, which provide the best fit to our data, might actually lie outside of the range determined by the maximum and minimum of the interval values for the same parameter. It is important to mention that the quantities obtained from the inversion always bear an imprint of the assumed model. Some subsurface features, such as the short-scale velocity heterogeneity, can be never incorporated into our models because of the limited resolution of seismic data. Those features, however, do influence the data and can also change the values of the estimated parameters in a way that is difficult to control.

Chapters 2 and 3 show that for a certain class of layered VTI models with dipping or irregular interfaces, PP-wave reflection data alone can be used to reconstruct the depth scale of the model and parameters ϵ and δ. This inversion, however, breaks down if the difference $\epsilon - \delta$ is small, and the anisotropy is close to elliptical (Dellinger and Muir, 1988). As follows from the results of this chapter, combining PP- and SS-waves resolves this ambiguity (in the presence of mild reflector dip) because the velocity function of SV-waves in elliptical media is purely isotropic. Extending the argument of Dellinger and Muir (1988), one can state that the isotropic velocity function of SV-waves, which have equal vertical and horizontal velocities, does not allow the medium "stretching" in the vertical direction that causes the depth ambiguity.

Chapter 5

APPLICATION OF MOVEOUT INVERSION TO PHYSICAL MODEL DATA

Here, we use data from a physical modeling experiment to study the feasibility of anisotropic parameter estimation in TTI media from measurements obtained from actual velocity analysis of CMP gathers. The physical model was built by Leslie and Lawton (1996) to simulate typical reflection data acquired in overthrust areas of the Alberta Foothills in Canada. Using the general theory of normal moveout in laterally heterogeneous media (Grechka and Tsvankin, 2002a), we show how one might invert P-wave NMO velocities and zero-offset traveltimes for the full set of the anisotropic parameters of the TTI layer. Information about the anisotropic parameter ϵ is contained in the moveout of a reflected wave that crosses one of the dipping TI blocks. The accuracy of the inversion procedure is dependent on the errors in the NMO velocities obtained from conventional hyperbolic semblance analysis of reflection events.

5.1 Physical modeling

The 2-D physical model built at the University of Calgary by Leslie and Lawton (1996) was designed to mimic overthrust structures typical for the Central Alberta

Foothills in Canada (Figure 5.1). Four blocks of Phenolic laminate (shaded in gray in Figure 5.1) were glued together to form a bending transversely isotropic layer with symmetry axis orthogonal to the bedding. The Phenolic material, which is known to be orthorhombic, was cut in the direction of one of the symmetry planes to produce a 2-D TI sheet with the parameters believed to be typical for shales in the Foothills. The P-wave velocities in the symmetry direction ($V_0 = 2925$ m/s) and isotropy plane ($V_{90} = 3365$ m/s) yield the anisotropic parameter $\epsilon = 0.16$, while the second relevant anisotropic coefficient, δ, is equal to 0.08 (Cheadle et al., 1991). The TI layer was embedded in a purely isotropic Plexiglass material (white in Figure 5.1) with the P-wave velocity $V_{\text{iso}} = 2740$ m/s.

An ultrasonic P-wave reflection survey with the acquisition parameters given in Table 1 was acquired by Leslie and Lawton (1996) at the top of the model. The time section for the smallest offset in the data (Figure 5.2) shows a false anticline structure at a time of approximately 1.4 s. This pull-up of the bottom of the model is caused by the combined influence of the higher velocity and anisotropy in the Phenolic blocks. Leslie and Lawton (1998) presented a series of pre-stack depth migrations of these data and showed that the bottom interface cannot be flattened without taking anisotropy into account. Their results also suggest that P-wave reflection traveltimes might contain sufficient information for obtaining the model parameters needed for the anisotropic imaging. Here, we use the theoretical results discussed in Grechka and Tsvankin (2002a) to perform a parameter-estimation procedure based entirely on surface P-wave data.

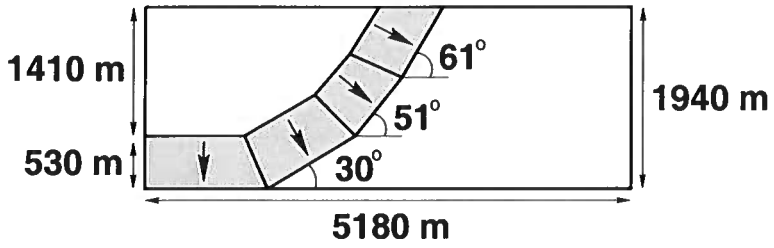

FIG. 5.1. Physical model of an anisotropic thrust sheet (after Leslie and Lawton, 1996). In each block of the bending TI layer, the symmetry axis (marked by the arrows) is perpendicular to the layer boundaries. The distances are scaled by a factor of 10,000.

Number of common midpoints	504
CMP spacing	10 m
Offset spacing	20 m
Minimum offset	200 m
Maximum offset	2000 m

Table 1. Acquisition parameters used by Leslie and Lawton (1996).

5.2 Parameter estimation

5.2.1 Assumptions about the model

First, we present the assumptions needed to avoid ambiguities in the inversion of the available set of measurements for the model parameters.

(i) All blocks making up the model in Figure 5.1 are assumed to be *homogeneous*. Allowing for lateral velocity variation leads to trade-offs between the parameters, such as those described for VTI media by Grechka (1998).

(ii) All four TTI blocks are made of the same material with the symmetry axis *orthogonal* to the bedding within each block. In other words, we have to assume that the model contains a homogeneous, bending TTI layer. Without this assumption,

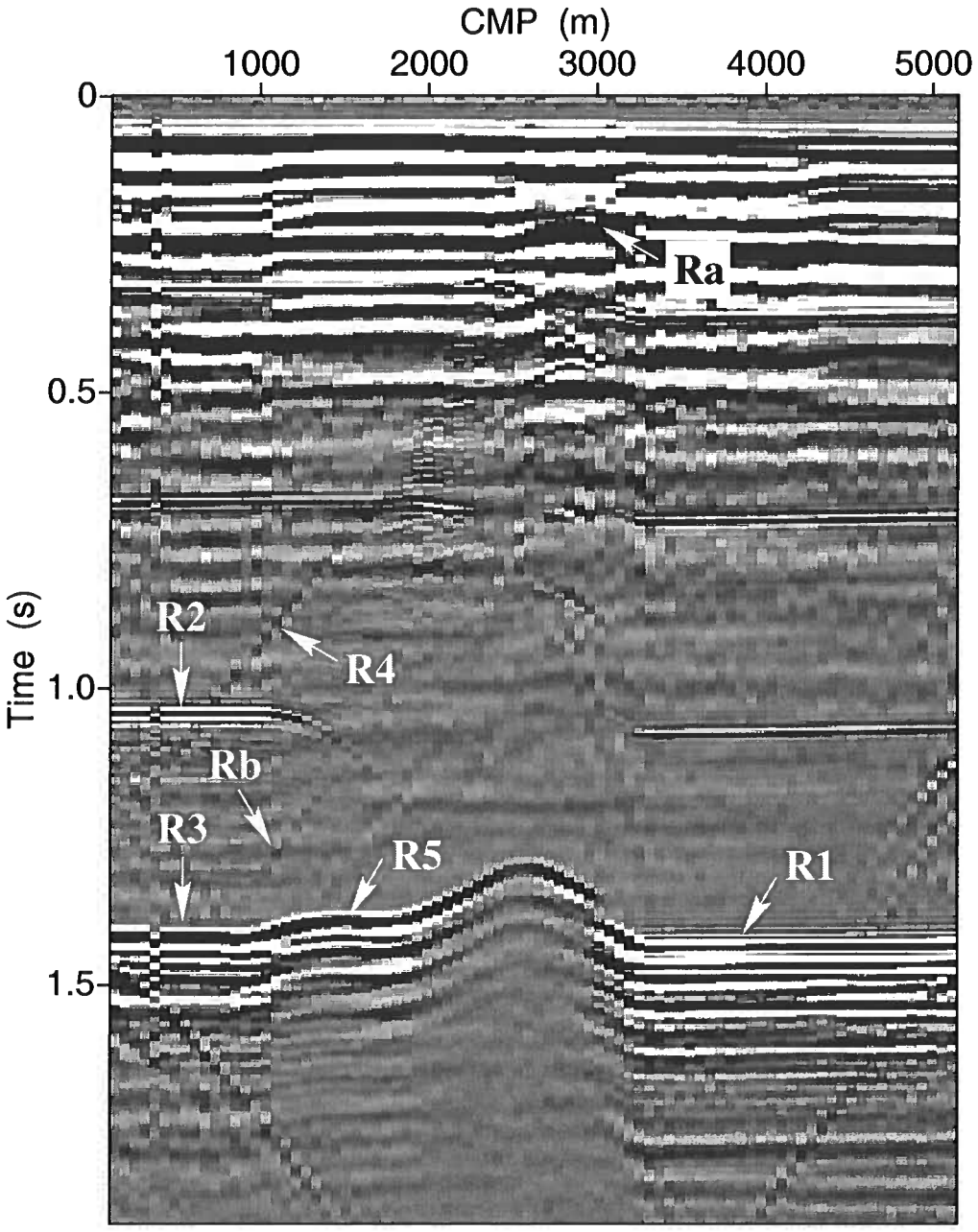

FIG. 5.2. Common-offset (200 m) time section of the reflection data acquired over the model from Figure 5.1. The arrows mark the reflection events (**R1** – **R5**, **Ra**, and **Rb**) discussed in the text.

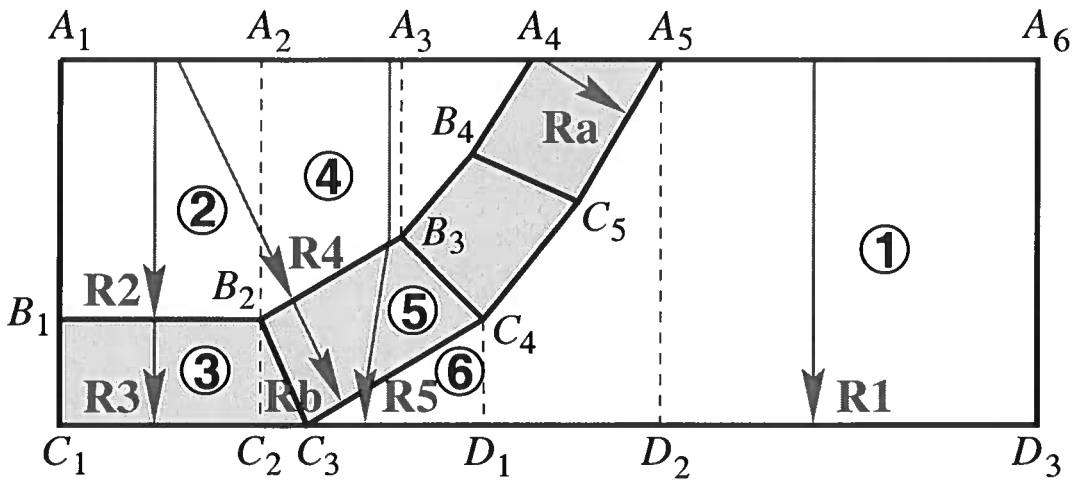

FIG. 5.3. Cartoon of the zero-offset rays for reflection events **R1** – **R5**, **Ra** and **Rb**. Numbers in the circles denote model blocks.

the number of independent parameters cannot be reduced to that constrained by the data.

(iii) The Plexiglass blocks (white in Figure 5.1) are *isotropic*. This assumption cannot be verified using the available data because the same P-wave reflection traveltimes could have been generated for an *elliptically anisotropic* surrounding medium with the same value of the NMO velocity from horizontal reflectors (e.g., Alkhalifah and Tsvankin, 1995).

(iv) The reflector at the bottom of the model is *horizontal*, which implies that the anticline structure at approximately 1.4 s in Figure 5.2 is caused by the spatial velocity variations in the overburden. This assumption would not be needed if we could measure the NMO velocity for the reflection event marked as **Ra** in Figure 5.2.

5.2.2 Inversion for the anisotropic parameters

Under the above assumptions, it is possible to obtain all model parameters in the depth domain using the zero-offset traveltimes and normal-moveout velocities of reflection events **R1** – **R5** marked in Figures 5.2–5.4. We also attempted to process reflections **Ra** and **Rb**, which carry information about the parameters of the TTI layer. However, as discussed below, the NMO velocities and zero-offset traveltimes of these events could not be picked with sufficient accuracy.

5.2.3 Reflection R1

Let us begin with event **R1** reflected from the segment $[D_2D_3]$ beneath the isotropic homogeneous Plexiglass layer [Figure 5.3; see assumptions **(i)** and **(iii)**]. The two-way zero-offset traveltime τ_{R1} and NMO velocity $V_{\mathrm{nmo,\,R1}} = V_{\mathrm{iso}}$ were picked from several semblance panels similar to the one shown in Figure 5.4a. Then we computed the mean values of the traveltimes and velocities over several common-midpoint (CMP) locations and obtained $\tau_{\mathrm{R1}} = 1.437$ s and $V_{\mathrm{nmo,R1}} = 2742$ m/s. The standard deviations attributable to picking inaccuracies, based on the spatial extent of the semblance maxima, were estimated at 0.004 s and 30 m/s (Figure 5.4a). The zero slope of reflection event **R1** in Figure 5.2 indicates that the segment $[D_2D_3]$ is horizontal. Its depth, which is supposed to be constant under the whole model according to assumption **(iv)**, is $z = z_{\mathrm{R1}} = \tau_{\mathrm{R1}}\, V_{\mathrm{R1}}/2 = 1969 \pm 22$ m. Here and below, the notation $a = b \pm c$ means that the quantity a is estimated to be equal to b with the error bar or standard deviation c. The computed depth z is somewhat greater than the correct value (1940 m) because it was determined using the traveltimes picked from

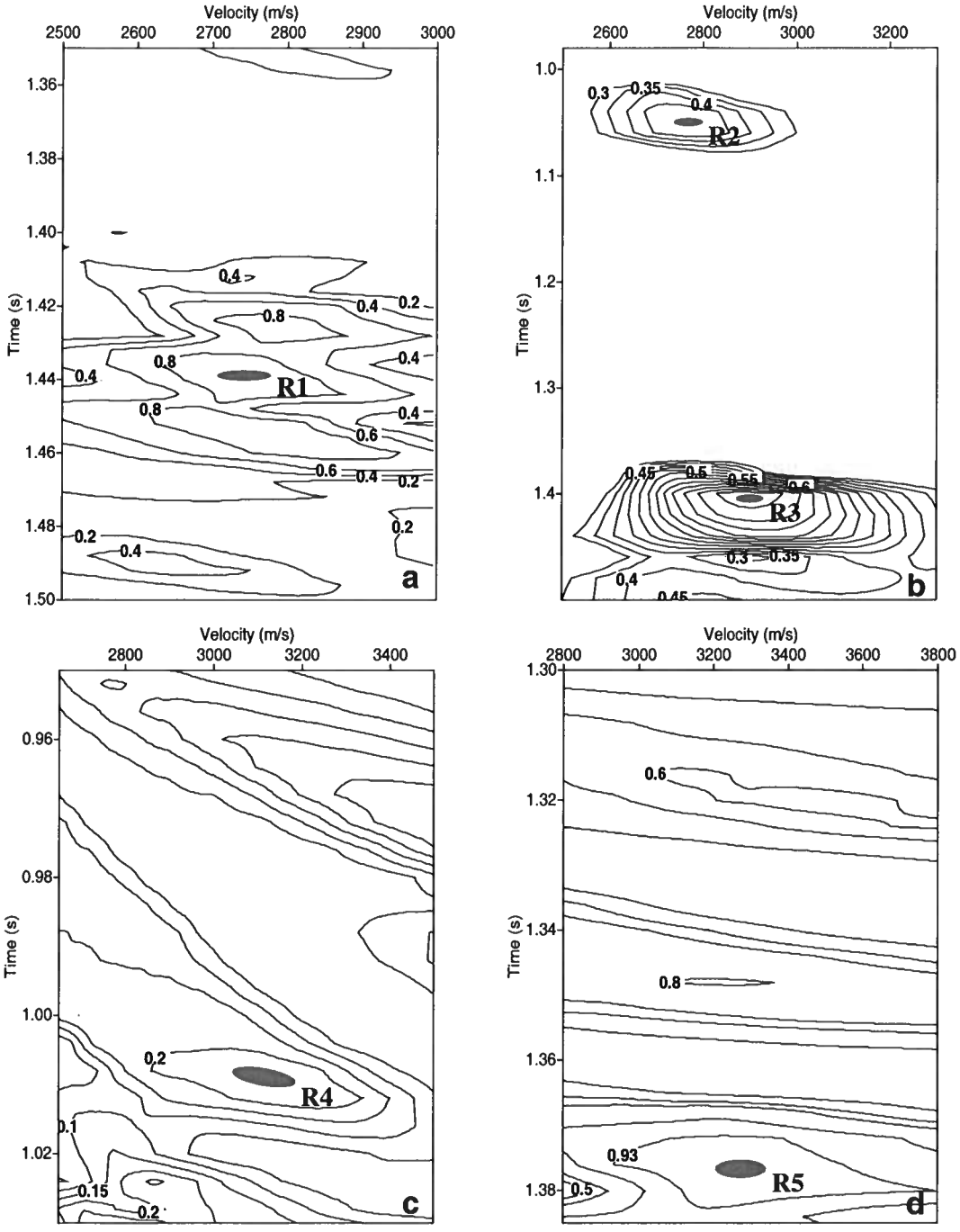

FIG. 5.4. Semblance contours at CMP locations 3780 m (a), 630 m (b), 680 m (c), and 1480 m (d). The gray areas mark the spatial dimensions of the semblance maxima used to pick the traveltimes and NMO velocities of reflection events **R1** – **R5**.

the semblance maxima rather than from the actual first breaks.

5.2.4 Reflection R2

Event **R2** is similar to **R1** because it also represents a reflection from the bottom of an isotropic homogeneous layer. Since the NMO velocity $V_{\mathrm{nmo,\,R2}} = V_{\mathrm{iso}} = 2750 \pm 40$ m/s (Figure 5.4b) practically coincides with $V_{\mathrm{nmo,\,R1}}$, and the Plexiglass is supposed to be homogeneous and isotropic, blocks 1 and 2 (Figure 5.3) are taken to be made of the same material. On the time section from Figure 5.2, reflection **R2** can be seen as a horizontal event at the traveltime $\tau_{\mathrm{R2}} = 1.05 \pm 0.008$ s; this implies that segment $[B_1 B_2]$ is horizontal. The estimated thickness of block 2 is $z_{\mathrm{R2}} = \tau_{\mathrm{R2}}\, V_{\mathrm{R2}}/2 = 1444 \pm 19$ m.

5.2.5 Reflection R3

Reflection **R3**, generated at the bottom of the horizontal block 3 (Figure 5.2 and 5.3), contains information about the NMO velocity V_{nmo} in the TTI layer. The symmetry axis in block 3 is vertical (i.e., the block has the VTI symmetry), and V_{nmo} is related to the symmetry-direction velocity V_0 as (Thomsen, 1986)

$$V_{\mathrm{nmo}} = V_0 \sqrt{1 + 2\,\delta}\,. \tag{5.2.1}$$

Since ray **R3** propagates through a laterally homogeneous medium [assumption **(i)**], the interval NMO velocity can be found using the conventional Dix (1955) differenti-

ation

$$V_{\text{nmo}} = \sqrt{\frac{\tau_{\text{R3}} V^2_{\text{nmo,R3}} - \tau_{\text{R2}} V^2_{\text{nmo,R2}}}{\tau_{\text{R3}} - \tau_{\text{R2}}}} = 3192 \pm 104\,\text{m/s}, \tag{5.2.2}$$

where $\tau_{\text{R3}} = 1.405 \pm 0.004$ s and $V_{\text{nmo,R3}} = 2870 \pm 20$ m/s are the measured zero-offset traveltime and normal-moveout velocity for reflection **R3** (Figure 5.4b). Under assumption **(iv)**, the depth of segment $[C_1C_2]$ is equal to that of segment $[D_2D_3]$: $z_{\text{R3}} = z_{\text{R1}} = 1969 \pm 22$ m. Therefore, one can compute the vertical velocity in block 3 as

$$V_0 = 2\,\frac{z_{\text{R3}} - z_{\text{R2}}}{\tau_{\text{R3}} - \tau_{\text{R2}}} = 2963 \pm 157\,\text{m/s}. \tag{5.2.3}$$

Then, using equation (5.2.1), one finds the anisotropic coefficient $\delta = 0.09 \pm 0.06$. As a result, conventional moveout analysis near the left edge of the model yields two parameters of the TTI layer: the symmetry-direction velocity V_0 and the coefficient δ. The other relevant anisotropic parameter, ϵ, still has to be found.

5.2.6 Reflection Ra

To determine the parameter δ from horizontal events, we again had to assume that the bottom interface is horizontal. An alternative way of estimating δ without such an assumption is to use the NMO velocity $V_{\text{nmo,Ra}}$ of the reflection from the dipping segment $[A_5C_5]$ (**Ra** in Figure 5.3). $V_{\text{nmo,Ra}}$ represents the following function of the velocities V_0, V_{nmo}, and the half-slope p_{Ra} of reflection **Ra** on the zero-offset section (Grechka and Tsvankin, 1998b):

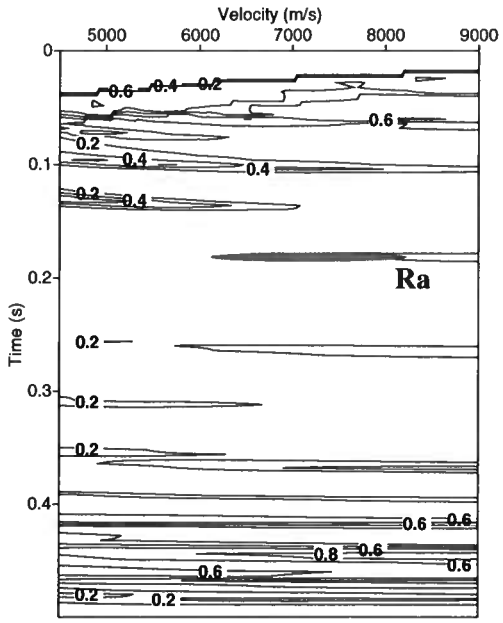

FIG. 5.5. Semblance contours for reflection **Ra** at CMP location 2810 m. The gray area indicates the range of possible moveout-velocity picks.

$$V_{\mathrm{nmo,\,Ra}} = \frac{V_{\mathrm{nmo}}}{\sqrt{1 - p_{\mathrm{Ra}}^2 V_0^2}}\,. \tag{5.2.4}$$

The NMO velocity of event **Ra** needs to be picked on a CMP gather within the relatively short segment $[A_4A_5]$. To avoid receiver locations outside this segment, offsets larger than approximately 500 m have to be muted. Even after the muting, however, accurate picking of the NMO velocity $V_{\mathrm{nmo,\,Ra}}$ is practically impossible because of the absence of small offsets up to 200 m (Table 1) and relatively large (for such a shallow reflection) offset increment. The steep interface $[A_5C_5]$ also contributes to the high uncertainty in the velocity picking. The above factors lead to strongly elongated semblance contours in Figure 5.5, which yield error bars for $V_{\mathrm{nmo,\,Ra}}$ of at least 1000 m/s. Clearly, such an accuracy is inadequate for the subsequent estimation of the anisotropic coefficients.

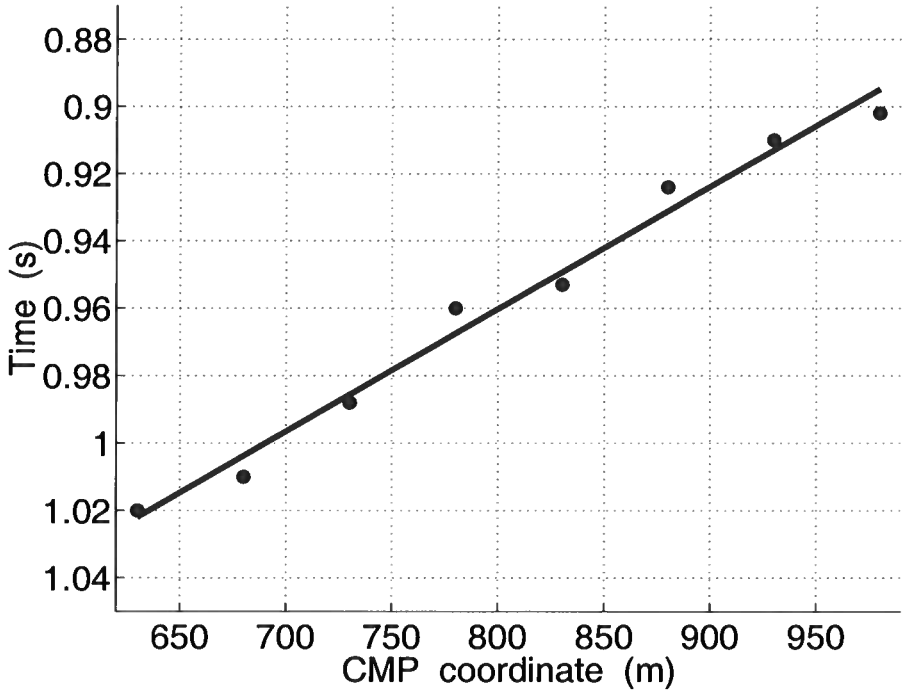

FIG. 5.6. Two-way zero-offset traveltimes (dots) for reflection **R4** and their approximation with a straight line. The standard deviation of the picked traveltimes from the straight line is 0.006 s.

5.2.7 Reflections R4 and Rb

Reflections **R4** and **Rb** form parallel straight lines on the time section in Figure 5.2, indicating that segments $[B_2B_3]$ and $[C_3C_4]$ of the TTI block 5 in Figure 5.3 are parallel to each other. Approximation of the picked zero-offset traveltimes of event **R4** by a straight line (Figure 5.6) allows us to obtain the half-slope $p_{\mathrm{R4}} = 1.82\times10^{-4}$ s/m. The NMO velocity $V_{\mathrm{nmo,\,R4}} = 3120\pm70$ m/s corresponding to the semblance maximum in Figure 5.4c satisfies the isotropic relationship (Tsvankin, 2001)

$$V_{\mathrm{nmo,\,R4}} = \frac{V_{\mathrm{iso}}}{\sqrt{1 - p_{\mathrm{R4}}^2\, V_{\mathrm{iso}}^2}}\,. \tag{5.2.5}$$

Although equation (5.2.5) is also valid for elliptically anisotropic media with the zero-dip NMO velocity V_{iso}, we use assumption **(iii)** to identify blocks 2 and 4 as part of the homogeneous isotropic section of the model. Then the dip ϕ of segment $[B_2B_3]$ is given by

$$\phi = \sin^{-1}\left(p_{\mathrm{R4}}\, V_{\mathrm{iso}}\right) = 29.8^\circ \pm 0.4^\circ\,. \tag{5.2.6}$$

Neither the traveltime τ_{Rb} nor the NMO velocity $V_{\mathrm{nmo,\,Rb}}$ of event **Rb** could be picked because of its low amplitude (Figure 5.2). However, this does not hamper parameter estimation because both τ_{Rb} and $V_{\mathrm{nmo,\,Rb}}$ are controlled by the model parameters that can be estimated from other reflections. For example, the traveltime τ_{Rb} could have been used to obtain the thickness $z_\perp$ of block 5 (Figure 5.3) in the direction normal to interfaces $[B_2B_3]$ and $[C_3C_4]$. Since the symmetry axis is also perpendicular to these interfaces [assumption **(ii)**],

$$z_\perp = V_0\,\frac{\tau_{\mathrm{Rb}} - \tau_{\mathrm{R4}}}{2}\,. \tag{5.2.7}$$

Instead of using equation (5.2.7), however, one finds the thickness $z_\perp$ from the traveltime of reflection **R5** (see below).

Although it is natural to expect that the NMO velocity $V_{\mathrm{nmo,\,Rb}}$ contains information about the anisotropic parameter ϵ, it turns out not to be the case. The Dix-type averaging equation for tilted layers described by Grechka and Tsvankin (2002a) leads to the following expression for $V_{\mathrm{nmo,\,Rb}}$:

$$V^2_{\mathrm{nmo,\,Rb}} = \frac{\tau_{\mathrm{R4}}\, V^2_{\mathrm{iso}} + (\tau_{\mathrm{Rb}} - \tau_{\mathrm{R4}})\, V^2_{\mathrm{nmo}}}{\tau_{\mathrm{Rb}}\, \cos^2\phi}\,, \tag{5.2.8}$$

where ϕ is the dip of interfaces $[B_2B_3]$ and $[C_3C_4]$, given by equation (5.2.6). Equation (5.2.8) shows that $V_{\mathrm{nmo,\,Rb}}$ depends on a single parameter of the TTI block – the NMO velocity V_{nmo}, which has already been determined from the horizontal events. The same conclusion holds for the almost invisible reflection from segment $[C_4C_5]$.

5.2.8 Reflection R5

Both the thickness $z_\perp$ and the anisotropic coefficient ϵ can be found from traveltime $\tau_{\mathrm{R5}} = 1.378 \pm 0.004$ s and the NMO velocity $V_{\mathrm{nmo,\,R5}} = 3250 \pm 50$ m/s of reflection **R5** (Figures 5.4d and 5.7). Note than neither τ_{R5} nor $V_{\mathrm{nmo,\,R5}}$ depends on the CMP coordinate (Figure 5.2). This is possible only if segments $[B_2B_3]$ and $[C_3C_4]$ are parallel to each other (this has already been established by the analysis of events **R4** and **Rb**) and the bottom interface $[C_3D_1]$ is horizontal. Consequently, the zero-offset ray **R5** inside the isotropic blocks 4 and 6 has to be vertical (Figures 5.3 and 5.7). The zero-offset traveltime τ_{R5} of event **R5** can be written as

$$\tau_{\mathrm{R5}} = \tau_{\mathrm{tti,\,R5}} + \tau_{\mathrm{iso,\,R5}}\,, \tag{5.2.9}$$

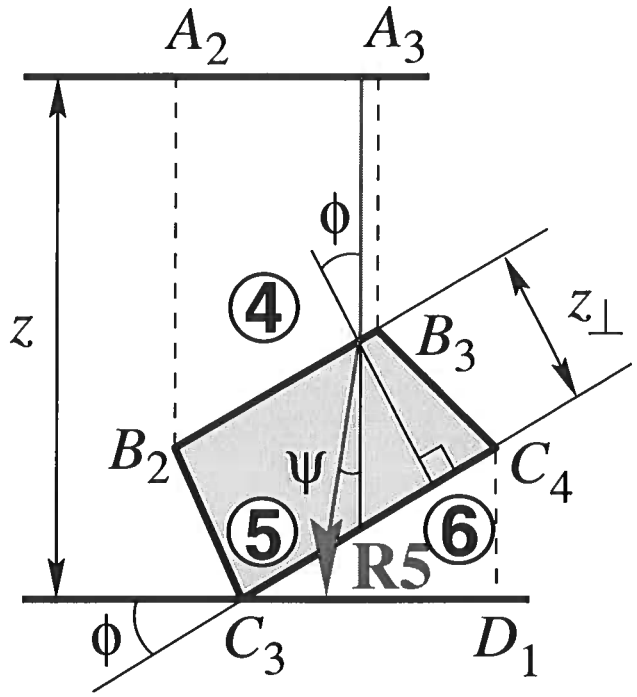

FIG. 5.7. Notation associated with the zero-offset ray of reflection **R5** from the horizontal interface $[C_3D_1]$ below the TTI block 5.

where $\tau_{\mathrm{tti,\,R5}}$ and $\tau_{\mathrm{iso,\,R5}}$ are the traveltimes inside the TTI and isotropic blocks, respectively. Using the relationships between the group(ray)-velocity vector and the horizontal (p) and vertical [$q = q(p)$] components of the slowness vector in the TTI block 5 (Grechka et al., 1999b), one obtains

$$\tau_{\mathrm{tti,\,R5}} = 2\,z_\perp\,(q - p\,q')\,\frac{\cos\psi}{\cos(\phi+\psi)}\,, \tag{5.2.10}$$

$$\tau_{\mathrm{iso,\,R5}} = \frac{2}{V_{\mathrm{iso}}}\left(z - z_\perp\,\frac{\cos\psi}{\cos(\phi+\psi)}\right)\,, \tag{5.2.11}$$

where

$$\psi = \tan^{-1}\left(\frac{dq}{dp}\right) \equiv \tan^{-1} q' \tag{5.2.12}$$

	Actual	Inverted
V_{iso} (m/s)	2740	2742 ± 30
V_0 (m/s)	2925	2963 ± 157
ϵ	0.16	0.16 ± 0.06
δ	0.08	0.09 ± 0.06

Table 2. Comparison of the actual and inverted values of the velocities and anisotropic coefficients.

is the angle between the zero-offset ray and vertical inside the TTI block 5 (Figure 5.7). The slownesses p and q satisfy Snell's law at the top and bottom interfaces of block 5:

$$p = \left(q - \frac{1}{V_{\text{iso}}}\right) \tan\phi \,. \tag{5.2.13}$$

In combination with the Christoffel equation in the TTI layer, Snell's law (5.2.13) can be used to obtain both slowness components for a given set of the TTI parameters.

The NMO velocity $V_{\text{nmo,R5}}$ provides a second equation for estimating $z_\perp$ and ϵ. We omit the derivation of $V_{\text{nmo,R5}}$, which can be found in a straightforward manner using the results of Grechka and Tsvankin (2002a) and Le Stunff et al. (2001):

$$V^2_{\text{nmo,R5}} = \frac{1}{\tau_{\text{R5}}} \left[\tau_{\text{iso,R5}} V^2_{\text{iso}} + \tau_{\text{tti,R5}} \left(\frac{V_{\text{tti,nmo}}(p)}{1 - q' \tan\phi} \right)^2 \right], \tag{5.2.14}$$

where

$$V^2_{\text{tti,nmo}}(p) = \frac{d^2q/dp^2}{p\,q' - q} \tag{5.2.15}$$

is the interval NMO velocity within the TTI block evaluated for the horizontal slowness component p of the zero-offset ray (Grechka et al., 1999b).

After picking τ_{R5} and $V_{nmo,R5}$ from the semblance panel in Figure 5.4d, we perform nonlinear inversion of equations (5.2.9) and (5.2.14) for $z_\perp$ and ϵ and obtain $z_\perp = 594 \pm 105$ m and $\epsilon = 0.16 \pm 0.06$. Complete results of the parameter-estimation procedure are summarized in Table 2.

5.3 Summary

The presence of transverse isotropy with a tilted symmetry axis (TTI media) causes significant distortions in the results of conventional velocity analysis and imaging in overthrust areas. While migration algorithms can be extended to TTI models in a relatively straightforward way, estimating the anisotropic parameters needed to build the velocity model is a much more difficult task. The structural setting of overthrust areas is characterized by steep interfaces and substantial lateral heterogeneity, which further complicate the recovery of the anisotropic velocity field from surface reflection data.

Still, for models consisting of quasi-homogeneous blocks it may be possible to invert P-wave reflection traveltimes acquired in the dip direction of the structure for all relevant parameters of TTI media. Here, we used the physical-modeling data of Leslie and Lawton (1996) to estimate the thickness, symmetry-direction velocity V_0, and the anisotropic coefficients ϵ and δ of a bending transversely isotropic layer. Two important constraints on the TTI model were provided by the geologically justified assumptions that the symmetry axis is orthogonal to the bedding and the TTI layer is homogeneous. Another, more arbitrary assumption used in the inversion procedure was that the bottom of the model is horizontal. This assumption, however, would have been unnecessary if the acquisition geometry had been suitable for processing

reflections from steep interfaces in the shallow portion of the model.

While estimation of the symmetry-direction velocity V_0 and the coefficient δ using horizontal reflection events and the depth of the bottom interface was relatively straightforward, obtaining the parameter ϵ represented the most challenging part of the inversion procedure. As follows from the analytic description of normal moveout in laterally heterogeneous media (Grechka and Tsvankin, 2002a), information about ϵ is contained only in the NMO velocity and zero-offset traveltime of arrivals that cross the dipping TTI blocks and reflect from the bottom of the model. The inversion using one of these reflection events makes it possible to estimate not only the value of ϵ, but also the thickness of the dipping TTI block. Thus, P-wave reflection traveltimes proved to be sufficient to reconstruct the tilted TI model in the depth domain.

In general, the feasibility of anisotropic parameter estimation in TTI media depends strongly on the degree of structural complexity and the range of propagation directions covered by the zero-offset reflected rays. As long as the lateral variation in the elastic parameters is not substantial, the presence of bending TTI layers with variable dips may actually help in parameter estimation by generating reflected rays that cross the TTI blocks at different angles with the symmetry axis. The analytic inversion methods (i.e. those based on NMO ellipses) may become inaccurate for media with more severe lateral heterogeneity, but they can still be used to build an initial model for migration velocity analysis.

One of the objectives was to estimate the confidence intervals for all inverted quantities. These error bars were obtained by visually inspecting the spatial extent of the semblance maxima used to pick the NMO velocities and zero-offset traveltimes. Although this approach is subjective, it still provides useful information about the un-

certainties in the traveltime inversion for anisotropic media. It should be mentioned that the accuracy in velocity picking can be substantially increased by upgrading the acquisition geometry (i.e., recording small offsets, reducing the receiver spacing, etc.).

Chapter 6

STACKING VELOCITY TOMOGRAPHY FOR ORTHORHOMBIC MEDIA

Here, we extend the methodology of stacking-velocity tomography to orthorhombic media, believed to be typical for naturally fractured oil and gas reservoirs (Schoenberg and Helbig, 1997; Bakulin et al., 2000).

6.1 Tomographic parameter estimation using multicomponent data

The success of the parameter-estimation procedure discussed below depends on our ability to construct SS traveltimes from PP and PS reflection data using the $PP + PS = SS$ method (Grechka and Tsvankin, 2002b). Although this method requires no explicit velocity information, one must be able to identify traveltimes of PP- and PS-reflections, from the same interface, on prestack common-receiver gathers. Traveltime picking, however, is difficult for traces with low PS amplitudes (and, correspondingly, low signal-to-noise ratio) caused by small reflection coefficients in areas of polarity reversals. To evaluate the seriousness of this issue for a typical moderately anisotropic orthorhombic model, we use a synthetic test.

We computed the multicomponent seismograms in Figure 6.1 by anisotropic dynamic ray tracing. As expected, the PP reflection has the highest amplitude on the vertical

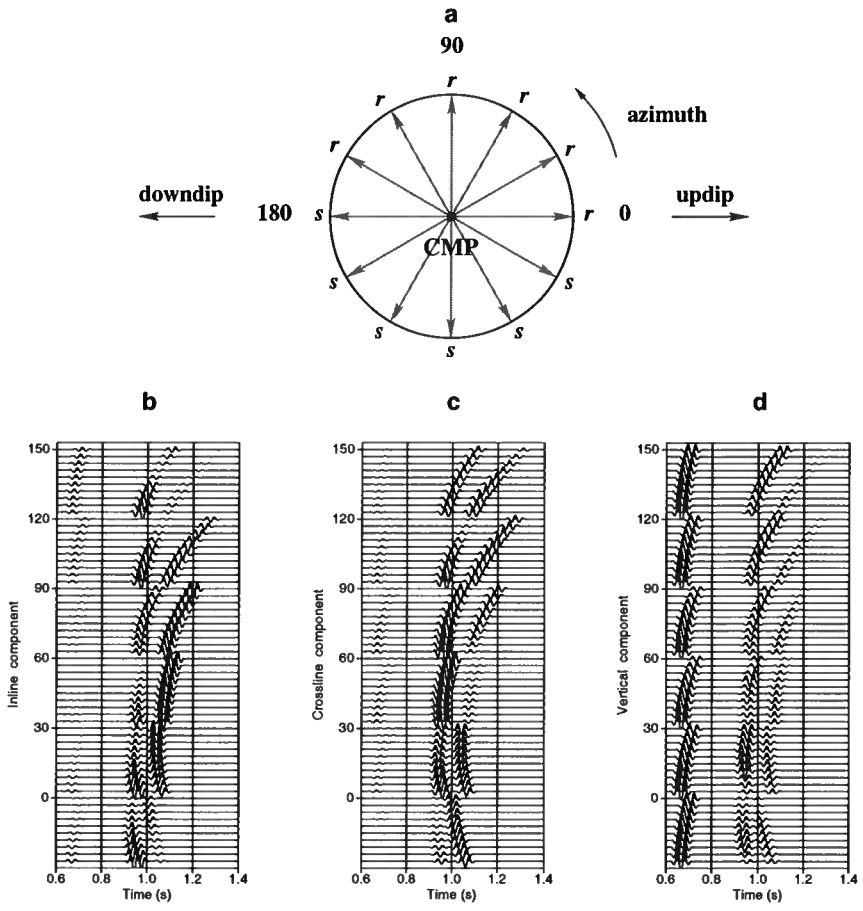

FIG. 6.1. (a) Plan view of a multiazimuth CMP gather, with sources for each line located on one side marked by s, and receivers on the side marked by r. (b-d) True-amplitude three-component synthetic seismograms of PP-, PS_1- and PS_2-waves reflected from a dipping interface beneath an orthorhombic layer. The numbers 0, 30, 60, 90, 120, and 150 on the vertical axis in Figures (b-d) indicate the azimuth (in degrees) of the block of traces plotted under this number (e.g., all traces between numbers 150 and 120 have an azimuth of 150°). The source-receiver offsets within each block of traces range from 0.1 km to 1 km in 0.1 km increments. The azimuth of the dip plane is $\psi = 0°$ (see the plan view), the dip $\phi = 30°$, and the depth under the common midpoint $z = 1$ km. The azimuth of the vertical $[x_1, x_3]$ symmetry plane of the orthorhombic layer with respect to the reflector dip plane is $\beta = 60°$. Tsvankin's (1997c) anisotropic parameters of the layer are $V_{P0} = 2.9$ km/s, $V_{S0} = 1.4$ km/s, $\epsilon^{(2)} = 0.15$, $\delta^{(2)} = 0.05$, $\gamma^{(2)} = -0.25$, $\epsilon^{(1)} = 0.25$, $\delta^{(1)} = 0.15$, $\gamma^{(1)} = -0.20$, $\delta^{(3)} = -0.05$.

component (Figure 6.1d), whereas the two split converted waves PS_1 and PS_2 are seen best on the horizontal inline and crossline components (Figures 6.1b, c). Despite some dimming of the PS_1- and PS_2-waves at certain azimuths, the offset range of those low-amplitude arrivals is relatively narrow. Therefore, Figures 6.1b, c suggest that, despite the presence of polarity reversals, picking of wide-azimuth converted-wave traveltimes over orthorhombic media is feasible. This conclusion remains valid for media with a smaller shear-wave splitting coefficient than those used here, where the PS_1 and PS_2 arrivals overlap, and time picking has to be preceded by Alford (1986) rotation.

Once the traveltimes of PP-, PS_1-, and PS_2-waves have been picked, the $PP + PS = SS$ method can be employed to compute the traveltimes t_{S1} and t_{S2} of pure shear-wave reflections S_1S_1 and S_2S_2 from the same interface. The traveltimes t_{S1} and t_{S2} are guaranteed to be symmetric with respect to the common midpoint, so they can be processed by means of hyperbolic semblance analysis. For wide-azimuth data, it is possible to reconstruct the NMO ellipses of both PP- and SS-waves using a 3-D hyperbolic semblance operator (Grechka and Tsvankin, 1999b).

The NMO ellipses, along with the corresponding horizontal projections of the slowness vectors $\boldsymbol{p}_Q$ (the reflection slopes on zero-offset time sections) and zero-offset traveltimes τ_Q ($Q = P$, S_1, or S_2), are used as the input data for anisotropic stacking-velocity tomography. The data vector for an N-layered orthorhombic medium is

$$\boldsymbol{d}(Q, \boldsymbol{Y}, n) \equiv \{\tau_Q(\boldsymbol{Y}, n), \boldsymbol{p}_Q(\boldsymbol{Y}, n), \boldsymbol{W}_Q(\boldsymbol{Y}, n)\}\,, \tag{6.1.1}$$

where $\boldsymbol{Y} = [Y_1, Y_2]$ is the CMP location, $n = 1, 2, ..., N$ is the reflector number and $\boldsymbol{W}$ is the 2×2 matrix describing the NMO ellipse.

Stacking-velocity tomography for multicomponent data is described in detail in Chapter 4 (Grechka et al., 2002b).

In the next section, we discuss the issues of uniqueness and stability in the inversion of the data vector (6.1.1) for the parameters of orthorhombic media.

6.2 Parameter estimation in a single orthorhombic layer

First, we review notation and some relevant properties of wave propagation for orthorhombic models. Seismic signatures in orthorhombic media can be conveniently described in terms of the two vertical velocities,

$$V_{P0}=\sqrt{\frac{c_{33}}{\rho}} \quad \text{and} \quad V_{S0}=\sqrt{\frac{c_{55}}{\rho}}, \tag{6.2.2}$$

and Thomsen-style anisotropic coefficients $\epsilon^{(1,2)}$, $\delta^{(1,2,3)}$, and $\gamma^{(1,2)}$ introduced by Tsvankin (1997c); c_{ij} are the components of the stiffness tensor and ρ is the density. The coefficients $\epsilon^{(i)}$, $\delta^{(i)}$, $\gamma^{(i)}$ $(i=1,2)$ defined in the vertical symmetry planes $[x_2, x_3]$ and $[x_1, x_3]$ (Figure 6.2) have the same meaning as Thomsen's (1986) parameters ϵ, δ, and γ for transverse isotropy. The coefficient $\delta^{(3)}$ plays the role of Thomsen's δ in the horizontal plane $[x_1, x_2]$.

The kinematics of wave propagation in the symmetry planes of orthorhombic media is practically identical to that in VTI media. The only notable difference is caused by the so-called singularity directions in orthorhombic media (the point A in Figure 6.2), where the phase velocities of two shear waves coincide. The S_2-wavefront near a singularity usually becomes multi-valued, while the wavefront of the fast S_1-wave develops an elliptical hole. Those complicated phenomena are outside of the scope of

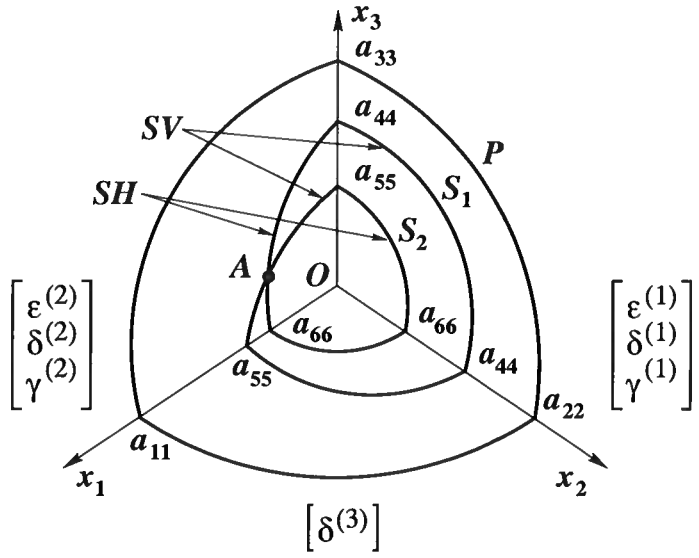

FIG. 6.2. Sketch of body-wave phase-velocity surfaces in orthorhombic media (after Grechka et al., 1999a). The coefficients $\epsilon^{(1)}$, $\delta^{(1)}$ and $\gamma^{(1)}$ are defined in the symmetry plane $[x_2, x_3]$, while $\epsilon^{(2)}$, $\delta^{(2)}$ and $\gamma^{(2)}$ correspond to the plane $[x_1, x_3]$ (Tsvankin, 1997c). $a_{ij} \equiv \sqrt{c_{ij}/\rho}$, where c_{ij} are the stiffness coefficients and ρ is the density.

the thesis; hereafter, we assume that the singularities are located outside of the fan of ray directions used for velocity analysis.

6.2.1 Horizontal reflector

The semi-axes of NMO ellipses for all reflection modes in a horizontal orthorhombic layer are co-oriented with the vertical symmetry planes and have the following simple form (Grechka et al, 1999a):

$$\frac{1}{V^2_{Q,\mathrm{nmo}}(\alpha)} = \frac{\cos^2\alpha}{\left[V^{(2)}_{Q,\mathrm{nmo}}\right]^2} + \frac{\sin^2\alpha}{\left[V^{(1)}_{Q,\mathrm{nmo}}\right]^2} \tag{6.2.3}$$

$(Q = P,\ S_1,\ \text{or}\ S_2)$;

α is the azimuth with respect to the $[x_1, x_3]$-plane. Because of the kinematic equivalence between the symmetry planes of orthorhombic and VTI media, the semi-axes of the NMO ellipses ($V^{(i)}_{Q,\mathrm{nmo}}$) can be obtained by adapting the VTI equations (Grechka and Tsvankin, 1998b)

$$V^{(2)}_{P,\mathrm{nmo}} = V_{P0}\sqrt{1+2\,\delta^{(2)}}\,, \tag{6.2.4}$$

$$V^{(1)}_{P,\mathrm{nmo}} = V_{P0}\sqrt{1+2\,\delta^{(1)}}\,, \tag{6.2.5}$$

$$V^{(2)}_{S1,\mathrm{nmo}} = V_{S1}\sqrt{1+2\,\gamma^{(2)}} = \sqrt{c_{66}/\rho}\,, \tag{6.2.6}$$

$$V^{(1)}_{S1,\mathrm{nmo}} = V_{S1}\sqrt{1+2\,\sigma^{(1)}}\,, \tag{6.2.7}$$

$$V^{(2)}_{S2,\mathrm{nmo}} = V_{S2}\sqrt{1+2\,\sigma^{(2)}}\,, \tag{6.2.8}$$

$$V^{(1)}_{S2,\mathrm{nmo}} = V_{S2}\sqrt{1+2\,\gamma^{(1)}} = \sqrt{c_{66}/\rho}\,, \tag{6.2.9}$$

where

$$\sigma^{(2)} = \left(\frac{V_{P0}}{V_{S2}}\right)^2 \left(\epsilon^{(2)} - \delta^{(2)}\right)\,,$$

$$\sigma^{(1)} = \left(\frac{V_{P0}}{V_{S1}}\right)^2 \left(\epsilon^{(1)} - \delta^{(1)}\right)\,, \tag{6.2.10}$$

and

$$V_{S2} = V_{S0}\,, \qquad V_{S1} = V_{S0}\sqrt{\frac{1+2\,\gamma^{(1)}}{1+2\,\gamma^{(2)}}}\,. \tag{6.2.11}$$

Here, it is assumed that the fast mode S_1 at vertical incidence is polarized in the x_2-direction.

As follows from equations (6.2.4)–(6.2.11), the anisotropic coefficients $\epsilon^{(1,2)}$, $\delta^{(1,2)}$, and $\gamma^{(1,2)}$ can be estimated in a unique fashion only if either one of the vertical velocities or the reflector depth is known. This result is hardly surprising because the NMO velocities and zero-offset traveltimes could not be unambiguously inverted for the anisotropic parameters even for the higher-symmetry horizontal VTI layer.

Note that the coefficient $\delta^{(3)}$ has no influence on the NMO ellipses in a horizontal layer and, therefore, cannot be determined from conventional-spread reflection moveout. A more detailed discussion of the NMO ellipses of pure and converted waves in horizontally layered orthorhombic media, and their inversion, can be found in Grechka et al. (1999a).

6.2.2 Plane dipping reflector co-oriented with a vertical symmetry plane

While moveout inversion of multicomponent data is nonunique for a horizontal VTI layer, the results of Chapter 4 show that the vertical velocities and coefficients ϵ and δ can be estimated uniquely from PP and SS traveltimes if the reflector beneath the VTI medium has a dip of at least 15-20°. Here, let us examine whether or not this result holds for an orthorhombic layer above a plane dipping reflector that is oriented in such a way that the dip plane coincides with one of the vertical symmetry planes of the overburden.

Suppose the dip plane of the reflector is the $[x_1, x_3]$ symmetry plane of the orthorhombic medium. Since the slowness vector of the zero-offset ray for any pure mode is or-

thogonal to the reflector, the horizontal slowness projection at zero offset is confined to the dip plane. Both horizontal slowness components (p_1 and p_2) of the zero-offset ray can be found from reflection slopes on the zero-offset (or stacked) time section. Therefore, reflection time slopes can be used to find the azimuthal direction of both the reflector and the $[x_1, x_3]$ symmetry plane.

Then, the model vector $\boldsymbol{m}$ to be estimated from moveout data contains the remaining eleven unknowns: nine Tsvankin's (1997c) parameters discussed above (V_{P0}, V_{S0}, $\epsilon^{(1)}$, $\epsilon^{(2)}$, $\delta^{(1)}$, $\delta^{(2)}$, $\delta^{(3)}$, $\gamma^{(1)}$, and $\gamma^{(2)}$), the reflector dip ϕ, and the distance D between the reflector and the origin of the Cartesian coordinate system $\boldsymbol{O}$. The elements of $\boldsymbol{m}$ are supposed to be found from the eighteen-component data vector (6.1.1), which has six zero elements,

$$p_{2,Q} = 0;\ W_{12,Q} = 0, \quad (Q = P,\ S_1,\ \text{or}\ S_2)\,, \tag{6.2.12}$$

because $[x_1, x_3]$ is the symmetry plane for the whole model. The remaining three zero-offset traveltimes τ_Q, three horizontal slownesses $p_{1,Q}$, and six diagonal elements of the matrices $\boldsymbol{W}_Q$ (which correspond to the dip- and strike-components of the NMO velocities) provide a total of 12 equations.

However, below we demonstrate that the expressions for the traveltimes τ_Q are not independent. The equation of a planar reflector can be written as

$$\boldsymbol{n} \cdot \boldsymbol{x} = D\,, \tag{6.2.13}$$

where $\boldsymbol{n} \equiv [\sin\phi,\ 0,\ \cos\phi\,]$ is a unit vector perpendicular to the reflector. Assuming that the origin $\boldsymbol{O}$ of the Cartesian coordinate system is placed at the common midpoint, the reflection point $\boldsymbol{r}_Q$ of the zero-offset ray can be found from

$$\boldsymbol{r}_Q = \boldsymbol{g}_Q \tau_Q \,, \tag{6.2.14}$$

where $\boldsymbol{g}_Q$ is the group-velocity vector of mode Q. Since the point $\boldsymbol{r}_Q$ lies on the reflector (6.2.13), the one-way zero-offset traveltime is

$$\tau_Q = \frac{D}{\boldsymbol{n} \cdot \boldsymbol{g}_Q} \,. \tag{6.2.15}$$

Snell's law requires that the slowness vectors $\boldsymbol{p}_Q \equiv [p_{1,Q},\, 0,\, p_{3,Q}]$ of pure modes be parallel to each other and orthogonal to the reflector, so

$$\boldsymbol{n} = \frac{\boldsymbol{p}_Q}{|\boldsymbol{p}_Q|} \qquad (Q = P,\ S_1,\ \text{or}\ S_2) \,. \tag{6.2.16}$$

Combining equations (6.2.15) and (6.2.16) and taking into account that $\boldsymbol{p}_Q \cdot \boldsymbol{g}_Q = 1$ (this equality plays the role of the eikonal equation in anisotropic media) yields

$$\tau_Q = \frac{D\,|\boldsymbol{p}_Q|}{\boldsymbol{p}_Q \cdot \boldsymbol{g}_Q} = D\,|\boldsymbol{p}_Q| = \frac{D\,p_{1,Q}}{\sin\phi} \,. \tag{6.2.17}$$

Equation (6.2.17) shows that three zero-offset traveltimes τ_P, τ_{S1}, and τ_{S2} constrain only *one* combination of the model parameters – $D/\sin\phi$. Therefore, the number of independent equations to be solved for the 11 unknown parameters reduces from 12 to 10. Clearly, this inverse problem does not have a unique solution.

6.2.3 Arbitrarily oriented plane dipping reflector

If the dip plane of the reflector does not coincide with either vertical symmetry plane, each NMO ellipse generally has a different orientation. That increases the number of

independent components of the data vector (6.1.1) and, as demonstrated below, can make the inversion unambiguous.

Indeed, if the dip plane and the symmetry planes are misaligned, the number of equations exceeds the number of unknowns. The model vector includes 13 elements to be found from the data:

$$\boldsymbol{m} = \{V_{P0},\, V_{S0},\, \epsilon^{(1)},\, \delta^{(1)},\, \gamma^{(1)},\, \epsilon^{(2)},\, \delta^{(2)},\, \gamma^{(2)},\, \delta^{(3)},\, \beta,\, D,\, \phi,\, \psi\}\,, \tag{6.2.18}$$

where β is the azimuth of the vertical symmetry plane $[x_1,\, x_3]$ and ψ is the azimuth of the dip plane of the reflector. The original number of equations (i.e., the number of measured quantities) is 18 [equation (6.1.1)], but, as discussed above [see equation (6.2.17)], the three traveltimes τ_Q provide only one independent equation. In addition, the ratio of the horizontal slowness components for each mode is fixed by the reflector azimuth ($p_{2,Q}/p_{1,Q} = \tan\psi$), which eliminates two more independent equations. Even with these factors taken into account, however, the number of equations (14) is larger than the number of unknown model parameters (13), and, in principle, the moveout inversion may be possible.

Still, the inverse problem is nonlinear, so the feasibility of parameter estimation has to be assessed by numerical testing on noise-contaminated data. The numerical analysis will show that the inversion for a range of typical orthorhombic models is not only unique but also quite stable. Because of the multimodal nature of the misfit function, we perform several inversions starting from different points in the model space. The results in Figure 6.3 are obtained from the data $\boldsymbol{d} = \left\{\tau_Q,\, \boldsymbol{p}_Q,\, \boldsymbol{W}_Q\right\}$ generated for all three modes (P, S_1 and S_2) at a single CMP location. The traveltimes τ_Q, the horizontal slowness components $\boldsymbol{p}_Q$, and the NMO ellipses $\boldsymbol{W}_Q$ were contaminated

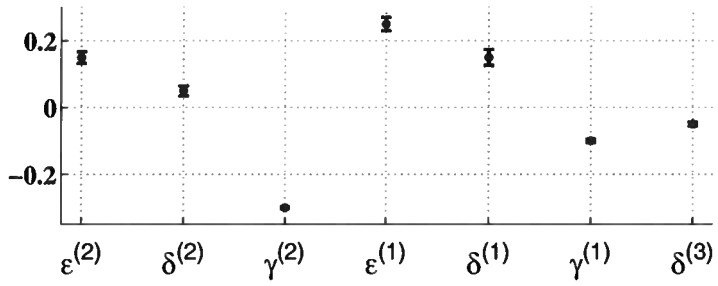

FIG. 6.3. Inversion results for a single orthorhombic layer above a dipping reflector. The exact values of the anisotropic coefficients are marked by the dots; the bars correspond to the ± standard deviation in each parameter. The reflector dip ϕ is 30°, the azimuth of the dip plane $\psi = 0°$, and the azimuth of the $[x_1, x_3]$ symmetry plane of the layer $\beta = 60°$.

by Gaussian noise with standard deviations of 1% for τ_Q and $\boldsymbol{p}_Q$ and 2% for $\boldsymbol{W}_Q$.

The parameter estimation was repeated 100 times for different realizations of the noise using a nonlinear least-squares algorithm. The maximum standard deviation in the recovered anisotropic coefficients does not exceed 0.025 (the value for $\delta^{(1)}$ in Figure 6.3), which means that the inversion is sufficiently stable. The standard deviations for the parameters not displayed in Figure 6.3 are small as well (1.2% and 0.6% for the vertical velocities V_{P0} and V_{S0}, respectively, and less than 1° for the angles β, ϕ and ψ).

For the model from Figure 6.3, the dip plane of the reflector deviates by 30° from the nearest vertical symmetry plane, which ensures the high stability of the inversion result. Figure 6.4 shows the inversion output for a model similar to that in Figure 6.3, but the azimuth angle between the dip plane and a vertical symmetry plane is just 15°, and the dip ϕ is reduced from 30° to 20°. Both changes have a negative influence on the performance of the inversion algorithm, and the error bars for most parameters become noticeably longer. Still, the moderate magnitude of the standard deviations

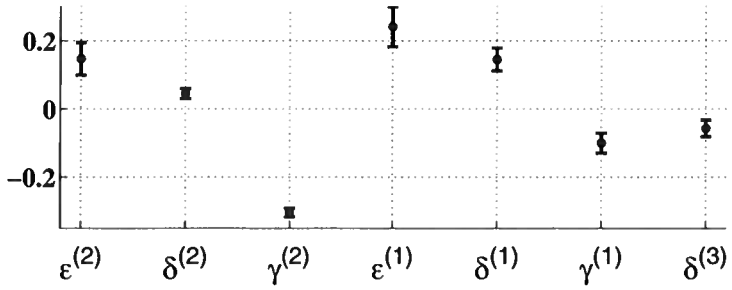

FIG. 6.4. Same as Figure 6.3, but the reflector dip ϕ is 20°, and the azimuth of the $[x_1, x_3]$ symmetry plane $\beta = 15°$ (the azimuth of the dip plane remains $\psi = 0°$). The standard deviations for the parameters not shown on the plot are as follows: 1.3% and 0.7% for the velocities V_{P0} and V_{S0}, respectively, and less than 1.5° for the angles β, ϕ and ψ.

indicates that the inversion remains sufficiently stable for practical applications.

Further reduction in the difference $|\psi - \beta|$ or in the reflector dip leads to a rapid increase in the errors (i.e., the standard deviations). Indeed, the analysis in the previous section suggests that the inversion becomes nonunique when $|\psi - \beta|$ approaches $k\pi/2$, where k is an integer. Likewise, the inversion becomes unstable if the reflector dip $\phi < 15°$; for subhorizontal reflectors the anisotropic coefficients cannot be estimated without *a priori* knowledge of the vertical velocities or reflector depth (see above). A similar dependence of the quality of moveout-inversion results on reflector dip was found for VTI media in Chapter 4 (see also Tsvankin and Grechka, 2000, 2002).

6.2.4 Curved reflector

If the reflector beneath an orthorhombic layer has arbitrary spatially varying curvature, the uniqueness of the inversion procedure is much more difficult to evaluate analytically. The feasibility of estimating the medium parameters in this case strongly

depends on the shape and parameterization of the reflector and the spatial distribution of the common midpoints (see Chapter 4).

Extensive testing with synthetic traveltimes shows that reflector curvature does not pose any serious problems for the parameter estimation in a single orthorhombic layer, provided the reflecting interface contains dips over 15° and the dip directions deviate from the vertical symmetry planes. Typical inversion results for noise-contaminated data τ_Q, $\boldsymbol{p}_Q$, and $\boldsymbol{W}_Q$ from nine CMP locations are displayed in Figure 6.5. As in the previous test, the inversion was repeated 100 times to study the distribution of the estimated parameters. The standard deviations in Figure 6.5b are even smaller than those in Figure 6.3; this conclusion also holds for the vertical velocities V_{P0}, V_{S0} and the reflector orientation (not shown).

The increase in stability for the curved reflector in Figure 6.5 is explained by the relatively wide range of reflector dips and azimuths sampled by the zero-offset rays. In other words, each CMP provides independent information. This advantage of curved interfaces, of course, can be fully exploited only if it is still possible to treat the medium above the reflector as homogeneous.

6.3 Stacking-velocity tomography in layered media

The above analysis for a single orthorhombic layer helped to reveal the potential of the multicomponent inversion algorithm. In this section, the methodology of stacking-velocity tomography is applied to more realistic models composed of homogeneous orthorhombic layers separated by plane or curved interfaces.

If *noise-free* data $\left\{\tau_Q, \boldsymbol{p}_Q, \boldsymbol{W}_Q\right\}$ $(Q = P, S_1, S_2)$ for all interfaces are available, and

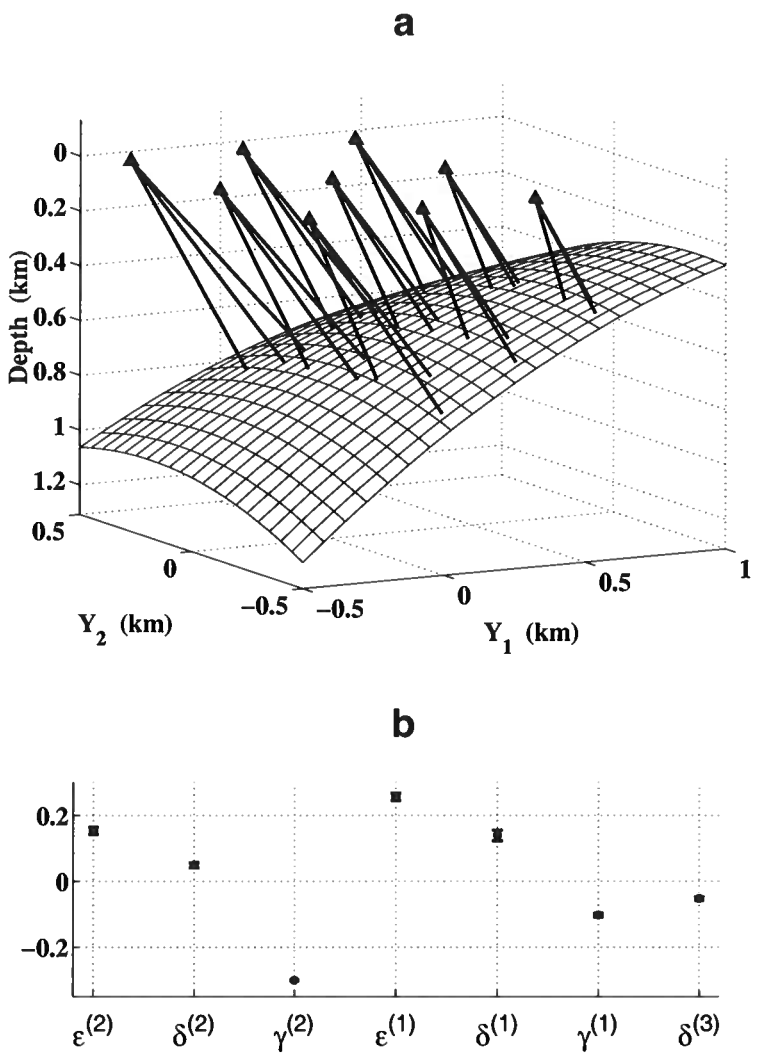

FIG. 6.5. (a) Zero-offset rays of the P- S_1- and S_2-waves reflected from a curved interface below an orthorhombic layer and (b) the estimated anisotropic parameters. The $[x_1, x_3]$ symmetry plane makes an angle of 60° with the Y_1-axis. The data were contaminated with Gaussian noise that had the same standard deviations as in Figure 6.3. The exact values of the anisotropic coefficients are marked by the dots, while the bars correspond to the $\pm$ standard deviation in each parameter.

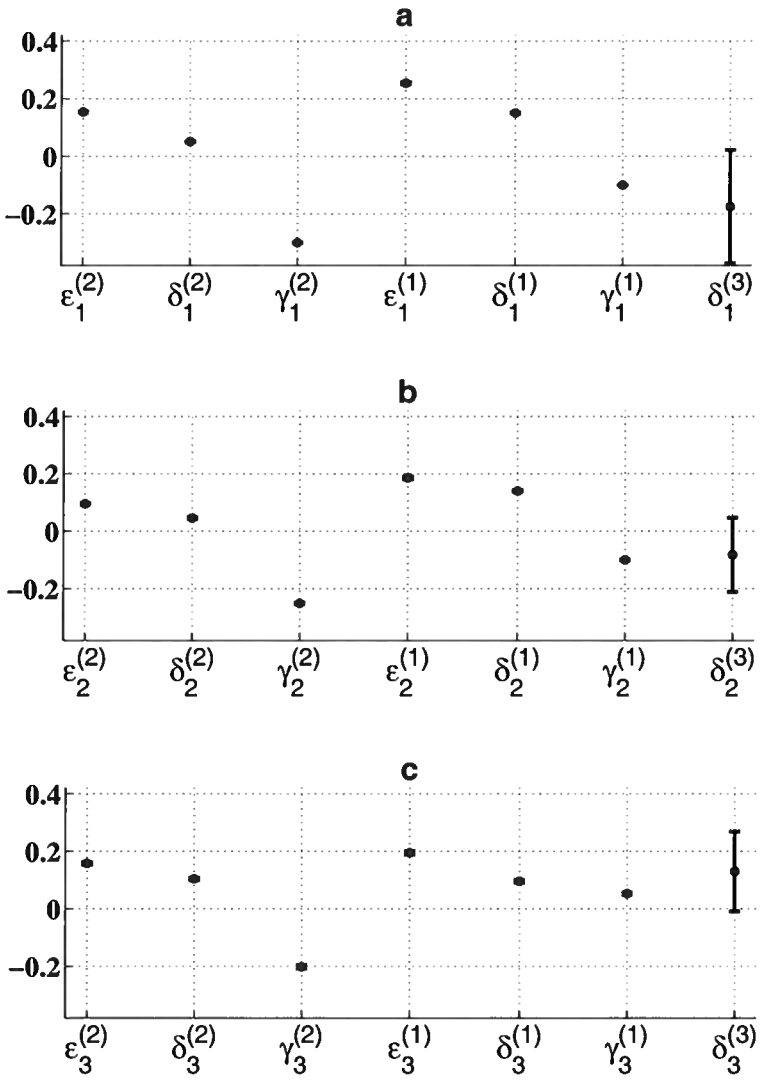

FIG. 6.6. The results of stacking-velocity tomography for a model composed of three horizontal layers (a – top layer, b – middle layer, c – bottom layer) with different azimuths of the vertical symmetry planes. The vertical velocities were assumed to be known; from top to bottom, $V_{P0,1} = 1.0$ km/s, $V_{S0,1} = 0.5$ km/s, $V_{P0,2} = 1.5$ km/s, $V_{S0,2} = 0.6$ km/s, and $V_{P0,3} = 1.8$ km/s, $V_{S0,3} = 1.0$ km/s. The layer thicknesses are $z_1 = 0.4$ km, $z_2 = 0.6$ km and $z_3 = 0.8$ km, and the azimuths of the symmetry planes are $\beta_1 = 40°$, $\beta_2 = 70°$ and $\beta_3 = 10°$.

the reflectors satisfy the conditions established for a single layer (i.e., the dips exceed 15-20° and the reflector azimuths sufficiently deviate from those of the vertical symmetry planes), the tomographic algorithm can recover the interval orthorhombic parameters along with the shapes of the interfaces. However, due to error accumulation with depth and a lower sensitivity of surface data to the parameters of deeper layers, even moderate noise causes substantial errors in the interval parameters.

To make the inversion sufficiently stable for field-data applications, we assume that the interval vertical velocities ($V_{P0,n}$ or $V_{S0,n}$) are known in all layers $n = 1, \ldots, N$. It may be sufficient to establish some constraints on the vertical velocities to recover the rest of the medium parameters; alternatively, it is possible to specify the thickness of each layer. Such an assumption may not be too restrictive in reservoir characterization because seismic inversion for orthorhombic anisotropy would typically be performed at later stages of the reservoir development when borehole and check-shot data are already available.

Figure 6.6 shows the parameter-estimation results for a model composed of three horizontal orthorhombic layers. The data $\left\{\tau_Q, \boldsymbol{p}_Q, \boldsymbol{W}_Q\right\}$ were generated for nine common midpoints and contaminated by Gaussian noise with standard deviations of 1% for the zero-offset traveltimes and horizontal slownesses and 2% for the matrices $\mathbf{W}$ describing the NMO ellipses. After fixing the interval vertical velocities $V_{P0,n}$, $V_{S0,n}$ ($n = 1, 2, 3$) at the correct values, we performed the inversion for the interval anisotropic coefficients, the azimuths β_n of the vertical symmetry planes, and the layer thicknesses. Knowledge of the vertical velocities ensures that all anisotropic coefficients except for $\delta^{(3)}$ are estimated with high accuracy. Because the parameter $\delta^{(3)}$ has no influence on the NMO ellipses of both P- and S-waves in a horizontal orthorhombic layer (see above), it is not constrained by the input data. The stan-

dard deviations in the azimuths of the symmetry planes do not exceed 1°, and the deviations in the layer thicknesses are less than 1%.

Application of the tomographic algorithm to a more complicated layered model with curved interfaces is illustrated by Figure 6.7. The input data were computed again for nine common midpoints (Figure 6.7a) and contaminated by Gaussian noise with the same standard deviations as in Figure 6.6. In addition to the interval anisotropic parameters and the azimuths β_n of the vertical symmetry planes, the algorithm was designed to reconstruct the shapes of all three interfaces. As expected for any technique based on surface traveltime data, parameter estimation becomes less stable with depth (Figures 6.7b,c,d). Nevertheless, the standard deviations in the anisotropic parameters do not exceed 0.1 (the value for $\delta_3^{(1)}$ in Figure 6.7d). Taking into account that the error amplification for a given layer is proportional to its relative thickness, we conclude that the anisotropic coefficients are constrained reasonably well. The azimuths of the symmetry planes and the shapes of the interfaces were also estimated with high accuracy; the standard deviations in β_1, β_2, and β_3 are 1.0°, 1.6°, and 4.6°, respectively.

6.4 Summary

Estimating the parameters of orthorhombic media from surface seismic data is of primary importance in building realistic models of naturally fractured reservoirs. This chapter is devoted to an extension of multicomponent stacking-velocity tomography to orthorhombic media. The input data include the NMO ellipses, zero-offset traveltimes, and reflection slopes of the PP- and SS-waves, which are inverted for the interval anisotropic parameters and the shapes of the interfaces.

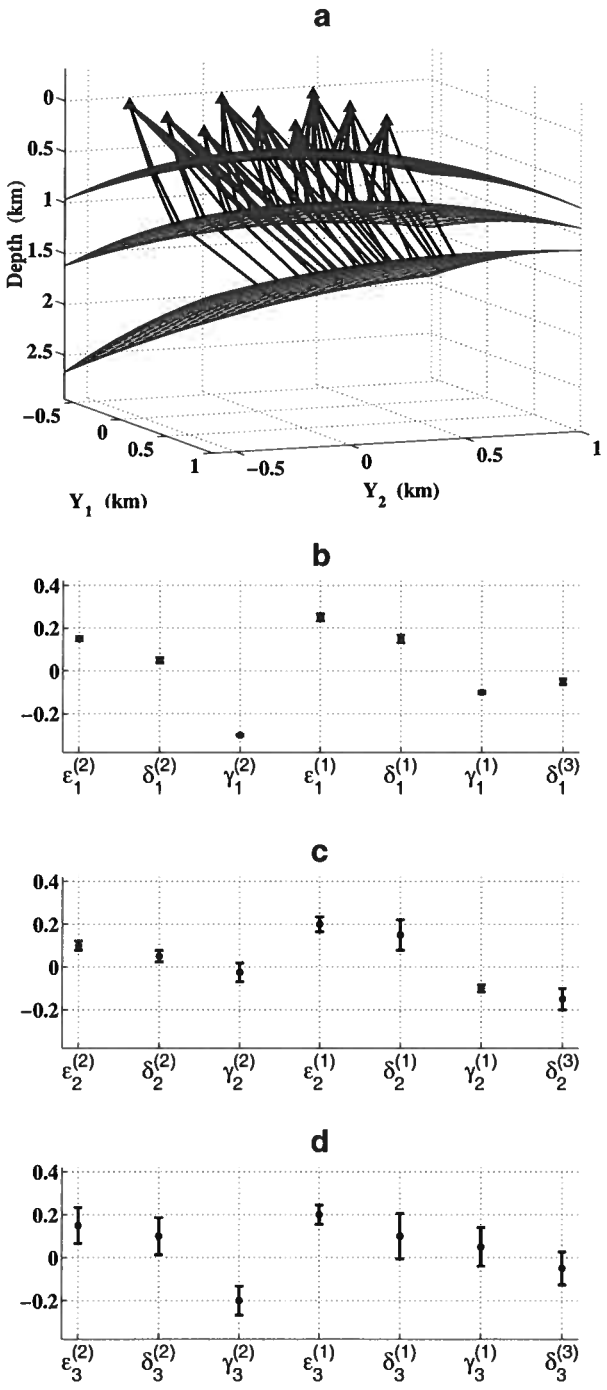

FIG. 6.7. (a) Reflected zero-offset rays of the P-, S_1- and S_2-waves in a three-layer orthorhombic medium, and (b,c,d) the results of stacking-velocity tomography. The vertical velocities $V_{P0,1} = 1.0$ km/s, $V_{S0,1} = 0.6$ km/s, $V_{P0,2} = 1.5$ km/s, $V_{S0,2} = 0.8$ km/s, and $V_{P0,3} = 1.8$ km/s, $V_{S0,3} = 1.0$ km/s were assumed to be known. The azimuths of the symmetry planes are $\beta_1 = 40°$, $\beta_2 = 50°$ and $\beta_3 = 10°$.

The theoretical conditions needed to make this inversion unique for a single orthorhombic layer require that the reflector has at least a mild dip (ϕ) and the azimuth of the dip plane (ψ) be different from those of the vertical symmetry planes of the overburden ($\beta \pm 90°$). If the reflector is horizontal, the vertical velocities and the anisotropic parameters $\epsilon^{(1,2)}$, $\delta^{(1,2,3)}$, and $\gamma^{(1,2)}$ cannot be obtained from the reflection traveltimes of PP- and SS-waves (or PS-waves) alone (Grechka et al., 1999a). Even a mild reflector dip $\phi = 15 - 20°$, however, makes the inversion for a single orthorhombic layer feasible; a similar result was obtained by Tsvankin and Grechka (2000, 2002) for VTI media.

When the dip plane of the reflector coincides with one of the vertical symmetry planes of the overburden, the NMO ellipses are co-oriented with the dip and strike directions and do not contain enough information about the medium parameters. The difference between the dip direction and the azimuth of the nearest symmetry plane has to exceed 10° to ensure unambiguous inversion. The same condition ($|\psi - \beta| > 10°$) is required in the inversion of multiazimuth PP-wave traveltimes for the anellipticity parameters η of orthorhombic media (Grechka and Tsvankin, 1999a).

Synthetic tests on noise-contaminated data for typical orthorhombic models show that, for a single layer, noise does not get amplified by the inversion algorithm. In contrast, the estimated anisotropic parameters in layered orthorhombic media often are significantly distorted as a result of error accumulation with depth and a reduced sensitivity of surface data to the parameters of deeper layers. We suggested that this instability in stacking-velocity tomography could be avoided by supplementing the surface data with constraints on the vertical velocities of the P- and S-waves measured from well logs or check shots. This constraint makes the inversion results sufficiently stable for application in quantitative fracture characterization for

orthorhombic reservoir models (Bakulin et al., 2000).

Chapter 7

ANALYTIC DESCRIPTION OF NONHYPERBOLIC REFLECTION MOVEOUT

7.1 Nonhyperbolic moveout equation

Reflection traveltime of pure (non-converted) modes is conventionally approximated by a Taylor series expansion of the squared traveltime t^2, which is often truncated after the quartic term (Taner and Koehler, 1969):

$$t^2 = A_0 + A_2 X^2 + A_4 X^4 , \tag{7.1.1}$$

where X is the source-receiver offset and

$$A_0 = t_0^2,\ A_2 = \left.\frac{d(t^2)}{d(X^2)}\right|_{X=0},\ A_4 = \frac{1}{2}\frac{d}{d(X^2)}\left[\frac{d(t^2)}{d(X^2)}\right]\Bigg|_{X=0} . \tag{7.1.2}$$

$t_0 = t(0)$ is the two-way zero-offset traveltime, and A_2 is related to the NMO velocity as $A_2 = V_{\mathrm{nmo}}^{-2}$. The first two terms in equation (7.1.1) describe the hyperbolic part of the moveout curve, while A_4 is the quartic coefficient primarily responsible for nonhyperbolic moveout.

Although the series (7.1.1) provides a better approximation for long-spread moveout than does the conventional hyperbolic equation based on just the NMO velocity, it

loses accuracy for offsets reaching 1.5-2 z (z is the reflector depth). Tsvankin and Thomsen (1994) modified equation (7.1.1) by adding a denominator to the quartic moveout term to make $t(X)$ convergent at $X \to \infty$:

$$t^2 = A_0 + A_2 X^2 + \frac{A_4 X^4}{1 + A X^2}, \tag{7.1.3}$$

where the additional coefficient A depends on the horizontal group velocity V_{hor},

$$A = \frac{A_4}{V_{\text{hor}}^{-2} - V_{\text{nmo}}^{-2}}. \tag{7.1.4}$$

Equation (7.1.3) was originally derived for VTI media, but its generic form makes it suitable for anisotropic media of any symmetry. For example, Al-Dajani and Tsvankin (1998) obtained the exact moveout parameters A_2 (V_{nmo}) and A_4 for a horizontal HTI layer and used them to extend equation (7.1.3) to azimuthally dependent P-wave moveout in HTI media. While equation (7.1.3) is not always adequate for pure (non-converted) S-waves (Tsvankin and Thomsen, 1994), it provides a simple and numerically efficient way for modeling the reflection traveltimes of P-waves and, for relatively simple models, converted waves (Tsvankin, 2001).

For horizontally layered anisotropic media above the reflector, the effective NMO velocity (or the effective A_2) in a certain azimuthal direction can be determined from the generalized Dix formula of Grechka et al. (1999), which operates with interval NMO ellipses (Grechka and Tsvankin, 2002a). The velocity V_{hor} used in equation (7.1.4) to define the coefficient A is found by averaging the interval horizontal velocities (Tsvankin, 2001).

Therefore, the key issue in applying equation (7.1.3) is to derive the corresponding quartic moveout coefficient A_4. The dependence of A_4 on the medium parameters

also yields valuable analytic insight into the properties of nonhyperbolic moveout. Below, we give a general representation of the coefficient A_4 and discuss its behavior for TI media with arbitrary symmetry-axis orientation.

7.2 General expression for the quartic moveout coefficient

Here, we present an exact expression for the quartic moveout coefficient in arbitrarily anisotropic, heterogeneous media (Figure 7.1). The derivation, described in detail in Appendix I, is based on expanding the two-way traveltime in a Taylor series in half-offset and applying the so-called normal-incidence-point (NIP) theorem (Chernjak and Gritsenko, 1979; Hubral and Krey, 1980; Fomel and Grechka, 2001), which helps to relate the Taylor series coefficients to the spatial derivatives of the zero-offset traveltime. The general form of the quartic moveout coefficient A_4 can be represented as (Appendix I):

$$A_4 = \frac{1}{16} \left[\frac{\partial^2 \tau_0}{\partial y_k \, \partial y_l} \frac{\partial^2 \tau_0}{\partial y_m \, \partial y_n} + \frac{\tau_0}{3} \frac{\partial^4 \tau_0}{\partial y_k \, \partial y_l \, \partial y_m \, \partial y_n} - \tau_0 \frac{\partial^3 \tau_0}{\partial y_k \, \partial y_l \, \partial x_i} \left(\frac{\partial^2 \tau_0}{\partial x_i \, \partial x_j} \right)^{-1} \frac{\partial^3 \tau_0}{\partial x_j \, \partial y_m \, \partial y_n} \right] L_k L_l L_m L_n \,, \tag{7.2.5}$$

where $\mathbf{y}$ defines the CMP location, $\mathbf{x}$ defines the reflection point, τ_0 is the one-way zero-offset traveltime, and $\mathbf{L}$ is a unit vector parallel to the CMP line. Since in our case the traveltime is recorded at the surface, $\mathbf{L} = [\cos\alpha, \sin\alpha, 0]$, where α is the azimuth of the CMP line with respect to the axis x_1.

Equation (7.2.5) was obtained without making specific assumptions about the anisotropy or heterogeneity of the model; also, it is generally valid for reflectors of irregular shape.

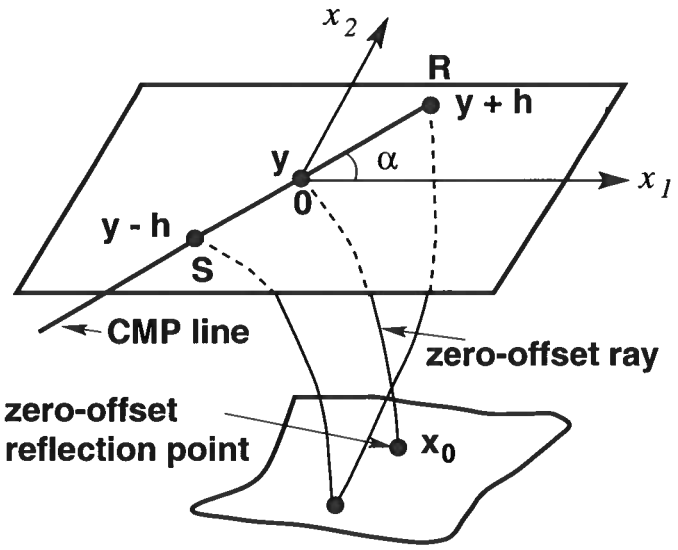

FIG. 7.1. Reflection traveltimes from an irregular interface are recorded in a multi-azimuth CMP gather over an arbitrarily anisotropic, heterogeneous medium. The quartic moveout coefficient A_4 varies with the azimuth α of the CMP line. **h** is the half-offset vector. The derivation of the quartic coefficient in Appendix I takes into account reflection-point dispersal.

Our derivation, however, assume that the one-way zero-offset traveltime can be differentiated with respect to the spatial coordinates near the common midpoint, which is not the case, for example, in shadow zones. The Taylor series expansion for reflection traveltime may break down for models with strong lateral velocity variations (Grechka and Tsvankin, 1998b) and in the vicinity of caustics. Nonetheless, for sufficiently smooth subsurface models commonly used in seismology, equation (7.2.5) can be expected to give an accurate representation of the quartic moveout coefficient and therefore the magnitude of nonhyperbolic moveout.

The form of the azimuthal dependence of the coefficient A_4 in equation (7.2.5) is governed by the derivatives of the zero-offset traveltime τ_0 with respect to the coordinates of the common midpoint and zero-offset reflection point. For relatively simple

models, the traveltime τ_0 can be expressed explicitly as a function of $\mathbf{y}$ and $\mathbf{x}$, and the derivatives in equation (7.2.5) can be evaluated in closed form. However, if the medium is laterally heterogeneous or has a low anisotropic symmetry, it is convenient to express equation (7.2.5) in terms of the horizontal slowness component of the zero-offset ray (Cohen, 1998; Grechka et al., 1999). Most important, all derivatives in equation (7.2.5) can be evaluated using quantities computed during the tracing of the zero-offset ray.

7.3 Quartic coefficient in a homogeneous TTI layer

While equation (7.2.5) is completely general, the treatment here is restricted to analysis of nonhyperbolic moveout in a homogeneous TTI layer overlaying a planar dipping reflector. Furthermore, we assume that the symmetry axis is confined to the dip plane of the reflector, which is typical for dipping TI formations (e.g., shales) in fold-and-thrust belts (Isaac and Lawton, 1999) or near salt domes (Tsvankin, 1997a). Hyperbolic reflection moveout and the dependence of NMO velocity on the anisotropic parameters for this model was discussed by Tsvankin (1997a, 2001) and Grechka and Tsvankin (2000). As in Chapter 4, we parametrize the medium by the symmetry-direction velocities of P-waves (V_{P0}) and S-waves (V_{S0}) and Thomsen's anisotropic coefficients ϵ, δ, and γ specified with respect to the symmetry axis. In other words, the parameters are defined by the VTI equations in the rotated coordinate system whose x_3-axis is aligned with the axis of symmetry. The tilt ν of the symmetry axis is considered positive if the axis points toward the reflector (i.e., if the symmetry axis and the reflector normal deviate from the vertical in the same direction).

Since the dip plane of the reflector contains the symmetry axis of the overburden, it represents a vertical symmetry plane for the whole model. Therefore, the dip and strike directions of the reflector determine the principal axes of the azimuthally-varying quartic moveout coefficient A_4. Below, we use equation (7.2.5) to study the functional form of A_4 in a TTI layer and its dependence on the reflector dip and anisotropic parameters.

For a homogeneous medium, the zero-offset traveltime τ_0 can be expressed explicitly in terms of the CMP and reflection-point coordinates (see Appendix J). This allows us to evaluate the spatial derivatives of τ_0 and obtain the coefficient A_4 from equation (7.2.5). While the exact equation for the quartic coefficient is suitable for computational purposes, it does not provide analytic insight into the dependence of A_4 on the model parameters. As demonstrated in Appendix J, significant simplification can be achieved by applying the weak-anisotropy approximation and linearizing equation (7.2.5) in the anisotropic parameters.

Although the discussion of the weak-anisotropy results below is formally limited to P-waves, any kinematic signature of SV-waves (i.e., of the mode polarized in the plane formed by the slowness vector and the symmetry axis) for weak transverse isotropy can be obtained from the corresponding P-wave signature by making the following substitutions: $V_{P0} \rightarrow V_{S0}$, $\delta \rightarrow \sigma$, and $\epsilon \rightarrow 0$ (Tsvankin, 2001). The parameter $\sigma \equiv (V_{P0}/V_{S0})^2(\epsilon - \delta)$ is fully responsible for SV-wave velocity variations in weakly anisotropic TI media.

The linearized P-wave quartic moveout coefficient in a TTI layer can be written as (Appendix J)

$$A_4^{\mathrm{TTI}} = -\frac{2\,\eta}{t_{P0}^2\,V_{P0}^4}\,F(\alpha,\,\phi,\,\nu)\,, \tag{7.3.6}$$

where the function F is defined in equation (J.1.14), t_{P0} is the two-way zero-offset traveltime, α is the azimuth of the CMP line measured from the dip plane, and ϕ is the reflector dip.

Figure 7.2 shows that the linearized equation (7.3.6) is sufficiently close to the exact quartic coefficient for relatively small values of the anisotropic parameters. The diamonds in Figure 7.2 correspond to the coefficient A_4 obtained by least-squares fitting of a quartic polynomial to reflection traveltimes generated by anisotropic ray tracing. Clearly, equation (7.3.6) (solid curve) provides a good approximation to the best-fit values of A_4 for the full range of azimuths. As demonstrated by Tsvankin and Thomsen (1994), the weak-anisotropy approximation may rapidly lose its accuracy with increasing values of the parameters ϵ and δ. However, equation (7.3.6) can still be used for qualitative analysis of nonhyperbolic moveout in tilted TI media.

7.3.1 Analysis of the approximate quartic coefficient

It is clear from equation (7.3.6) that regardless of the tilt of the symmetry axis and reflector dip, the P-wave quartic moveout for weak transverse isotropy is controlled by a single anisotropic parameter – the anellipticity coefficient η. If the medium is elliptical ($\eta = 0$), A_4 vanishes and reflection moveout becomes purely hyperbolic. This is a general result valid for an elliptically anisotropic layer with any strength of the anisotropy (Uren et al., 1990).

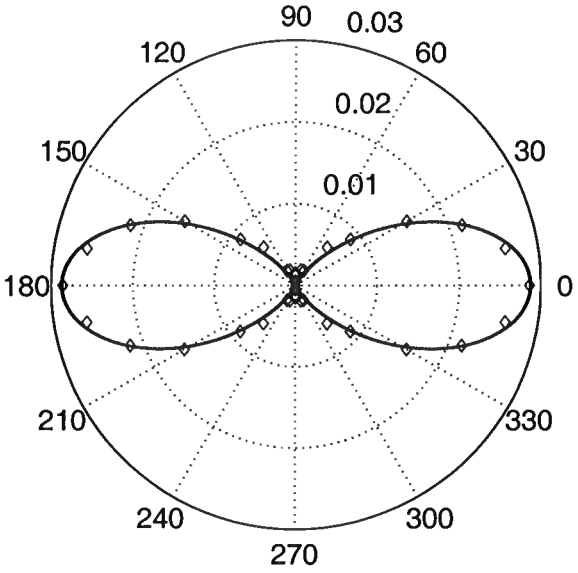

FIG. 7.2. Accuracy of the linearized quartic moveout coefficient for a tilted TI layer. The diamonds mark values of A_4 obtained for each azimuth by fitting a quartic polynomial to the ray-traced $t^2(x^2)$–curve on the spreadlength $X_{\max} \approx 1.25z$, where $z = 1$ km is the reflector depth. The solid line is the weak-anisotropy approximation (7.3.6). The model parameters are $V_{P0} = 1$ km/s, $\epsilon = 0.1$, $\delta = 0.025$, $\phi = 0°$, and $\nu = 80°$.

7.3.2 Dip and strike components of A_4

Equations (7.3.6) and (J.1.14) can be used to find the coefficients A_4 in the dip and strike directions. On the dip line ($\alpha = 0°$),

$$A_{4,\text{dip}}^{\text{TTI}}(\phi) = -\frac{2\,\eta}{t_{P0}^2\,V_{P0}^4}\,\cos^3\phi\,\cos(4\nu - 3\phi)\,. \tag{7.3.7}$$

Note that the quartic coefficient is proportional to $\cos^3\phi$, and the magnitude of nonhyperbolic moveout has a general decreasing trend with dip [the influence of the term $\cos(4\nu - 3\phi)$ is discussed below]. Equation (7.3.7), however, becomes less accurate for near-vertical reflectors because for ϕ close to 90° several terms involving anisotropic coefficients can no longer be treated as small. Evaluation of the exact

equation (7.2.5) shows that unless the symmetry axis is vertical or horizontal, A_4 for a vertical reflector ($\phi = 90°$) is relatively small but does not go to zero.

According to equation (7.3.7), the quartic moveout coefficient (and, therefore, nonhyperbolic moveout as a whole) vanishes if $\cos(3\phi - 4\nu) = 0$, or $(3\phi - 4\nu) = n\pi/2$ ($n = \pm 1, \pm 3, \pm 5, ...$). In the special case of VTI media ($\nu = 0$), the quartic coefficient and nonhyperbolic moveout as a whole vanish for a dip of 30° (see a more detailed discussion of the VTI model below).

Since the argument $3\phi - 4\nu$ is a linear combination of ϕ and ν, zero values of $\cos(3\phi - 4\nu)$ are represented by straight lines. For instance, $3\phi - 4\nu = -\pi/2$, or

$$\nu = \frac{3\phi}{4} + \frac{\pi}{8}. \tag{7.3.8}$$

For a fixed reflector dip, $\cos(3\phi - 4\nu)$ goes to zero for two different values of the tilt ν between 0° and 90°, which is in good agreement with the computations of analytic (NMO) and finite-spread moveout velocity in Tsvankin (1995, 2001). Hence, the absence or low magnitude of dip-line nonhyperbolic moveout in nonelliptical ($\eta \neq 0$) TTI media may be used to constrain the relationship between the reflector dip and the tilt of the symmetry axis.

Equation (7.3.7) is written in terms of reflector dip, which cannot be estimated from surface reflection data unless the velocity model is known. Therefore, for purposes of anisotropic parameter estimation, it is more convenient to rewrite the quartic coefficient as a function of the horizontal component p of the slowness vector associated with the zero-offset ray (e.g., Alkhalifah and Tsvankin, 1995). The horizontal slowness component, or the ray parameter, determines the slope of reflections on zero-offset

Processing parameters (TTI)		
$V_{P,\mathrm{nmo}}$	$\eta \cos 4\nu$	$\eta \sin 4\nu$
Processing parameters (VTI)		
$V_{P,\mathrm{nmo}}$	η	0

Table 1. Correspondence between the parameters responsible for the kinematic signatures of P-waves in anisotropic TTI and VTI media. It is assumed that the CMP line for TTI media lies in the dip plane that also contains the symmetry axis. The parameter description for TTI media is valid if the anisotropy is weak.

(or stacked) sections and can be measured directly from surface data.

Substituting the ray parameter $p = \sin\phi/V(\phi)$ [$V(\phi)$ is the phase velocity at dip ϕ] into equation (7.3.7) yields

$$A_{4,\mathrm{dip}}^{\mathrm{TTI}}(p) = \frac{8\,(1-y)^3}{t_{P0}^2\,[V_{\mathrm{nmo,dip}}^{\mathrm{TTI}}(0)]^4}\left[\left(y-\frac{1}{4}\right)\sqrt{1-y}\,\eta\cos 4\nu + \left(y-\frac{3}{4}\right)\sqrt{y}\,\eta\sin 4\nu\right], \quad (7.3.9)$$

where

$$y \equiv p^2\,[V_{\mathrm{nmo}}^{TTI}(0)]^2 \quad (7.3.10)$$

and $V_{\mathrm{nmo}}^{TTI}(0)$ is the NMO velocity from a horizontal reflector. Hence, $A_{4,\mathrm{dip}}^{\mathrm{TTI}}$ expressed as a function of p depends on three parameters: $V_{\mathrm{nmo}}^{TTI}(0)$, η, and ν [or $V_{\mathrm{nmo}}^{TTI}(0)$, $\eta\cos 4\nu$, and $\eta\sin 4\nu$] (Table 1). In principle, the quartic moveout coefficient can be inverted for these parameters, if accurate estimates of $A_{4,\mathrm{dip}}^{\mathrm{TTI}}$ are available for three different dips. The high level of structural complexity in overthrust areas or near salt domes in some cases may be sufficient for reconstructing the function $A_{4,\mathrm{dip}}^{\mathrm{TTI}}(p)$. However, as discussed by Grechka and Tsvankin (1998a), the trade-off between the NMO velocity and quartic moveout coefficient typically leads to substantial uncertainty in A_4.

In anisotropic parameter estimation, nonhyperbolic moveout should be used in combination with the NMO velocity (e.g., Alkhalifah, 1997; Grechka and Tsvankin, 1998a). The dip-line P-wave NMO velocity for weakly anisotropic TTI media was given by Tsvankin (1997a, 2001) as a function of dip. Rewriting his result through the ray parameter p yields

$$V_{\rm nmo}^{\rm TTI}(p) = \frac{V_{\rm nmo}^{TTI}(0)}{\sqrt{1-y}}\left[1 + f\,\eta\cos 4\nu - g\,\eta\sin 4\nu\right], \tag{7.3.11}$$

where

$$f \equiv \frac{y}{1-y}\left(6 - 9y + 4y^2\right) \tag{7.3.12}$$

and

$$g \equiv \sqrt{\frac{y}{1-y}}\left(3 - 7y + 4y^2\right). \tag{7.3.13}$$

For vertical transverse isotropy ($\nu = 0$), equation (7.3.11) reduces to the expression derived by Alkhalifah and Tsvankin (1995). Note that, both the dip-line NMO velocity and the quartic moveout coefficient are fully governed by the same parameter combinations: $V_{\rm nmo}^{\rm TTI}(0)$, $\eta\cos 4\nu$, and $\eta\sin 4\nu$. According to Tsvankin (1997a, 2001), however, the weak-anisotropy approximation for NMO velocity loses accuracy for anisotropic coefficients reaching 0.15-0.2, and the exact $V_{\rm nmo}$ becomes dependent on the individual values of ϵ and δ.

Next, we analyze the strike component of the quartic moveout coefficient that can be obtained by substituting $\alpha = 90^\circ$ into equation (7.3.6):

$$A_{4,\text{strike}}^{\text{TTI}}(\phi) = -\frac{2\,\eta}{t_{P0}^2\,V_{P0}^4}\,\cos^4(\phi-\nu)\,. \tag{7.3.14}$$

Both the dip and strike components of A_4 are proportional to η, but their dependencies on reflector dip ϕ and the symmetry-axis tilt ν are entirely different. Equation (7.3.14) shows that $A_{4,\text{strike}}^{\text{TTI}}$ goes to zero only if the symmetry axis is perpendicular to the reflector normal (i.e., the symmetry axis is confined to the reflecting plane). For example, if the reflector is vertical ($\phi = 90°$), the strike-line quartic coefficient vanishes for VTI media ($\nu = 0°$). Indeed, for such a model, reflected rays are confined to the horizontal (isotropy) plane where velocity is independent of angle, which makes reflection moveout for any azimuth purely hyperbolic. On the whole, the dip and strike components of the quartic coefficient vanish for different combinations of ν and ϕ and, therefore, can be effectively combined in an inversion procedure.

If the symmetry axis is orthogonal to the reflector ($\phi = \nu$), $A_{4,\text{strike}}^{\text{TTI}}$ is independent of both dip and tilt:

$$A_{4,\text{strike}}^{\text{TTI}} = -\frac{2\,\eta}{t_{P0}^2\,V_{P0}^4}\,. \tag{7.3.15}$$

Equation (7.3.15) is known for the special case of VTI media and a horizontal reflector, i.e., when $\phi = \nu = 0$ (Tsvankin and Thomsen, 1994). Another special case of interest is that of an HTI layer ($\nu = 90°$) and a vertical reflector ($\phi = 90°$). Since the strike line for this model is perpendicular to the symmetry axis, and reflected rays are horizontal, reflection moveout in the strike direction is identical to that for a VTI layer above a horizontal reflector.

The dip-line component of A_4 for $\phi = \nu$ is proportional to $\cos^4\nu$ [equation (7.3.7)], so it rapidly decreases with dip, while the strike-line component remains constant.

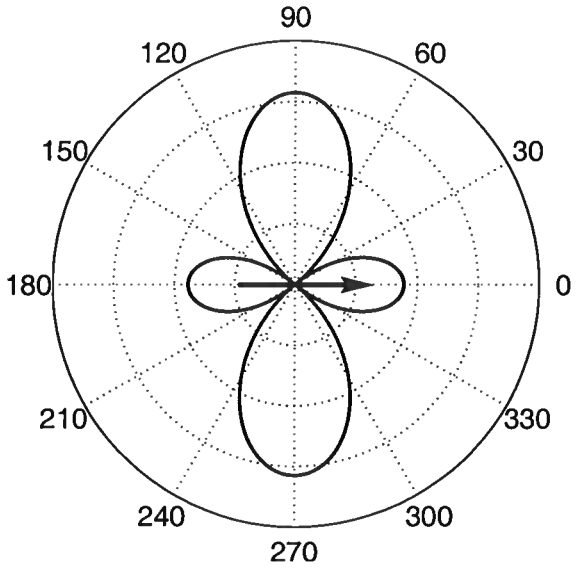

FIG. 7.3. Azimuthally-varying quartic moveout coefficient A_4 for a TTI layer computed from equation (7.3.6). The polar radius is equal to the coefficient A_4 in the corresponding azimuthal direction (the azimuth is measured from the dip plane marked by the arrow). The reflector dip is $\phi = 15°$, and the tilt of the symmetry axis is 40°; the other parameters change only the scale of the plot (intentionally undefined here).

Therefore, nonhyperbolic moveout from dipping reflectors for this model should be measured close to the strike direction; a more detailed discussion of the azimuthal dependence of A_4 is given below.

7.3.3 Azimuthal dependence of A_4

Unlike NMO velocity that has a simple elliptical azimuthal dependence (Grechka and Tsvankin, 1998b), the variation of the quartic moveout coefficient with azimuth has a much more complicated character. The nonlinear relationship between A_4 and the angles ϕ, ν, and α [equation (7.3.6)] leads to multiple zeros of the function $A_4(\alpha)$ whose positions strongly depend on both dip ϕ and tilt ν. Figure 7.3 displays a

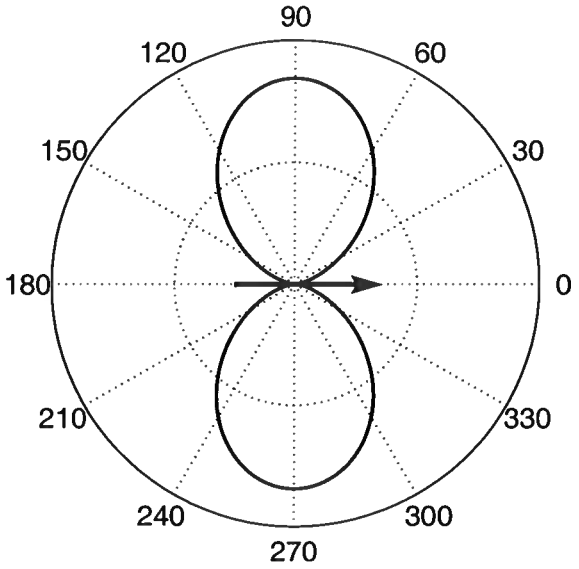

FIG. 7.4. Azimuthally-varying coefficient A_4 for a VTI layer computed from equation (7.3.19). Reflector dip is 30°, and the dip direction is marked by the arrow.

polar plot with a typical azimuthal signature of the quartic coefficient in TTI media. Clearly, A_4 exhibits much more variability compared to the NMO ellipse, with zeros at azimuths of 38° and 142°. (The quartic coefficient and moveout signature as a whole have an azimuthal period of 180°.) The sign of the coefficient A_4 changes from positive near the dip direction (i.e., for the horizontally oriented lobe in the figure) to negative for the other lobe corresponding to $38° < \alpha < 142°$.

These plots suggest that the azimuthal signature of the quartic coefficient can provide useful information for anisotropic parameter estimation. In particular, the azimuthal directions of the CMP lines with vanishing A_4 depend on certain combinations of ϕ and ν and can be used to constrain the orientation of the symmetry axis [equation (7.3.6)]. The variation of the sign of A_4 with azimuth is also sensitive to both ϕ and ν.

7.3.4 Symmetry axis orthogonal to the reflector

Because of the complicated structure of equation (7.3.6), here we focus on several special cases of practical importance. Models with the symmetry axis orthogonal to the reflector ($\phi = \nu$) are believed to be typical for fold-and-thrust belts (e.g., the Canadian Foothills) where the anisotropy is caused by dipping TI shale layers. For TI media with $\phi = \nu$, the zero-offset ray is parallel to the symmetry axis and orthogonal to the reflector, so some features of reflection moveout are similar to those for a horizontal VTI layer. For example, Tsvankin (1995, 2001) demonstrated that if $\phi = \nu$, the dip-line NMO velocity obeys the conventional (isotropic) cosine-of-dip dependence.

The dip and strike components of the quartic coefficient for this model were discussed above. To study the azimuthal dependence of A_4, we substitute $\phi = \nu$ into equation (7.3.6) to obtain

$$A_4^{\mathrm{TTI}}(\phi = \nu) = -\frac{2\,\eta}{t_{P0}^2\,V_{P0}^4}\left(1 - \sin^2\nu\cos^2\alpha\right)^2 . \tag{7.3.16}$$

According to equation (7.3.16), the quartic coefficient goes to zero when

$$|\cos\alpha| = \frac{1}{|\sin\nu|} . \tag{7.3.17}$$

Condition (7.3.17) can be satisfied only on the dip line ($\alpha = 0°$) of a vertical reflector ($\nu = 90°$, which implies a horizontal symmetry axis). Away from the dip line, the coefficient A_4 for a vertical reflector varies as

$$A_4^{\mathrm{TTI}}(\phi = \nu = 90°) = -\frac{2\,\eta}{t_{P0}^2\,V_{P0}^4}\sin^4\alpha . \tag{7.3.18}$$

Equation (7.3.18) shows that A_4 rapidly decays with increasing deviation from the strike direction ($\alpha = 90°$). This conclusion remains valid for arbitrary reflector dip because the strike component for this model is independent of ν and α [equation (7.3.15)], while the dip component is proportional to $\cos^4 \nu$.

7.3.5 Dipping reflector beneath a VTI layer

Setting the tilt ν of the symmetry axis in equation (7.3.6) to zero yields the weak-anisotropy approximation for the quartic coefficient in VTI media

$$A_4^{\mathrm{VTI}} = -\frac{2\,\eta\,\cos^4\phi}{t_{P0}^2\,V_{P0}^4}\left(1 - 4\,\sin^2\phi\,\cos^2\alpha\right). \tag{7.3.19}$$

For a vertical reflector ($\phi = 90°$), A_4 vanishes regardless of the azimuth of the CMP line because reflected rays are confined to the horizontal isotropy plane where velocity is constant and moveout is purely hyperbolic. If the reflector is horizontal ($\phi = 0°$), the model as a whole is azimuthally isotropic, and the approximate A_4 is determined by the well-known expression (Tsvankin and Thomsen, 1994; Alkhalifah and Tsvankin, 1995)

$$A_4^{\mathrm{VTI}}(\phi = 0°) = -\frac{2\,\eta}{t_{P0}^2\,V_{P0}^4}. \tag{7.3.20}$$

A discussion of the exact (i.e., not limited to weak anisotropy) quartic moveout coefficient of both P- and S-waves in horizontally layered VTI media can be found in Tsvankin (2001).

For a dipping reflector, the coefficient A_4 vanishes in azimuthal directions satisfying

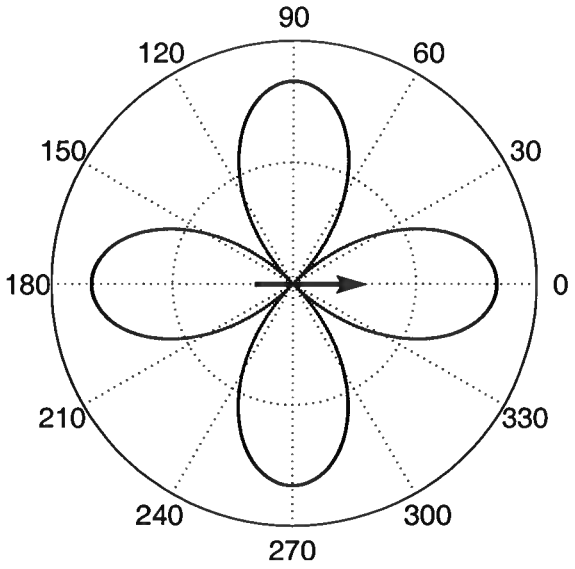

FIG. 7.5. Same as Figure 7.4, but the reflector dip is 45°.

$$|\cos\alpha| = \frac{1}{2\sin\phi}\,. \tag{7.3.21}$$

If the dip is equal to 30°, A_4 goes to zero only for a single azimuth $\alpha = 0°$ that corresponds to the dip plane (Figure 7.4). This analytic result is in good agreement with the numerical study of NMO velocity in Tsvankin (1995, 2001), who showed that the P-wave dip-line moveout approaches to a hyperbola for reflector dips relatively close to 30°.

For any dip between 30° and 90°, equation (7.3.19) yields two azimuths α (plus two more azimuths different by ±180°) for which $A_4 = 0$. If the dip is equal to 45°, the quartic coefficient vanishes for azimuth $\alpha = \pm 45°$ (Figure 7.5). The sign of A_4 is positive near the dip plane ($-45° < \alpha < 45°$) and negative near the strike direction ($45° < \alpha < 135°$). If the dip is less than 30°, equation (7.3.21) does not have a solution, and $A_4 < 0$ for all azimuths (Figure 7.6).

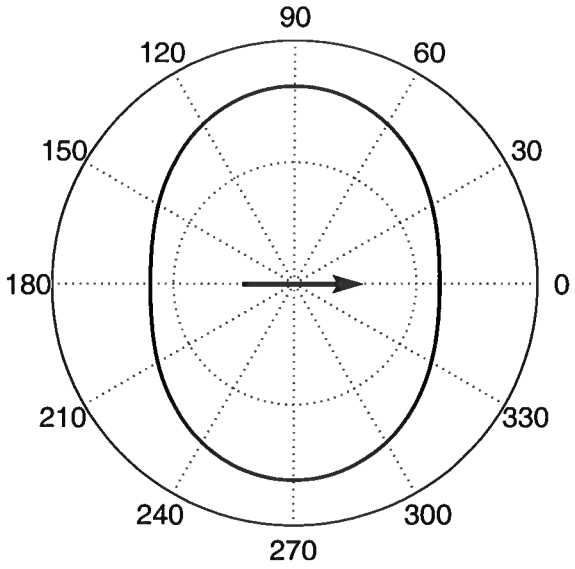

FIG. 7.6. Same as Figure 7.4, but the reflector dip is 15°.

7.3.6 Horizontal HTI layer

For a horizontal HTI layer ($\nu = 90°$ and $\phi = 0°$), equation (7.3.6) reduces to

$$A_4^{\mathrm{HTI}} = -\frac{2\,\eta}{t_{P0}^2\,V_{P0}^4}\,\cos^4\alpha\,. \tag{7.3.22}$$

Equation (7.3.22) has the same azimuthal dependence ($\cos^4\alpha$) as the exact expression for A_4 obtained by Al-Dajani and Tsvankin (1998). In the equation given by Al-Dajani and Tsvankin, however, the factor multiplied with $\cos^4\alpha$ corresponds to the exact quartic coefficient in the plane that contains the symmetry axis ($\alpha = 0°$). The quartic coefficient vanishes in the isotropy plane orthogonal to the symmetry axis ($\alpha = 90°$), where reflection moveout is thus purely hyperbolic.

7.3.7 Physical modeling results

Here, we show some results obtained by Isaac and Lawton (1999). They built a 2-D physical model to investigate the magnitude of imaging errors incurred by isotropic processing when anisotropy is present in the dipping overburden. Figure 7.7**a** shows an sketch of the model, and Figure 7.7**b** shows the migrated zero-offset section. Figure 7.8 demonstrates that for this particular model, the moveout of the reflection from the bottom of the TTI layer is almost hyperbolic; that is, the magnitude of the nonhyperbolic moveout is very small. This result is in agreement with the theoretical results presented above. From the theory described before, it is possible to predict that if the model has only one horizontal TTI layer, the magnitude of the nonhyperbolic moveout along the x_1-direction is small for mild tilts (the plane $[x_1, x_3]$ contains the symmetry axis).

7.4 Summary

This chapter introduces an exact expression for the quartic moveout coefficient A_4 valid for arbitrarily anisotropic, heterogeneous media. Unlike most existing methods, the approach used here does not require the model to have a horizontal symmetry plane and accounts for reflection-point dispersal on dipping or irregular interfaces. Substitution of the quartic coefficient into the general moveout equation of Tsvankin and Thomsen (1994) yields a good approximation for nonhyperbolic moveout of P-waves and, in some cases, mode-converted PS-waves in anisotropic media with realistic structural complexity.

It should be emphasized that all quantities needed to calculate the azimuthally-

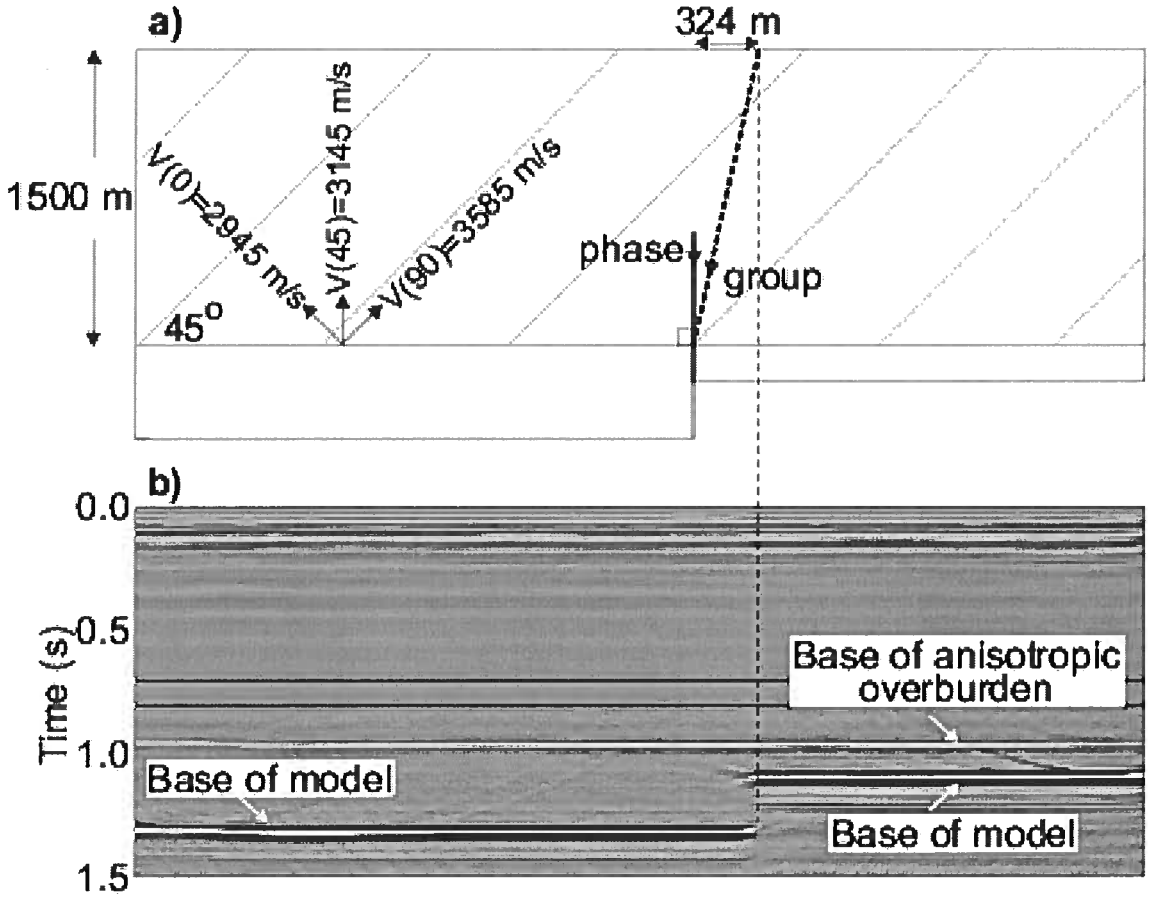

FIG. 7.7. **a)** Scaled physical model built by Isaac and Lawton (1999). The model is composed of two layers. The first layer has TTI symmetry; it was made with phenolic material. The second layer is isotropic, and it was made with Plexiglass. **b)** migrated zero-offset section.

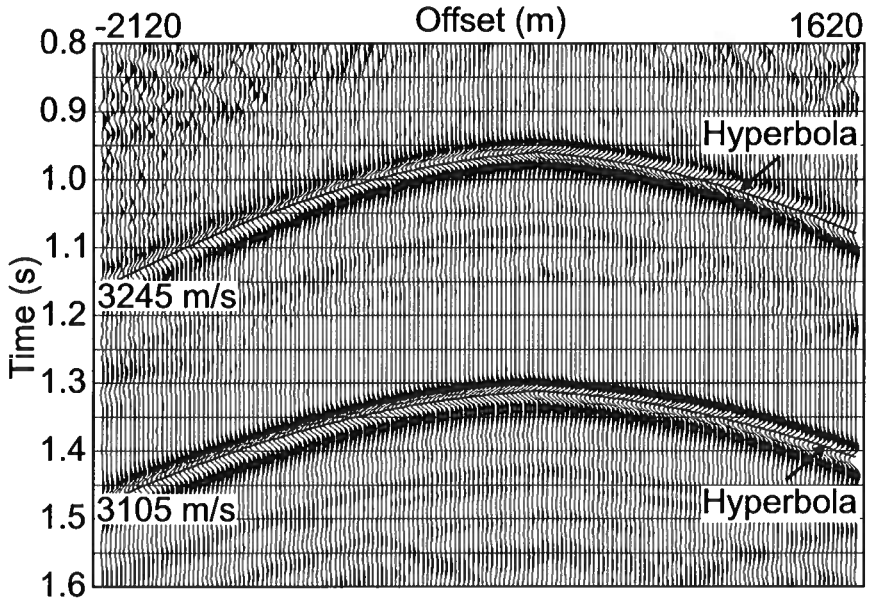

FIG. 7.8. Shot gather showing that the moveout of the reflection from the bottom of the TTI layer is close to hyperbolic. The parameters of the TTI layer are: $\epsilon = 0.18$, $\delta = 0.08$, and $\nu = 45°$.

varying quartic coefficient can be obtained by tracing a single (zero-offset) ray. Computing the zero-offset ray is also sufficient to construct the NMO ellipse (i.e., the azimuthally varying NMO velocity) responsible for short-spread moveout (Grechka et al., 1999; Grechka and Tsvankin, 2002a). Therefore, the results of this chapter can be used to model azimuthally dependent long-spread moveout in a computationally efficient way, without time-consuming multi-offset, multi-azimuth ray tracing.

The general equation for A_4 was applied to study the properties of P-wave nonhyperbolic moveout in TI media with arbitrary orientation of the symmetry axis. The analysis was restricted to a homogeneous TI layer above a planar horizontal or dipping reflector; it was assumed that the symmetry axis is confined to the dip plane. To gain insight into the the dependence of the quartic moveout coefficient on the model parameters, we simplified the exact expression by linearizing it in the anisotropic parameters. The derived weak-anisotropy approximation is proportional to the anisotropic time-processing parameter $\eta \approx \epsilon - \delta$, so the magnitude of nonhyperbolic moveout increases as the model deviates from elliptical ($\epsilon = \delta$).

While the azimuthal dependence of A_4 is a rather complicated function of the reflector dip ϕ and the tilt ν of the symmetry axis, the expressions for the quartic coefficients in the principal (dip and strike) directions are relatively simple. In particular, the strike component of A_4 depends solely on the *difference* between the dip and tilt rather than on their individual values. The magnitude of the dip component is proportional to $\cos^3\phi$, so it rapidly decreases with ϕ. For a fixed dip, the dip-line quartic coefficient vanishes for two values of the tilt between 0° and 90°.

While the azimuthal dependence of NMO velocity typically has a simple elliptical form, the azimuthal variation of the quartic coefficient in tilted TI media turns out to

be more complicated, sometimes with A_4 vanishing in several azimuthal directions. The azimuthal positions of the zeros of the quartic coefficients and the signs of A_4 in different azimuthal sectors are largely governed by the tilt ν and reflector dip ϕ (η plays the role of a scaling coefficient). In realistic heterogeneous media, nonhyperbolic moveout is also caused by vertical and lateral velocity gradients, but anisotropy usually makes a more significant contribution to A_4 (Alkhalifah, 1997). In particular, the azimuthal dependence of nonhyperbolic moveout over a medium containing a tilted TI layer should be well-described by the equations given in this paper.

In the important special case of the symmetry axis orthogonal to the reflector ($\phi = \nu$), the quartic coefficient goes to zero only on the dip line of a vertical reflector. For this model, the strike-line A_4 is independent of dip (and tilt) and has the same value as in VTI media, while the dip-line A_4 decreases with dip as $\cos^4 \phi$. Therefore, the magnitude of nonhyperbolic moveout for $\phi = \nu$ is significant mostly for azimuthal directions close to the reflector strike. If the medium is VTI and reflector dip is mild ($\phi < 30°$), A_4 is negative for all azimuths, and its magnitude increases away from the dip direction. For a 30° dip, nonhyperbolic moveout in VTI media vanishes on the dip line, which agrees with existing numerical results (Tsvankin, 1995, 2001). If the dip exceeds 30°, A_4 goes to zero in two azimuths that do not coincide with either strike or dip directions.

For purposes of anisotropic parameter estimation, moveout equations have to be rewritten in terms of the ray parameter p that can be determined from reflection slopes on zero-offset (or stacked) sections. The dip components of both A_4 and NMO velocity expressed through p depend on the same three parameter combinations involving η, ν, and the NMO velocity from a horizontal reflector. This result and the high sensitivity of the azimuthal signature of A_4 to the symmetry-axis orienta-

tion indicate that P-wave nonhyperbolic moveout may provide valuable information for velocity analysis in TTI media. Although the trade-off between V_{nmo} and A_4 makes quantitative estimates of the quartic coefficient relatively unstable (Grechka and Tsvankin, 1998a), the azimuthal variation of the sign of A_4 and the directions of vanishing or small nonhyperbolic moveout should be detectable from wide-azimuth reflection data.

Chapter 8

DISCUSSIONS AND CONCLUSIONS

8.0.1 Conclusions

I introduced stacking-velocity tomography for wide-azimuth P-wave reflection data. If the overburden contains dipping interfaces, P-wave NMO ellipses measured from multi-azimuth 3-D reflection data over layered VTI media depend on all three relevant interval Thomsen parameters ($V_{0,n}$, ϵ_n, and δ_n).

If the interfaces have different azimuths and do not cross each other, the P-wave NMO ellipses in an N-layer model yield $3N-1$ independent equations for the $3N$ interval VTI parameters $V_{0,n}$, ϵ_n, and δ_n. The spatial variation of the NMO ellipses for this model does not provide any additional information for the inversion procedure. Therefore, in general surface 3-D P-wave data alone are insufficient to determine the unknown VTI parameters and reconstruct the interfaces in a unique fashion. For 2-D models with co-oriented interfaces, the axes of all NMO ellipses are parallel to the dip and strike directions, and the number of independent equations reduces further to $2N$.

This ambiguity, however, can be overcome if a *single* parameter in any layer (for 3-D models) is known *a priori*. For example, in many cases the subsurface layer may be assumed to be isotropic ($\epsilon_1 = \delta_1 = 0$), or the vertical velocity in it may be estimated

in a shallow borehole. The inversion can also be made unique by introducing some relationship between the parameters (e.g., between ϵ and δ) in at least one of the layers. The only model for which this approach fails to remove the ambiguity (for P-wave data) is elliptical anisotropy ($\epsilon_n = \delta_n$).

In contrast to media with planar interfaces, for VTI media with irregular interfaces it may be possible to reconstruct the model in depth from P-wave reflection traveltimes alone. Interface curvature increases the angle coverage of reflected rays, which helps to constrain the parameters of the anisotropic velocity field. Only if the anisotropy is close to elliptical, does the depth scale become poorly constrained by P-wave data regardless of the interface shape, which agrees with the results of Dellinger and Muir (1988).

I also extended stacking-velocity tomography to mulicomponent (P and S) data. The tomographic algorithm is designed to invert wide-azimuth traveltimes of P and S-wave reflections (in general, using two split S-waves) for the interval parameters of TI media. Although the method does not operate directly with converted PS-waves, it can still be applied in multicomponent ocean-bottom surveys. Prior to the anisotropic velocity analysis, PS data are combined with the PP-wave moveout from the same interface to compute the reflection traveltimes of SS-waves using the model-independent kinematic technique of Grechka and Tsvankin (2002b).

The multicomponent tomography was implemented for a stack of transversely isotropic layers separated by smooth interfaces. The detailed analysis for a homogeneous TI medium and numerical testing for layered models show that for a range of reflector dips and tilt angles of the symmetry axis, the combination of PP and PSV (or $SVSV$) data can be used to build anisotropic models for depth processing. The most

notable exception is horizontally layered VTI media, where even long-spread (nonhyperbolic) moveout of PP- and PSV-waves does not constrain the vertical velocities (Grechka and Tsvankin, 2002c).

The inversion of P-wave stacking velocities was applied to 2D physical-modeling data of Leslie and Lawton (1996). This physical model, which contains a bending TTI layer, was built to simulate the distinctive features of typical reflection data acquired over TTI shale layers in the Alberta Foothills. Two important constraints on the TTI model were provided by the geologically justified assumptions that the symmetry axis is orthogonal to the bedding and the TTI layer is homogeneous. Another, more arbitrary assumption used in the inversion procedure was that the bottom of the model is horizontal. This assumption, however, would have been unnecessary if the acquisition geometry had been suitable for processing reflections from steep interfaces in the shallow portion of the model. The assumptions made it possible to estimate all model parameters from P-wave reflection traveltimes.

The multicomponent stacking-velocity tomography was further generalized for orthorhombic media. A number of synthetic tests on noise-contaminated data for typical orthorhombic models showed that, for a single layer, noise does not get amplified by the inversion algorithm, and the anisotropic inversion is stable. In contrast, the estimated anisotropic parameters in layered orthorhombic media often are significantly distorted as a result of error accumulation with depth and a reduced sensitivity of surface data to the parameters of deeper layers. This instability in stacking-velocity tomography can be avoided or reduced by supplementing the surface data with constraints on the vertical velocities of the P- and S-waves measured from well logs or check shots. This constraint makes the inversion results sufficiently stable for application in quantitative fracture characterization for orthorhombic reservoir models

(Bakulin et al., 2000).

While the above algorithms operate with NMO velocities or ellipses, I also introduced an exact expression for the quartic moveout coefficient A_4 valid for arbitrarily anisotropic, heterogeneous media. Unlike most existing methods, the approach used here does not require the model to have a horizontal symmetry plane and accounts for reflection-point dispersal on dipping or irregular interfaces. Substitution of the quartic coefficient into the general moveout equation of Tsvankin and Thomsen (1994) yields a good approximation for nonhyperbolic moveout of P-waves and, in some cases, mode-converted PS-waves in anisotropic media with realistic structural complexity.

It should be emphasized that all quantities needed to calculate the azimuthally-varying quartic coefficient can be obtained by tracing a single (zero-offset) ray. Computing the zero-offset ray is also sufficient to construct the NMO ellipse (i.e., the azimuthally varying NMO velocity) responsible for conventional-spread moveout (Grechka et al., 1999b; Grechka and Tsvankin, 2002a). Therefore, these results can be used to model azimuthally dependent long-spread moveout in a computationally efficient way, without time-consuming multi-offset, multi-azimuth ray tracing.

The general equation for A_4 was applied to study the properties of P-wave nonhyperbolic moveout in TI media with arbitrary orientation of the symmetry axis. The analysis was restricted to a homogeneous TI layer above a planar horizontal or dipping reflector; it was assumed that the symmetry axis is confined to the dip plane. The derived linearized expression for A_4 is proportional to the anisotropic P-wave time-processing parameter $\eta \approx \epsilon - \delta$, so the magnitude of nonhyperbolic moveout increases as the model deviates from elliptical ($\epsilon = \delta$).

In the important special case of the symmetry axis orthogonal to the reflector ($\phi = \nu$), the quartic coefficient goes to zero only on the dip line of a vertical reflector. For this model, the strike-line A_4 is independent of dip (and tilt) and has the same value as in VTI media, while the dip-line A_4 decreases with dip as $\cos^4\phi$. Therefore, the magnitude of P-wave nonhyperbolic moveout for $\phi = \nu$ is significant mostly for azimuthal directions close to the reflector strike. If the medium is VTI and reflector dip is mild ($\phi < 30°$), A_4 is negative for all azimuths, and its magnitude increases away from the dip direction. For a 30° dip, nonhyperbolic moveout in VTI media vanishes on the dip line, which agrees with existing numerical results (Tsvankin, 1995, 2001). If the dip exceeds 30°, A_4 goes to zero in two azimuths that coincide with neither strike nor dip directions. These results can be used to constrain the symmetry-axis orientation.

In all the inversions presented in this work, the magnitude of the objective function evaluated at the initial guess was always greater than 1.

8.0.2 Future work

Recently Grechka et al. (2002) successfully applied stacking-velocity tomography to 2D field data (PP- and PSV-waves). The full potential of multicomponent stacking-velocity tomography can be realized by applying it to 3D data. To do so, it is necessary to recover the two pure shear-wave traveltimes (S_1S_1 and S_2S_2) from PP, PS_1, and PS_2 data using the $PP + PS = SS$ method. This is a challenging task that requires identification of the two converted waves (PS_1 and PS_2), which involves treating such problems as geophone coupling, vector fidelity, irregular acquisition geometries, random noise, and multiples. Clearly, the presence of lateral heterogeneity is a major

challenging problem for stacking-velocity tomography and one that requires further research. Another source of problems for stacking-velocity tomography may be the absence of sharp interfaces; smooth transition zones between layers may give rise to inaccurate estimates of the S_1S_1 and S_2S_2 traveltimes.

The joint inversion of near and far offsets is another subject requiring further investigation. This joint inversion may have some advantages over full-scale tomography; for instance, the azimuthally varying hyperbolic and nonhyperbolic moveouts of pure modes can be reconstructed by tracing only one zero-offset ray per common midpoint and per reflector. As shown in Chapter 7, it may be feasible to get additional information from nonhyperbolic moveout; as a consequence, one may be able to get better estimates of the anisotropic parameters for lower symmetries (orthorhombic, monoclinic, etc). The practical implementation of this joint inversion is challenging for the reasons mentioned in the previous paragraph. Again, one of the critical problems in dealing with large offsets is the presence of pronounced lateral velocity variations.

REFERENCES

Al-Dajani, A., and Tsvankin, I., 1998, Nonhyperbolic reflection moveout for horizontal transverse isotropy: Geophysics, **63**, 1738–1753.

Al-Dajani, A., Tsvankin, I., and Toksoz, M.N., 1998, Nonhyperbolic reflection moveout for azimuthally anisotropic media: 68th Ann. Internat. Mtg., Soc. Expl. Geophys., Expanded Abstracts, 1479–1482.

Alford, R.M., 1986, Shear data in the presence of azimuthal anisotropy: 56th Ann. Internat. Mtg., Soc. Expl. Geophys., Expanded Abstracts, 476–479.

Alkhalifah, T., 1997, Velocity analysis using nonhyperbolic moveout in transversely isotropic media: Geophysics, **62**, 1839–1854.

Alkhalifah, T., Biondi, B., and Fomel, S., 1998, Time-domain processing in arbitrary inhomogeneous media: 68th Ann. Internat. Mtg., Soc. Expl. Geophys., Expanded Abstracts, 1756–1759.

Alkhalifah, T., and Tsvankin, I., 1995, Velocity analysis for transversely isotropic media: Geophysics, **60**, 1550–1566.

Bakulin, A., Grechka, V., and Tsvankin, I., 2000, Estimation of fracture parameters from reflection seismic data – Part II: Fractured models with orthorhombic symmetry: Geophysics, **65**, 1803–1817.

Bartel, D.C., Abriel, W.L., Meadows, M.A, and Hill, N.R., 1998, Determination of transversely isotropic velocity parameters at the Pluto Discovery, Gulf of

Mexico: 68th Ann. Internat. Mtg., Soc. Expl. Geophys., Expanded Abstracts, 1269–1272.

Blyas, E.A., Gritsenko, E.A., and Chernyak, V.S., 1984, Time field derivatives in stratified media: Soviet Geology and Geophysics, **25**, 72–77.

Bube, K.P., and Meadows, M.A., 1997, On the null space in linearized anisotropic surface reflection tomography: 67th Ann. Internat. Mtg., Soc. Expl. Geophys., Expanded Abstracts, 1677–1680.

Byun, B.S., and Corrigan, D., 1990, Seismic traveltime inversion for transverse isotropy: Geophysics, **55**, 192–200.

Cheadle, S.P., Brown, R.J., and Lawton, D.C., 1991, Orthorhombic anisotropy: A physical seismic modeling study: Geophysics, **56**, 1603–1613.

Chernjak, V. S., and Gritsenko, S. A., 1979. Interpretation of effective common-depth-point parameters for a spatial system of homogeneous beds with curved boundaries: Soviet Geology and Geophysics, **20**, N12, 91-98.

Cohen, J. K., 1998, A convenient an expression for the NMO velocity function in terms of ray parameter: Geophysics, **63**, 275–278.

Contreras, P., Grechka, V., and Tsvankin, I., 1999, Moveout inversion of P-wave data for horizontal transverse isotropy: Geophysics, **64**, 1219–1229.

Dellinger, J., and Muir, F., 1988, Imaging reflections in elliptically anisotropic media: Geophysics, **53**, 1616–1618.

Dix, C.H., 1955, Seismic velocities from surface measurements: Geophysics, **20**, 68–86.

Fomel, S., 1994, Recurrent formulas for derivatives of a CMP traveltime curve: Russian Geology and Geophysics, **35**, N2, 118-126.

Fomel, S., and Grechka V., 2001, Nonhyperbolic reflection moveout of P-waves: An overview and comparison of reasons: CWP Research Report (CWP-372).

Goldin, S.V., 1986, Seismic traveltime inversion: Soc. Expl. Geophys.

Granli, J.R., Arntsen, B., Sollid, A., and Hilde, E., 1999, Imaging through gas-filled sediments using marine shear-wave data: Geophysics, **64**, 668–667.

Gray, S.H., Maclean, G., and Marfurt, K.J., 1999, Crooked line, rough topography: advancing towards the correct seismic image: Geophys. Prosp., **47**, 721–733.

Grechka, V., 1998, Transverse isotropy versus lateral heterogeneity in the inversion of P-wave reflection traveltimes: Geophysics, **63**, 204–212.

Grechka, V., Pech, A., and Tsvankin, I., 2002a, P-wave stacking-velocity tomography for VTI media: Geophys. Prosp., **50**, 151–168.

Grechka, V., Pech, A., and Tsvankin, I., 2002b, Multicomponent stacking-velocity tomography for transversely isotropic media: Geophysics, **67**, 1564–1574.

Grechka, V., Theophanis, S., and Tsvankin, I., 1999a, Joint inversion of P- and PS-waves in orthorhombic media: Theory and a physical-modeling study: Geophysics, **64**, 146–161.

Grechka, V., and Tsvankin, I., 1998a, Feasibility of nonhyperbolic moveout inversion in transversely isotropic media: Geophysics, **63**, 957–969.

Grechka, V., and Tsvankin, I., 1998b, 3-D description of normal moveout in anisotropic inhomogeneous media: Geophysics, **63**, 1079–1092.

Grechka, V., and Tsvankin, I., 1999a, 3-D moveout velocity analysis and parameter estimation for orthorhombic media: Geophysics, **64**, 820–837.

Grechka, V., and Tsvankin, I., 1999b, 3-D moveout inversion in azimuthally anisotropic media with lateral velocity variation: Theory and a case study: Geophysics, **64**, 1202–1218.

Grechka, V., and Tsvankin, I., 2000, Inversion of azimuthally dependent NMO velocity in transversely isotropic media with a tilted axis of symmetry: Geophysics, **65**, 232–246.

Grechka, V., and Tsvankin, I., 2002a, NMO-velocity surfaces and Dix-type formulas in heterogeneous anisotropic media: Geophysics, **67**, 939–951.

Grechka, V., and Tsvankin, I., 2002b, $PP + PS = SS$: Geophysics, **67**, 1961–1971.

Grechka, V., and Tsvankin, I., 2002c, The joint nonhyperbolic moveout inversion of PP and PS data in VTI media: Geophysics, **67**, 1929–1932.

Grechka, V., and Tsvankin, I., 2002d, Processing-induced anisotropy: Geophysics, **67**, 1920–1928.

Grechka, V., Tsvankin, I., Bakulin, A., Hansen, J.O., and Signer, C., 2002, Joint inversion of PP and PS reflection data for VTI media: A North Sea case study: Geophysics, **67**, 1920–1928.

Grechka, V., Tsvankin, I., and Cohen, J.K., 1999b, Generalized Dix equation and analytic treatment of normal-moveout velocity for anisotropic media: Geophys. Prosp., **47**, 117–148.

Gritsenko, E.A., 1984, Time field derivatives: Soviet Geology and Geophysics, **25**, 103–109.

Hake, H., Helbig, K., and Mesdag, C. S., 1984, Three-term Taylor series for $t^2 - x^2$ curves over layered transversely isotropic ground: Geophys. Prosp., **32**, 828–850.

Hubral, P., and Krey, T., 1980, Interval velocities from seismic reflection time measurements: SEG, Tulsa.

Isaac, J.H., and Lawton, D.C., 1999, Image mispositioning due to dipping TI media: A physical seismic modeling study: Geophysics, **64**, 1230–1238.

Leslie, J.M., and Lawton, D.C., 1996, Structural imaging below dipping anisotropic layers: predictions from seismic modeling: 66th Ann. Internat. Mtg., Soc. Expl. Geophys., Expanded Abstracts, 719–722.

Leslie, J.M., and Lawton, D.C., 1998, Anisotropic pre-stack depth migration: The Recorder, **XXIII**, N10, 23–36.

Le Stunff, Y., Grenié, D., 1998, Taking into account a priori information in 3D tomography: 68th Ann. Internat. Mtg., Soc. Expl. Geophys., Expanded Abstracts, 1875–1878.

Le Stunff, Y., Jeannot, J.P., 1998, Pre-stack anisotropic depth imaging: 60th EAGE Conference, Extended Abstracts.

Le Stunff, Y., Grechka, V., and Tsvankin, I., 2001, Depth-domain velocity analysis in VTI media using surface P-wave data: Is it feasible?: Geophysics, **66**, 897–903.

Muir, F., Dellinger, J., and Karrenbach, M., 1993, Anelliptic approximations for TI media: J. of Seismic Explor., **2**, 23–40.

Nolte, B., Bishop, K., and Sukup, D., 1999, Anisotropic prestack depth migration of converted-wave data from the Gulf of Mexico: 69th Ann. Internat. Mtg., Soc. Expl. Geophys., Expanded Abstracts, 691–694.

Peeters, M., Allen, D., Gomes, R., and Kristiansen, J., 1999, Invasion in space and time: 40th Ann. Symposium, Society of Professional Well Log Analysts, 479–485.

Pérez, M.A., Grechka, V., and Michelena, R.J., 1999, Fracture detection in a carbonate reservoir using a variety of seismic methods: Geophysics, **64**, 1266–1276.

Ryan-Grigor, S., 1998, Empirical relationships between anellipticity and V_P/V_S in shales: Potential applications to AVO studies and anisotropic seismic processing: 68th Ann. Internat. Mtg., Soc. Expl. Geophys., Expanded Abstracts, 208–211.

Sayers, C. M., and Ebrom, D. A., 1997, Seismic traveltime analysis for azimuthally anisotropic media: Theory and experiment: Geophysics, **36**, 1570–1582.

Scales, J. A., Smith, M. L., and Fischer, T. L., 1992, Global optimization methods for multimodal inverse problems: J. Comput. Phys., **102**, 258–268.

Schoenberg, M., and Helbig, K., 1997, Orthorhombic media: Modeling elastic wave behavior in a vertically fractured earth: Geophysics, **62**, 1954–1974.

Sexton, P., and Williamson, P., 1998, 3D anisotropic velocity estimation by model-based inversion of pre-stack traveltimes: 68th Ann. Internat. Mtg., Soc. Expl. Geophys., Expanded Abstracts, 1855–1858.

Taner, M. T., and Koehler, F., 1969, Velocity spectra – digital computer derivation and applications of velocity functions: Geophysics, **34**, 859–881.

Thomsen, L., 1986, Weak elastic anisotropy: Geophysics, **51**, 1954–1966.

Thomsen, L., 1999, Converted-wave reflection seismology over inhomogeneous, anisotropic media: Geophysics, **64**, 678–690.

Toldi, J., Alkhalifah, T., Berthet, P., Arnaud, J., Williamson, P., and Conche, B., 1999, Case study of estimation of anisotropy: The Leading Edge, **18**, no. 5, 588–594.

Tsvankin, I., 1995, Normal moveout from dipping reflectors in anisotropic media: Geophysics, **60**, 268–284.

Tsvankin, I., 1996, P-wave signatures and notation for transversely isotropic media: An overview: Geophysics, **61**, 467-483.

Tsvankin, I., 1997a, Moveout analysis for transversely isotropic media with a tilted symmetry axis: Geophys. Prosp., **45**, 479–512.

Tsvankin, I., 1997b, Reflection moveout and parameter estimation for horizontal transverse isotropy: Geophysics, **62**, 614–629.

Tsvankin, I., 1997c, Anisotropic parameters and P-wave velocity for orthorhombic media: Geophysics, **62**, 1292–1309.

Tsvankin, I., 2001, Seismic signatures and analysis of reflection data in anisotropic media: Elsevier Science.

Tsvankin, I., and Grechka, V., 2000, Dip moveout of converted waves and parameter estimation in transversely isotropic media: Geophys. Pros p., **48**, 257–292.

Tsvankin, I., and Grechka, V., 2002, 3D description and inversion of reflection moveout of PS-waves in anisotropic media: Geophys. Prosp., **50**, 301–316.

Tsvankin, I., and Thomsen, L., 1994, Nonhyperbolic reflection moveout in anisotropic media: Geophysics, **59**, 1290–1304.

Uren, N.F., Gardner, G.N.F., and McDonald, J.A., 1990, Normal moveout in anisotropic media: Geophysics, **55**, 1634–1636.

Vernik, L., and Liu, X., 1997, Velocity anisotropy in shales: A petrophysical study: Geophysics, **62**, 521–532.

Vestrum, R.W., Lawton, D.C., and Schmid, R., 1999, Imaging structures below dipping TI media: Geophysics, **64**, 1239–1246.

APPENDIX A

A.1 Derivation of the NMO velocity

The derivation is based on expanding the traveltime in a Taylor series in half-offset h near the CMP location ($h = 0$) (Grechka and Tsvankin, 1998b). The traveltime field is assumed to be smooth enough for all needed derivatives to exist at zero offset.

If the coordinate of the common midpoint O is denoted by $\mathbf{y}$ (Figure A.1), the coordinates of the source S and receiver R are $\mathbf{y} - \mathbf{x}$ and $\mathbf{y} + \mathbf{x}$, where

$$\mathbf{x} \equiv [x_1, x_2, x_3] = h\mathcal{L} \equiv h\,[\mathcal{L}_1, \mathcal{L}_2, \mathcal{L}_3]\,. \tag{A.1.1}$$

$\mathcal{L}$ corresponds to the unit vector parallel to the CMP line. The pure-mode two-way reflection traveltime t depends on the positions of the source and receiver and on the coordinate $\mathbf{r} = \mathbf{r}(\mathbf{y}, \mathbf{x})$ of the reflection point. Summing the one-way traveltimes τ corresponding to the downgoing and upgoing rays yields

$$t(\mathbf{y}, \mathbf{x}, \mathbf{r}) = \tau(\mathbf{y} - \mathbf{x}, \mathbf{r}) + \tau(\mathbf{y} + \mathbf{x}, \mathbf{r})\,. \tag{A.1.2}$$

Since reflection point dispersal (i.e., the deviation of $\mathbf{r}$ from $\mathbf{r}_0$ in Figure A.1 for $|\mathbf{x}| \neq 0$) does not change NMO velocity (e.g., Hubral and Krey, 1980; Goldin, 1986), we assume that nonzero-offset rays are reflected at point $\mathbf{r}_0$:

$$t(\mathbf{y}, \mathbf{x}, \mathbf{r}) = t(\mathbf{y}, \mathbf{x}, \mathbf{r}_0) = \tau(\mathbf{y} - \mathbf{x}, \mathbf{r}_0) + \tau(\mathbf{y} + \mathbf{x}, \mathbf{r}_0)\,.$$

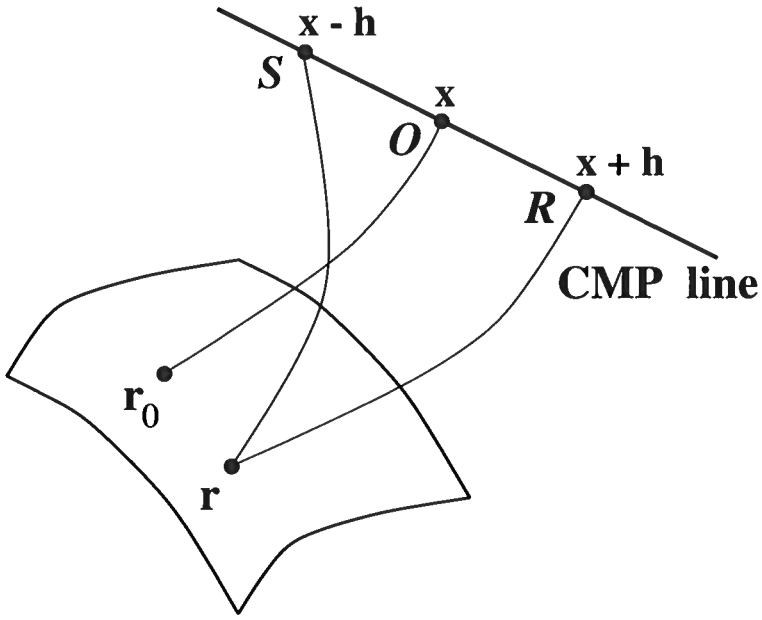

FIG. A.1. Reflected rays recorded on a common-midpoint line in 3-D space. $\mathbf{r}_0$ is the reflection point of the zero-offset ray originated at the CMP location O. The ray excited at S and emerging at R is reflected at a different point $\mathbf{r}$, but the reflection-point dispersal has no influence on NMO velocity.

Hence, for a given reflection event and a fixed CMP location (constant $\mathbf{y}$ and $\mathbf{r}_0$), t is a function of the one-way traveltime from the zero-offset reflection point:

$$t(\mathbf{x}) = \tau(-\mathbf{x}) + \tau(\mathbf{x})\,. \tag{A.1.3}$$

Taking into account equation (A.1.1), the first derivative of the traveltime with respect to the half-offset h is given by

$$\frac{dt}{dh} = \sum_{k=1}^{3} \frac{\partial t}{\partial x_k} \mathcal{L}_k\,. \tag{A.1.4}$$

Using equation (A.1.3), we find the derivative (A.1.4) at zero offset as

$$\frac{dt}{dh}\bigg|_{h=0} = \sum_{k=1}^{3} \left[-\frac{\partial \tau}{\partial x_k} + \frac{\partial \tau}{\partial x_k} \right] \mathcal{L}_k = 0\,. \tag{A.1.5}$$

Differentiating equation (A.1.4) again yields

$$\frac{d^2t}{dh^2} = \sum_{k,m=1}^{3} \frac{\partial^2 t}{\partial x_k\, \partial x_m}\, \mathcal{L}_k\, \mathcal{L}_m\,. \tag{A.1.6}$$

Therefore, at zero offset

$$\frac{d^2t}{dh^2}\bigg|_{|\mathbf{x}|=h=0} = \sum_{k,m=1}^{3} \frac{\partial^2 t}{\partial x_k\, \partial x_m}\bigg|_{h=0} \mathcal{L}_k\, \mathcal{L}_m = 2 \sum_{k,m=1}^{3} \frac{\partial^2 \tau}{\partial x_k\, \partial x_m}\bigg|_{h=0} \mathcal{L}_k\, \mathcal{L}_m\,, \tag{A.1.7}$$

To obtain the equation for NMO velocity along the CMP line $\mathcal{L}$, we expand the traveltime $t(h)$ in a Taylor series,

$$t(h, \mathcal{L}) = t_0 + \frac{dt}{dh}\bigg|_{h=0} h + \frac{d^2t}{dh^2}\bigg|_{h=0} \frac{h^2}{2} + \ldots\,, \tag{A.1.8}$$

where $t_0 = 2\tau_0$ is the two-way zero-offset traveltime. Substituting equations (A.1.5) and (A.1.7) into equation (A.1.8) leads to

$$t(h,\mathcal{L}) = t_0 + h^2 \sum_{k,m=1}^{3} \frac{\partial^2 \tau}{\partial x_k \, \partial x_m}\bigg|_{h=0} \mathcal{L}_k \, \mathcal{L}_m + \ldots \tag{A.1.9}$$

Squaring equation (A.1.9) and keeping quadratic and lower-order terms with respect to h yields

$$t^2(h,\mathcal{L}) = t_0^2 + 2\, t_0\, h^2 \sum_{k,m=1}^{3} \frac{\partial^2 \tau}{\partial x_k \, \partial x_m}\bigg|_{h=0} \mathcal{L}_k \, \mathcal{L}_m \,. \tag{A.1.10}$$

Introducing the source-receiver offset

$$X = 2\, h \,, \tag{A.1.11}$$

we rewrite equation (A.1.10) in its final form

$$t^2(X,\mathcal{L}) = t_0^2 + (\mathcal{L}\,\mathbf{U}\,\mathcal{L}^{\mathbf{T}})\, X^2 \,. \tag{A.1.12}$$

Here the superscript $\mathbf{T}$ denotes transposition; the 3×3 symmetric matrix $\mathbf{U}$ is defined as

$$U_{km} \equiv \tau_0 \, \frac{\partial^2 \tau}{\partial x_k \, \partial x_m}\bigg|_{h=0} = \tau_0 \, \frac{\partial p_k}{\partial x_m}\bigg|_{h=0} , \qquad (k,m = 1,2,3) \,, \tag{A.1.13}$$

and

$$p_k = \frac{\partial \tau}{\partial x_k} \,, \qquad (k = 1,2,3) \tag{A.1.14}$$

are the components of the slowness vector $\mathbf{p} = [p_1, p_2, p_3]$.

Comparing equation (A.1.12) with the conventional definition of the normal-moveout velocity $V_{\text{nmo}}(\mathcal{L})$ on the CMP line $\mathcal{L}$,

$$t^2(X, \mathcal{L}) = t_0^2 + \frac{X^2}{V_{\text{nmo}}^2(\mathcal{L})}\,, \tag{A.1.15}$$

we conclude that

$$\frac{1}{V_{\text{nmo}}^2(\mathcal{L})} = \mathcal{L}\,\mathbf{U}\,\mathcal{L}^{\mathbf{T}}\,. \tag{A.1.16}$$

APPENDIX B

B.1 Constructing the NMO surface from the NMO ellipse

Let us assume that the NMO ellipse (matrix $\mathbf{W}$) in the $[x_1, x_2]$-plane has been constructed from three or more moveout-velocity measurements in different azimuthal directions. To build the NMO-velocity surface $\mathbf{U}$ from $\mathbf{W}$, we need to obtain the matrix elements U_{k3}. This can be done by using the Christoffel equation,

$$F(\mathbf{p}, \mathbf{x}) = 0\,, \tag{B.1.1}$$

where $\mathbf{p} = \mathbf{p}(\mathbf{x})$ is the slowness vector of rays generated at the zero-offset reflection point, and F explicitly depends on the spatial coordinates $\mathbf{x}$ because in heterogeneous media the elastic stiffness coefficients c_{ij} vary in space.

Differentiating equation (B.1.1) with respect to x_1 and x_2 yields

$$\sum_{k=1}^{3} F_{p_k} \frac{\partial p_k}{\partial x_j} + F_{x_j} = 0\,, \qquad (j = 1, 2)\,, \tag{B.1.2}$$

where $F_{p_k} \equiv \partial F / \partial p_k$ and $F_{x_j} \equiv \partial F / \partial x_j$. The partial derivatives of the horizontal slowness components and the zero-offset traveltime τ_0 define the NMO ellipse $\mathbf{W}$:

$$\frac{\partial p_i}{\partial x_j} = \frac{W_{ij}}{\tau_0}\,, \qquad (i, j = 1, 2)\,. \tag{B.1.3}$$

Substituting equation (B.1.3) into equation (B.1.2) and solving for $\partial p_3 / \partial x_j$, we find

$$U_{j3} \equiv \tau_0 \frac{\partial p_3}{\partial x_j} = -\frac{F_{p_1} W_{1j} + F_{p_2} W_{2j} + \tau_0 F_{x_j}}{F_{p_3}}, \qquad (j = 1, 2). \tag{B.1.4}$$

Differentiating the Christoffel equation (B.1.1) with respect to x_3 and taking into account that $\partial p_j / \partial x_3 = \partial p_3 / \partial x_j$ (because of the symmetry of $\mathbf{U}$) leads to the following expression for U_{33}:

$$U_{33} \equiv \tau_0 \frac{\partial p_3}{\partial x_3} = -\frac{F_{p_1} U_{13} + F_{p_2} U_{23} + \tau_0 F_{x_3}}{F_{p_3}}. \tag{B.1.5}$$

At a fixed spatial location $\mathbf{x}$, the Christoffel equation can be treated as a relationship between the vertical slowness component $p_3 \equiv q$ and the horizontal slownesses p_1 and p_2. Implicit differentiation of the Christoffel equation then gives (Grechka et al., 1999b)

$$q_{,j} = -\frac{F_{p_j}}{F_q}, \qquad (j = 1, 2), \tag{B.1.6}$$

where $q_{,j} \equiv \partial q / \partial p_j \equiv \partial p_3 / \partial p_j$ and $F_q \equiv \partial F / \partial q \equiv \partial F / \partial p_3$. Using equation (B.1.6), we rewrite equations (B.1.4) and (B.1.5) in the form

$$U_{j3} = q_{,1} W_{1j} + q_{,2} W_{2j} - \tau_0 \frac{F_{x_j}}{F_q}, \qquad (j = 1, 2) \tag{B.1.7}$$

and

$$U_{33} = q_{,1} U_{13} + q_{,2} U_{23} - \tau_0 \frac{F_{x_3}}{F_q}. \tag{B.1.8}$$

Substituting equation (B.1.7) into (B.1.8), we obtain the final expression for U_{33} and the NMO-velocity surface as a whole:

$$\mathbf{U} = \begin{pmatrix} W_{11} & W_{12} & q_{,1}W_{11} + q_{,2}W_{12} - \tau_0 F_{x_1}/F_q \\ \bullet & W_{22} & q_{,1}W_{12} + q_{,2}W_{22} - \tau_0 F_{x_2}/F_q \\ \bullet & \bullet & q_{,1}^2 W_{11} + 2q_{,1}q_{,2}W_{12} + q_{,2}^2 W_{22} - \tau_0 \left(q_{,1}F_{x_1} + q_{,2}F_{x_2} + F_{x_3}\right)/F_q \end{pmatrix}, \quad \text{(B.1.9)}$$

where bullets in the lower triangle of the matrix denote the elements $U_{21} = U_{12}$, $U_{31} = U_{13}$, and $U_{32} = U_{23}$.

APPENDIX C

C.1 Dix-type averaging in heterogeneous anisotropic media

Here we give a detailed description of the Dix-type procedure for building the NMO-velocity surfaces in heterogeneous anisotropic media. Suppose we would like to use a known surface $\mathbf{U}(\tau_0)$ at the zero-offset traveltime τ_0 to construct the surface $\mathbf{U}(\tau_0 + \Delta\tau_0)$ at the time $\tau_0 + \Delta\tau_0$, where $\Delta\tau_0$ is an infinitesimal interval. We assume that the projection of the slowness vector $\mathbf{p}(\tau_0)$ onto the plane $\mathcal{P}(\tau_0) \perp d\mathbf{p}/d\tau_0$ is locally preserved over the ray segment corresponding to $\Delta\tau_0$ (Figure C.1). Given the intersection of the NMO-velocity surface $\mathbf{U}(\tau_0)$ with the plane $\mathcal{P}(\tau_0)$,

$$\mathbf{W}^{\mathcal{P}(\tau_0)}(\tau_0) = \mathbf{U}(\tau_0) \bigcap \mathcal{P}(\tau_0)\,,$$

the intersection at the time $\tau_0 + \Delta\tau_0$ is given by the Dix-type equation

$$\left[\mathbf{W}^{\mathcal{P}(\tau_0)}(\tau_0 + \Delta\tau_0)\right]^{-1} = \frac{\tau_0 \left[\mathbf{W}^{\mathcal{P}(\tau_0)}(\tau_0)\right]^{-1} + \Delta\tau_0 \left[\mathbf{W}^{\mathcal{P}(\tau_0)}|_{[\tau_0,\, \tau_0+\Delta\tau_0]}\right]^{-1}}{\tau_0 + \Delta\tau_0}\,. \qquad \text{(C.1.1)}$$

Here

$$\mathbf{W}^{\mathcal{P}(\tau_0)}|_{[\tau_0,\, \tau_0+\Delta\tau_0]} = \mathbf{U}|_{[\tau_0,\, \tau_0+\Delta\tau_0]} \bigcap \mathcal{P}(\tau_0)$$

is the intersection of the *local* NMO-velocity surface $\mathbf{U}|_{[\tau_0,\, \tau_0+\Delta\tau_0]}$ with the plane $\mathcal{P}(\tau_0)$.

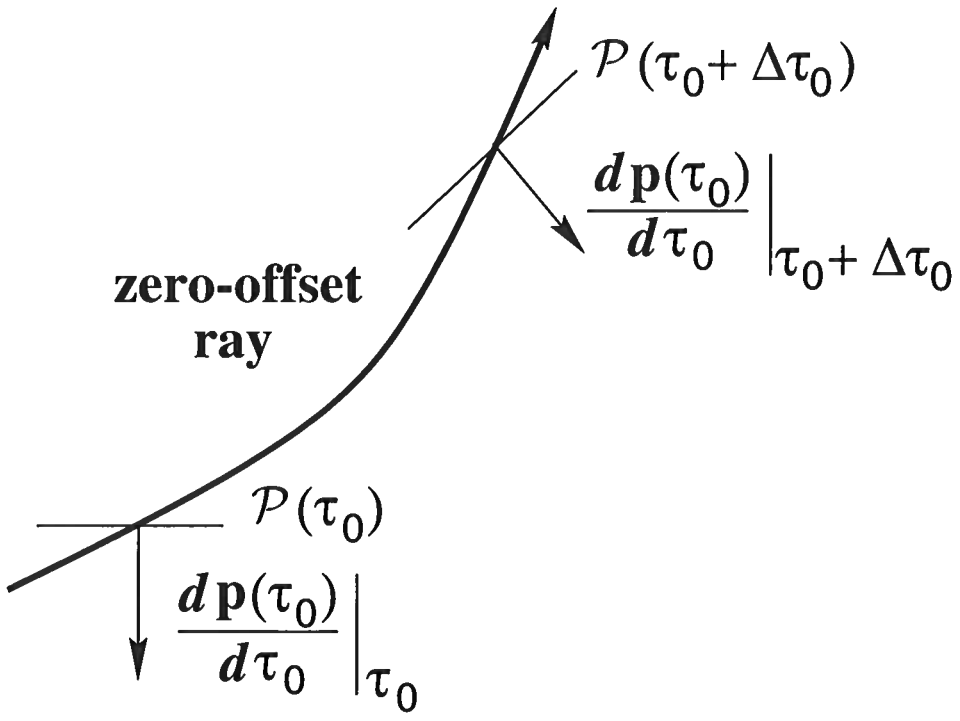

FIG. C.1. The projection of the slowness vector $\mathbf{p}(\tau_0)$ onto the plane $\mathcal{P}(\tau_0) \perp d\mathbf{p}/d\tau_0$ is locally preserved even if the medium is inhomogeneous and anisotropic.

The plane $\mathcal{P}(\tau_0 + \Delta\tau_0) \perp d\mathbf{p}/d\tau_0|_{\tau_0+\Delta\tau_0}$ at traveltime $\tau_0 + \Delta\tau_0$ generally differs from the plane $\mathcal{P}(\tau_0)$, as shown in Figure C.1. In order to account for the rotation of the plane $\mathcal{P}$ along the ray, we reconstruct the NMO surface $\mathbf{U}(\tau_0 + \Delta\tau_0)$ from its cross-section $\mathbf{W}^{\mathcal{P}(\tau_0)}(\tau_0 + \Delta\tau_0)$ using equations (D.1.9) and (D.1.12) (see Appendix D) and find the intersection of $\mathbf{U}(\tau_0 + \Delta\tau_0)$ with the plane $\mathcal{P}(\tau_0 + \Delta\tau_0)$:

$$\mathbf{W}^{\mathcal{P}(\tau_0+\Delta\tau_0)}(\tau_0 + \Delta\tau_0) = \mathbf{U}(\tau_0 + \Delta\tau_0) \bigcap \mathcal{P}(\tau_0 + \Delta\tau_0)\,.$$

Since the slowness components are locally preserved in the plane $\mathcal{P}(\tau_0 + \Delta\tau_0)$, we can continue the cross-section $\mathbf{W}^{\mathcal{P}(\tau_0+\Delta\tau_0)}(\tau_0 + \Delta\tau_0)$ along the next ray segment using equation (C.1.1) applied to the time interval $[\tau_0 + \Delta\tau_0,\ \tau_0 + 2\Delta\tau_0]$.

In summary, continuation of the NMO-velocity surface along the zero-offset ray involves the following steps:

Step 1. Construct the intersection $\mathbf{W}^{\mathcal{P}(\tau_0)}(\tau_0)$ [equation (D.1.7)] of the given NMO-velocity surface $\mathbf{U}(\tau_0)$ with the plane $\mathcal{P}(\tau_0)$ orthogonal to the vector $d\mathbf{p}/d\tau_0$.

Step 2. Continue the cross-section of the NMO-velocity surface over the time interval $\Delta\tau_0$; that is, compute $\mathbf{W}^{\mathcal{P}(\tau_0)}(\tau_0+\Delta\tau_0)$ from $\mathbf{W}^{\mathcal{P}(\tau_0)}(\tau_0)$ using equation (C.1.1).

Step 3. Reconstruct the surface $\mathbf{U}(\tau_0+\Delta\tau_0)$ [equations (D.1.9) and (D.1.12)] from its cross-section $\mathbf{W}^{\mathcal{P}(\tau_0)}(\tau_0+\Delta\tau_0)$.

Step 4. Repeat **Step 1** for the surface $\mathbf{U}(\tau_0+\Delta\tau_0)$.

APPENDIX D

D.1 Operations with cross-sections of NMO-velocity surfaces

In this appendix, we show how to compute the intersection $\mathbf{W}^{\mathcal{P}}$ of the NMO-velocity surface $\mathbf{U}$ with an arbitrary plane $\mathcal{P}$ and reconstruct the matrix $\mathbf{U}$ from its given cross-section $\mathbf{W}^{\mathcal{P}}$. Let us denote by $\mathbf{z}$ the unit vector in the direction $d\mathbf{p}/d\tau_0$ normal to the plane $\mathcal{P}$. The vector $\mathbf{z}$ can be specified by two spherical angles ϕ_1 and ϕ_2:

$$\mathbf{z} = [\sin\phi_1 \cos\phi_2,\ \sin\phi_1 \sin\phi_2,\ \cos\phi_1]\,. \tag{D.1.1}$$

It is straightforward to verify that the unit vectors

$$\mathbf{b}^{(1)} = [\cos\phi_1 \cos\phi_2,\ \cos\phi_1 \sin\phi_2,\ -\sin\phi_1] \tag{D.1.2}$$

and

$$\mathbf{b}^{(2)} = [-\sin\phi_2,\ \cos\phi_2,\ 0] \tag{D.1.3}$$

are both orthogonal to $\mathbf{z}$ and, therefore, lie in the plane $\mathcal{P} \perp \mathbf{z}$. Thus, any vector $\mathbf{b}$ in $\mathcal{P}$ is given by

$$\mathbf{b} = \mathbf{b}^{(1)} \cos\alpha + \mathbf{b}^{(2)} \sin\alpha\,, \tag{D.1.4}$$

where α is the azimuth (within $\mathcal{P}$) with respect to $\mathbf{b}^{(1)}$.

The NMO velocity within the plane $\mathcal{P}$,

$$\frac{1}{V_{\mathrm{nmo}}^2(\mathbf{b})} = \mathbf{b}\,\mathbf{U}\,\mathbf{b}^{\mathbf{T}}\,, \tag{D.1.5}$$

can be viewed as the intersection of the NMO surface $\mathbf{U}$ with the plane $\mathcal{P}$. Substituting equations (D.1.2) – (D.1.4) into (D.1.5) yields

$$\left.\frac{1}{V_{\mathrm{nmo}}^2(\alpha)}\right|_{\mathcal{P}} = W_{11}^{\mathcal{P}}\cos^2\alpha + 2\,W_{12}^{\mathcal{P}}\sin\alpha\cos\alpha + W_{22}^{\mathcal{P}}\sin^2\alpha\,, \tag{D.1.6}$$

where

$$W_{ij}^{\mathcal{P}} = \sum_{k,m=1}^{3} B_{km,ij}\,U_{km}\,, \qquad (i,j=1,2)\,, \tag{D.1.7}$$

and

$$B_{km,ij} = \frac{1}{2}\left(b_k^{(i)}b_m^{(j)} + b_k^{(j)}b_m^{(i)}\right)\,, \qquad (i,j=1,2;\quad k,m=1,2,3)\,. \tag{D.1.8}$$

Equations (D.1.1) – (D.1.3), (D.1.7), and (D.1.8) define the matrix $\mathbf{W}^{\mathcal{P}}$ that describes the intersection (i.e., the NMO ellipse) of the NMO surface $\mathbf{U}$ with the plane $\mathcal{P}$ having the unit normal $\mathbf{z}$.

Next, we show how to reconstruct the whole NMO surface $\mathbf{U}$ from its cross-section $\mathbf{W}^{\mathcal{P}}$. This procedure is based on equation (B.1.9), which can be written in the form

$$\mathbf{U} = \begin{pmatrix} W_{11} & W_{12} & q_{,1}W_{11} + q_{,2}W_{12} + A_1 \\ \bullet & W_{22} & q_{,1}W_{12} + q_{,2}W_{22} + A_2 \\ \bullet & \bullet & q_{,1}^2W_{11} + 2q_{,1}q_{,2}W_{12} + q_{,2}^2W_{22} + A_3 \end{pmatrix}, \tag{D.1.9}$$

where $\mathbf{W}$ is the NMO ellipse in the horizontal plane $[x_1, x_2]$, and the quantities A_i are given by

$$A_i = -\tau_0 \frac{F_{x_i}}{F_q}, \qquad (i = 1, 2),$$

$$A_3 = -\tau_0 \frac{q_{,1}F_{x_1} + q_{,2}F_{x_2} + F_{x_3}}{F_q}.$$

The derivatives of F [equation (B.1.1)], which also determine the derivatives $q_{,i}$ and $q_{,ij}$ of the vertical slowness component with respect to the horizontal slownesses are evaluated at point $\mathbf{x}$ of the zero-offset ray specified by the one-way traveltime τ_0.

From equation (D.1.9) it is clear that in order to compute $\mathbf{U}$ we need to know the matrix $\mathbf{W}$ because all other quantities are obtained by differentiating the Christoffel equation (B.1.1). Substituting equation (D.1.9) into (D.1.7) leads to three linear equations relating the matrices $\mathbf{W}$ and $\mathbf{W}^{\mathcal{P}}$:

$$W^{\mathcal{P}}_{ij} = C_{ij} + \sum_{i',j'=1}^{2} D_{i'j',ij} W_{i'j'}, \qquad (i, j = 1, 2). \tag{D.1.10}$$

Here

$$C_{ij} = 2A_1 B_{13,ij} + 2A_2 B_{23,ij} + A_3 B_{33,ij}$$

and

$$D_{i'j',ij} = B_{i'j',ij} + q_{,i'} B_{j'3,ij} + q_{,j'} B_{i'3,ij} + q_{,i'} q_{,j'} B_{33,ij}, \qquad (i', j', i, j = 1, 2).$$

To emphasize the fact that equations (D.1.10) represent a system of linear equations for the unknown elements $W_{i'j'}$, we replace the pairs of indices $\{ij\}$ and $\{i'j'\}$ by a

single index using the following convention: $\{11\} \to 1$, $\{12\} \to 2$, and $\{22\} \to 3$. Then, equations (D.1.10) can be rewritten in a more conventional form,

$$\sum_{k'=1}^{3} E_{k'k}\, W_{k'} = C_k - W_k^{\mathcal{P}}\,, \qquad (k = 1, 2, 3)\,. \tag{D.1.11}$$

where $E_{k'k}$ are the elements of the 3×3 matrix

$$\mathbf{E} = \begin{pmatrix} D_{11,11} & 2\,D_{12,11} & D_{22,11} \\ D_{11,12} & 2\,D_{12,12} & D_{22,12} \\ D_{11,22} & 2\,D_{12,22} & D_{22,22} \end{pmatrix}.$$

The linear system (D.1.11) can be solved for the matrix $\mathbf{W}$ using standard techniques:

$$\mathbf{W} = \mathbf{E}^{-1}\left(\mathbf{W}^{\mathcal{P}} - \mathbf{C}\right). \tag{D.1.12}$$

Thus, equations (D.1.9) and (D.1.12), supplemented with the Christoffel equation (B.1.1), make it possible to reconstruct the NMO-velocity surface $\mathbf{U}$ from its intersection $\mathbf{W}^{\mathcal{P}}$ with the plane $\mathcal{P}$.

APPENDIX E

E.1 NMO velocity along a curved CMP line

Here the derivation of the NMO velocity measured along a *straight* arbitrarily oriented CMP line given by Grechka and Tsvankin (2002a) is extended to CMP lines with nonzero curvature at the common midpoint. This new derivation is based on expanding the pure-mode reflection traveltime t in a Taylor series in half offset h ($h = 0$ at the CMP location). The traveltime is assumed to be smooth enough for all needed derivatives to exist at zero offset.

Let us denote $\mathbf{x}_{\text{CMP}} = \boldsymbol{\sigma}(0)$ the coordinate of the common midpoint O (Figure E.1) on the irregular CMP line $\boldsymbol{\sigma}$. If the CMP line is parametrized as a function of its arclength h, the coordinates of the source S and receiver R become $\boldsymbol{\sigma}(-h)$ and $\boldsymbol{\sigma}(h)$. Using the small-offset approximation of the reflection traveltime, the function $\boldsymbol{\sigma}(h)$ can be replaced by its quadratic Taylor series expansion in the vicinity of $h = 0$:

$$\boldsymbol{\sigma}(h) = \mathbf{x}_{\text{CMP}} + \mathcal{L}\, h + \frac{1}{2}\mathcal{K}\, h^2 + o(h^2)\,. \tag{E.1.1}$$

Here $\mathcal{L}$ is the unit vector tangent to the CMP line at $h = 0$,

$$\mathcal{L} \equiv \left.\frac{d\boldsymbol{\sigma}}{dh}\right|_{h=0}, \tag{E.1.2}$$

and $\mathcal{K}$ is related to the curvature of the CMP line,

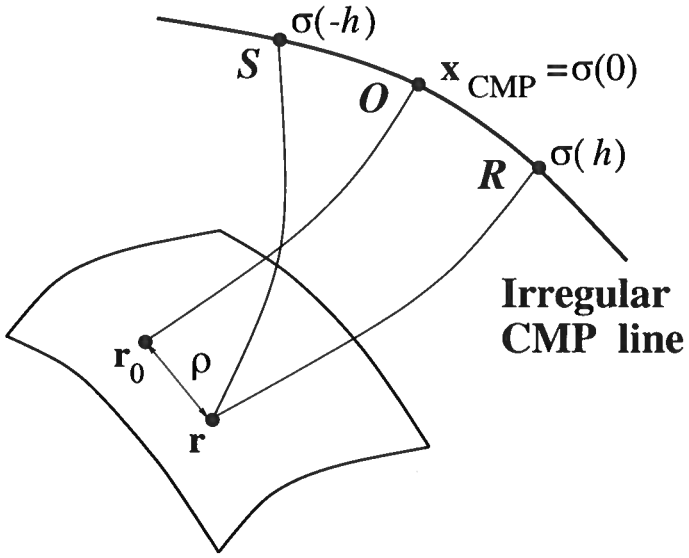

FIG. E.1. Reflection traveltimes are recorded along the curved CMP line $\boldsymbol{\sigma}$ with the common midpoint at O. Note the difference between the reflection points $\mathbf{r}_0$ and $\mathbf{r}$ of the zero-offset and nonzero-offset rays.

$$\mathcal{K} \equiv \left.\frac{d^2\boldsymbol{\sigma}}{dh^2}\right|_{h=0} . \tag{E.1.3}$$

The pure-mode two-way reflection traveltime t measured at small offsets h along the CMP line $\boldsymbol{\sigma}$ can be expanded in a similar quadratic Taylor series,

$$t\big(\boldsymbol{\sigma}(h),\mathbf{r}\big) = t\big(\boldsymbol{\sigma}(0),\mathbf{r}\big) + \left.\frac{dt\big(\boldsymbol{\sigma}(h),\mathbf{r}\big)}{dh}\right|_{h=0} h + \frac{1}{2}\left.\frac{d^2t\big(\boldsymbol{\sigma}(h),\mathbf{r}\big)}{dh^2}\right|_{h=0} h^2 + \ldots \tag{E.1.4}$$

The traveltime t depends on the source and receiver positions and on the coordinate $\mathbf{r}$ of the reflection point. Summing up the one-way traveltimes τ corresponding to the down- and upgoing rays, we can write

$$t\big(\boldsymbol{\sigma}(h),\mathbf{r}\big) = \tau\big(\boldsymbol{\sigma}(-h),\mathbf{r}\big) + \tau\big(\boldsymbol{\sigma}(h),\mathbf{r}\big) . \tag{E.1.5}$$

Let us begin with showing (following the derivation of Tsvankin and Grechka, 2000)

that the reflection point dispersal (i.e., the deviation of $\mathbf{r}$ from the zero-offset reflection point $\mathbf{r}_0$ in Figure E.1) has no influence on the values of the derivatives dt/dh and d^2t/dh^2 at $h = 0$, so equation (E.1.5) can be replaced with

$$t\big(\boldsymbol{\sigma}(h), \mathbf{r}\big) = t\big(\boldsymbol{\sigma}(h), \mathbf{r}_0\big) = \tau\big(\boldsymbol{\sigma}(-h), \mathbf{r}_0\big) + \tau\big(\boldsymbol{\sigma}(h), \mathbf{r}_0\big)\,. \tag{E.1.6}$$

Let us examine the difference

$$\Delta t \equiv t\big(\boldsymbol{\sigma}(h), \mathbf{r}\big) - t\big(\boldsymbol{\sigma}(h), \mathbf{r}_0\big)\,\Big|_{\text{fixed } \boldsymbol{\sigma} \text{ and } h} \tag{E.1.7}$$

between the traveltimes corresponding to the specular reflection point $\mathbf{r}$ and to the zero-offset (non-specular) reflection point $\mathbf{r}_0$. The source and receiver are located along the CMP line $\boldsymbol{\sigma}$ at the fixed half-offset h. The difference Δt can be expanded in a Taylor series in the distance $\rho = |\mathbf{r} - \mathbf{r}_0|$ between the points $\mathbf{r}$ and $\mathbf{r}_0$ (Figure E.1). At zero-offset, $\mathbf{r} = \mathbf{r}_0$ and $\Delta t|_{\rho=0} = 0$ as follows from equation (E.1.7). Since the traveltime has an extremum at the specular reflection point $\mathbf{r}$ (Fermat's principle), the series $\Delta t(\rho)$ starts with the quadratic term

$$\Delta t(\rho) = \frac{1}{2}\, A\big(\boldsymbol{\sigma}(h)\big)\, \rho^2\big(\boldsymbol{\sigma}(h)\big) + o(\rho^2)\,, \tag{E.1.8}$$

where

$$A\big(\boldsymbol{\sigma}(h)\big) = -\frac{d^2t\big(\boldsymbol{\sigma}(h), \mathbf{r}\big)}{d\rho^2}\bigg|_{\mathbf{r}}\,. \tag{E.1.9}$$

Differentiating equation (E.1.8) with respect to h yields

$$\frac{d\Delta t}{dh} = \frac{dA\big(\boldsymbol{\sigma}(h)\big)}{dh}\, \rho^2\big(\boldsymbol{\sigma}(h)\big) + 2\, A\big(\boldsymbol{\sigma}(h)\big)\, \rho\big(\boldsymbol{\sigma}(h)\big)\, \frac{d\rho\big(\boldsymbol{\sigma}(h)\big)}{dh}\,. \tag{E.1.10}$$

Since $\rho = 0$ at $h = 0$, the derivative

$$\left.\frac{d\Delta t}{dh}\right|_{h=0} = 0\,. \tag{E.1.11}$$

Therefore,

$$\left.\frac{dt\big(\boldsymbol{\sigma}(h),\mathbf{r}\big)}{dh}\right|_{h=0} = \left.\frac{dt\big(\boldsymbol{\sigma}(h),\mathbf{r}_0\big)}{dh}\right|_{h=0}\,. \tag{E.1.12}$$

Next, let us differentiate equation (E.1.10) again:

$$\begin{aligned}\frac{d^2\Delta t}{dh^2} &= \frac{d^2A\big(\boldsymbol{\sigma}(h)\big)}{dh^2}\,\rho^2\big(\boldsymbol{\sigma}(h)\big) + 4\,\frac{dA\big(\boldsymbol{\sigma}(h)\big)}{dh}\,\rho\big(\boldsymbol{\sigma}(h)\big)\,\frac{d\rho\big(\boldsymbol{\sigma}(h)\big)}{dh} \\ &\quad +2\,A\big(\boldsymbol{\sigma}(h)\big)\left[\frac{d\rho\big(\boldsymbol{\sigma}(h)\big)}{dh}\right]^2 + 2\,A\big(\boldsymbol{\sigma}(h)\big)\,\rho\big(\boldsymbol{\sigma}(h)\big)\,\frac{d^2\rho\big(\boldsymbol{\sigma}(h)\big)}{dh^2}\,.\end{aligned} \tag{E.1.13}$$

Evaluating the derivative (E.1.13) at $h = \rho = 0$, we obtain

$$\left.\frac{d^2\Delta t}{dh^2}\right|_{h=0} = 2\,A\big(\boldsymbol{\sigma}(h)\big)\left.\left[\frac{d\rho\big(\boldsymbol{\sigma}(h)\big)}{dh}\right]^2\right|_{h=0}\,. \tag{E.1.14}$$

To show that the derivative (E.1.14) is zero, one notes that both the traveltime and the ray trajectory of a pure reflection mode remain the same if one interchanges the source and receiver positions (the reciprocity principle). Hence,

$$\mathbf{r}\big(\boldsymbol{\sigma}(h)\big) = \mathbf{r}\big(\boldsymbol{\sigma}(-h)\big) \tag{E.1.15}$$

and, therefore,

$$\rho\big(\boldsymbol{\sigma}(h)\big) \equiv \Big|\mathbf{r}\big(\boldsymbol{\sigma}(h)\big) - \mathbf{r}_0\Big| = \Big|\mathbf{r}\big(\boldsymbol{\sigma}(-h)\big) - \mathbf{r}_0\Big| = \rho\big(\boldsymbol{\sigma}(-h)\big)\,, \tag{E.1.16}$$

i.e., ρ is an even function of h for any fixed CMP line $\boldsymbol{\sigma}$. Consequently,

$$\left.\frac{d\rho\big(\boldsymbol{\sigma}(h)\big)}{dh}\right|_{h=0} = 0\,, \tag{E.1.17}$$

so equation (E.1.14) results in

$$\left.\frac{d^2\Delta t}{dh^2}\right|_{h=0} = 0\,. \tag{E.1.18}$$

Thus

$$\left.\frac{d^2t\big(\boldsymbol{\sigma}(h),\mathbf{r}\big)}{dh^2}\right|_{h=0} = \left.\frac{d^2t\big(\boldsymbol{\sigma}(h),\mathbf{r}_0\big)}{dh^2}\right|_{h=0}\,, \tag{E.1.19}$$

and the derivatives in the series (E.1.4) can be obtained by differentiating equation (E.1.6). This result is equivalent to the normal incidence point (NIP) theorem proved by Chernyak and Gritsenko (1979) (their proof can also be found in Goldin, 1986) and by Hubral and Krey (1980).

The zero-offset ($h = 0$) traveltime can be expressed as [see equation (E.1.6)]

$$t\big(\boldsymbol{\sigma}(h),\mathbf{r}_0\big)\big|_{h=0} \equiv t_0 = 2\,\tau(\mathbf{x}_{\text{CMP}}). \tag{E.1.20}$$

Differentiating equation (E.1.6) and taking into account equation (E.1.1), one finds

$$\left.\frac{dt\big(\boldsymbol{\sigma}(h)\big)}{dh}\right|_{h=0} = \sum_{k=1}^{3}\frac{\partial\tau}{\partial\sigma_k}\Big(-\mathcal{L}_k + \mathcal{L}_k + 2\,\mathcal{K}_k\,h + o(h)\Big)\Big|_{h=0} = 0\,. \tag{E.1.21}$$

Differentiating the one-way traveltime with respect to h twice yields

$$\frac{d^2\tau\big(\boldsymbol{\sigma}(h)\big)}{dh^2} = \sum_{k,m=1}^{3}\frac{\partial^2\tau\big(\boldsymbol{\sigma}(h)\big)}{\partial\sigma_k\,\partial\sigma_m}\,\frac{d\sigma_k}{dh}\,\frac{d\sigma_m}{dh} + \sum_{k=1}^{3}\frac{\partial\tau\big(\boldsymbol{\sigma}(h)\big)}{\partial\sigma_k}\,\frac{d^2\sigma_k}{dh^2}\,. \tag{E.1.22}$$

Using equations (E.1.1), (E.1.6) and (E.1.22) leads to

$$\left.\frac{d^2t\big(\boldsymbol{\sigma}(h)\big)}{dh^2}\right|_{h=0} = 2\sum_{k,m=1}^{3}\left.\frac{\partial^2\tau\big(\boldsymbol{\sigma}(h)\big)}{\partial\sigma_k\,\partial\sigma_m}\right|_{h=0}\mathcal{L}_k\,\mathcal{L}_m + 2\sum_{k=1}^{3}\left.\frac{\partial\tau\big(\boldsymbol{\sigma}(h)\big)}{\partial\sigma_k}\right|_{h=0}\mathcal{K}_k\,. \qquad \text{(E.1.23)}$$

Noting that

$$\left.\frac{\partial}{\partial\sigma_k}\right|_{h=0} = \left.\frac{\partial}{\partial x_k}\right|_{h=0} \qquad \text{(E.1.24)}$$

equation (E.1.23) can be rewritten in the following form:

$$\left.\frac{d^2t\big(\boldsymbol{\sigma}(h)\big)}{dh^2}\right|_{h=0} = 2\sum_{k,m=1}^{3}\left.\frac{\partial^2\tau(\mathbf{x})}{\partial x_k\,\partial x_m}\right|_{h=0}\mathcal{L}_k\,\mathcal{L}_m + 2\sum_{k=1}^{3}\left.\frac{\partial\tau(\mathbf{x})}{\partial x_k}\right|_{h=0}\mathcal{K}_k\,. \qquad \text{(E.1.25)}$$

Equation (E.1.25) relates the second-order derivative of the two-way traveltime t with respect to the half-offset and the second-order spatial derivatives of the one-way traveltime τ from the zero-offset reflection point.

To obtain an equation for the NMO velocity along the CMP line $\boldsymbol{\sigma}$, let us substitute the derivatives (E.1.21) and (E.1.25) into the series (E.1.4):

$$t\big(\boldsymbol{\sigma}(h)\big) = t_0 + h^2\left\{\sum_{k,m=1}^{3}\left.\frac{\partial^2\tau(\mathbf{x})}{\partial x_k\,\partial x_m}\right|_{h=0}\mathcal{L}_k\,\mathcal{L}_m + \sum_{k=1}^{3}\left.\frac{\partial\tau(\mathbf{x})}{\partial x_k}\right|_{h=0}\mathcal{K}_k\right\}. \qquad \text{(E.1.26)}$$

Squaring this equation and keeping the quadratic and lower-order terms with respect to h yields

$$t^2\big(\boldsymbol{\sigma}(h)\big) = t_0^2 + 2\,t_0\,h^2\left\{\sum_{k,m=1}^{3}\left.\frac{\partial^2\tau(\mathbf{x})}{\partial x_k\,\partial x_m}\right|_{h=0}\mathcal{L}_k\,\mathcal{L}_m + \sum_{k=1}^{3}\left.\frac{\partial\tau(\mathbf{x})}{\partial x_k}\right|_{h=0}\mathcal{K}_k\right\}. \qquad \text{(E.1.27)}$$

Introducing the source-receiver offset

$$X = 2\,h\,, \tag{E.1.28}$$

one can rewrite equation (E.1.27) in its final form,

$$t^2\Big(\boldsymbol{\sigma}(X)\Big) = t_0^2 + (\mathcal{L}\,\mathbf{U}\,\mathcal{L}^{\mathbf{T}} + \tau_0\,\mathbf{p}\cdot\mathcal{K})\,X^2\,, \tag{E.1.29}$$

where $\tau_0 = t_0/2$ is the one-way zero-offset traveltime. Here $\mathbf{T}$ denotes transposition, and the 3×3 symmetric matrix $\mathbf{U}$ is defined as

$$U_{km} \equiv \tau_0 \left.\frac{\partial^2\tau(\mathbf{x})}{\partial x_k\,\partial x_m}\right|_{h=0} = \tau_0 \left.\frac{\partial p_k(\mathbf{x})}{\partial x_m}\right|_{h=0}, \qquad (k,m=1,2,3)\,; \tag{E.1.30}$$

$$p_k(\mathbf{x}) \equiv \frac{\partial\tau(\mathbf{x})}{\partial x_k}\,, \qquad (k,m=1,2,3), \tag{E.1.31}$$

are the components of the slowness vector $\mathbf{p} = [p_1, p_2, p_3]$. In equation (E.1.29) $\mathbf{p}$ is evaluated at the CMP location.

Comparing equation (E.1.29) with the conventional definition of the NMO velocity $V_{\rm nmo}(\boldsymbol{\sigma})$ along the CMP line $\boldsymbol{\sigma}$,

$$t^2\Big(\boldsymbol{\sigma}(X)\Big) = t_0^2 + \frac{X^2}{V_{\rm nmo}^2(\boldsymbol{\sigma})}\,, \tag{E.1.32}$$

we conclude that

$$V_{\rm nmo}^{-2}(\boldsymbol{\sigma}) = \mathcal{L}\,\mathbf{U}\,\mathcal{L}^{\mathbf{T}} + \tau_0\,\mathbf{p}\cdot\mathcal{K}\,. \tag{E.1.33}$$

APPENDIX F

F.1 NMO velocity at an irregular surface

Equation (E.1.33) can be used to describe the azimuthal variation of the NMO velocity measured along CMP lines at an irregular surface **s**. Let us specify the surface

$$\mathbf{s} \equiv \mathbf{s}(h_1, h_2) \tag{F.1.1}$$

by a pair of curvilinear orthogonal coordinates h_1 and h_2 (Figure F.1) in such a way that the half-offset h along the CMP line $\boldsymbol{\sigma}$ is given as (for $h \to 0$)

$$h_1 = h \cos\alpha \tag{F.1.2}$$

and

$$h_2 = h \sin\alpha\,, \tag{F.1.3}$$

where α is the azimuth of the tangent to the CMP line at the common midpoint $\mathbf{x}_{\text{CMP}}$ with respect to the axis h_1 (Figure F.1).

For simplicity, the axis x_3 of the coordinate frame is directed along the normal **n** to the surface $\mathbf{s}(h_1, h_2)$ at the CMP location. This implies that the tangent vector $\mathcal{L}$ to the CMP line at $\mathbf{x}_{\text{CMP}}$ [see equation (E.1.2)] is

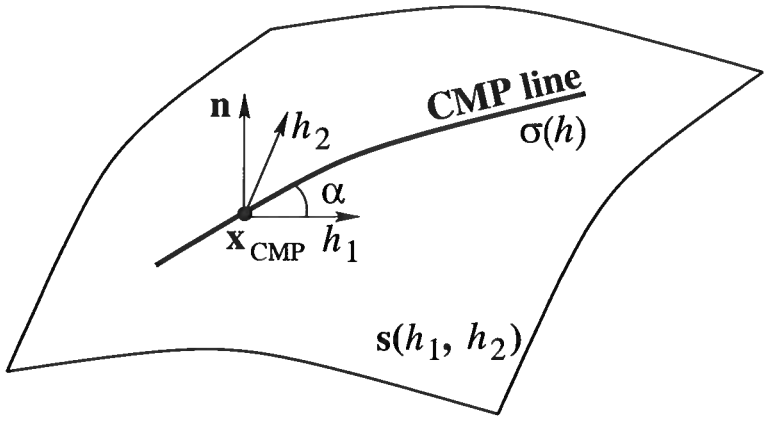

FIG. F.1. CMP line $\boldsymbol{\sigma}$ at an irregular surface described by the radius-vector $\mathbf{s}(h_1, h_2)$. $\mathbf{n}$ is the unit vector orthogonal to the surface at common midpoint $\mathbf{x}_{\text{CMP}}$.

$$\mathcal{L} = [\cos\alpha,\, \sin\alpha,\, 0]\,, \tag{F.1.4}$$

and one can replace $\mathcal{L}$ with the vector ℓ which lies in $\mathbf{s}$:

$$\ell \equiv [\mathcal{L}_1,\, \mathcal{L}_2] = [\cos\alpha,\, \sin\alpha]\,. \tag{F.1.5}$$

To obtain the NMO velocity for any CMP line $\boldsymbol{\sigma}$ within $\mathbf{s}$, one needs to express the curvature $\mathcal{K}$ in equation (E.1.33) in terms of the derivatives of $\mathbf{s}$ with respect to the coordinates h_1 and h_2. Using equations (E.1.3), (F.1.2) and (F.1.3), one finds

$$\begin{aligned}\mathcal{K} &= \left.\frac{d^2\mathbf{s}}{dh^2}\right|_{\text{along }\boldsymbol{\sigma},\ h=0} = \left.\sum_{i,j=1}^{2} \frac{\partial^2\mathbf{s}}{\partial h_i\, \partial h_j}\, \frac{dh_i}{dh}\, \frac{dh_j}{dh}\right|_{h=0} \\ &= \boldsymbol{\kappa}_{11}\, \cos^2\alpha + 2\,\boldsymbol{\kappa}_{12}\, \sin\alpha\, \cos\alpha + \boldsymbol{\kappa}_{22}\, \sin^2\alpha\,,\end{aligned} \tag{F.1.6}$$

where

$$\boldsymbol{\kappa}_{ij} \equiv \left.\frac{\partial^2\mathbf{s}}{\partial h_i\, \partial h_j}\right|_{h_1=h_2=0}, \qquad (i,j = 1,2)\,. \tag{F.1.7}$$

Equation (F.1.6) can be rewritten in matrix form using equation (F.1.5):

$$\mathcal{K} = \ell\, \boldsymbol{\kappa}\, \ell^{\mathbf{T}} . \tag{F.1.8}$$

Equation (E.1.33) then yields

$$V_{\text{nmo}}^{-2}(\mathbf{s}, \ell) = \ell\, (\mathbf{W} + \tau_0\, \mathbf{p} \cdot \boldsymbol{\kappa})\, \ell^{\mathbf{T}} , \tag{F.1.9}$$

where

$$W_{ij} \equiv U_{ij} , \qquad (i, j = 1, 2) . \tag{F.1.10}$$

Thus, the directional dependence of the NMO velocity $V_{\text{nmo}}(\mathbf{s}, \ell)$ measured on the irregular surface $\mathbf{s}$ can be described in terms of the following 2×2 symmetric quadratic form:

$$\mathcal{W} \equiv \mathbf{W} + \tau_0\, \mathbf{p} \cdot \boldsymbol{\kappa} , \tag{F.1.11}$$

where $\mathbf{W}$ is the matrix that represents the NMO ellipse in the plane tangent to $\mathbf{s}$ at the CMP location, and $\tau_0\, \mathbf{p} \cdot \boldsymbol{\kappa}$ is the correction for the curvature.

APPENDIX G

G.1 Continuation of NMO velocities through irregular interfaces

Grechka and Tsvankin (2002a) developed a concise Dix-type formula for anisotropic models composed of homogeneous layers separated by planar interfaces. They showed that the effective NMO ellipse at a given CMP location can be obtained by averaging the intersections of the NMO-velocity surfaces with the layer boundaries along the zero-offset ray.

the derivation of Grechka and Tsvankin (2002a) was based on the fact that the intersections of the NMO-velocity surfaces $\mathbf{U}$ with the planar boundaries (i.e., the NMO ellipses $\mathbf{W}$) are the same on both sides of each interface. For irregular interfaces, the quantities continuous across the interfaces are the matrices $\mathcal{W}$ defined by equation (F.1.11). Indeed, $\mathcal{W}$ determine the NMO velocities measured on the top (+) and bottom (−) sides of the interface $\mathbf{s}$ (Figure G.1). According to equation (F.1.11),

$$\mathcal{W}^{(+)} = \mathbf{W}^{(+)} + \tau_0 \, \mathbf{p}^{(+)} \cdot \boldsymbol{\kappa} \,, \tag{G.1.1}$$

$$\mathcal{W}^{(-)} = \mathbf{W}^{(-)} + \tau_0 \, \mathbf{p}^{(-)} \cdot \boldsymbol{\kappa} \,. \tag{G.1.2}$$

As shown in Appendix E, NMO velocity can be computed using the one-way traveltimes from the zero-offset reflection point to the CMP line. Essentially, those traveltimes correspond to the wavefront propagating from the zero-offset reflection point.

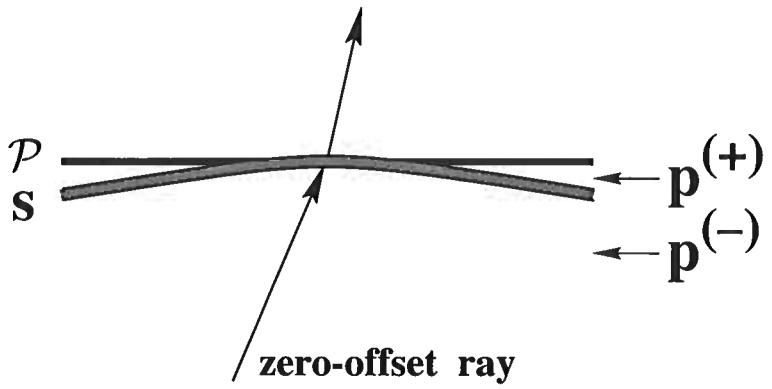

FIG. G.1. Zero-offset ray crossing an irregular interface **s**. Plane $\mathcal{P}$ is tangent to the interface at the intersection point; $\mathbf{p}^{(+)}$ and $\mathbf{p}^{(-)}$ are the slowness vectors on different sides of the interface.

To satisfy the boundary conditions, the wavefront has to be continuous across surface **s**, which implies that the NMO velocities measured on two sides of **s** at the reflection/transmission point (Figure G.1) are identical. Therefore,

$$\mathcal{W}^{(+)} = \mathcal{W}^{(-)}\,. \tag{G.1.3}$$

In contrast, the NMO ellipses $\mathbf{W}^{(+)}$ and $\mathbf{W}^{(-)}$ measured on two sides of the plane $\mathcal{P}$ tangent to **s** have to be different because the slowness vector changes across the interface. Combining equations (G.1.1)–(G.1.3), one finds

$$\mathbf{W}^{(+)} = \mathbf{W}^{(-)} - \tau_0 \left(\mathbf{p}^{(+)} - \mathbf{p}^{(-)}\right) \cdot \boldsymbol{\kappa}\,. \tag{G.1.4}$$

As discussed in the main text, the correction of NMO ellipses for the interface curvature developed here can be used to extend the Dix-type averaging formula of Grechka et al. (1999b) and Grechka and Tsvankin (2002a) to media with irregular interfaces.

APPENDIX H

H.1 Dix-type averaging for the Thomsen coefficient δ

As an example of the relationship between the effective and interval anisotropic parameters, consider the effective P-wave NMO velocity $\langle V_{P,\mathrm{nmo}} \rangle$ for a stack of horizontal homogeneous VTI layers. Here $\langle a \rangle$ denotes the effective value of the parameter a. The effective NMO velocity $\langle V_{P,\mathrm{nmo}} \rangle$ can be found using Dix (1955) averaging of the interval NMO velocities

$$\langle \tau \rangle \, \langle V_{P,\mathrm{nmo}} \rangle^2 = \sum_n \tau_n \, V^2_{P,\mathrm{nmo},n} \,, \tag{H.1.1}$$

where τ_n are the interval one-way zero-offset traveltimes, $V_{P,\mathrm{nmo},n}$ are the interval zero-dip NMO velocities, which relate to the interval vertical velocities $V_{P0,n}$ and interval anisotropic coefficients δ_n via equation (4.2.3),

$$V^2_{P,\mathrm{nmo},n} = V^2_{P0,n} \, (1 + 2\,\delta_n) \,, \tag{H.1.2}$$

and

$$\langle \tau \rangle = \sum_n \tau_n \tag{H.1.3}$$

is the total (effective) zero-offset traveltime.

The products of the interval vertical velocities $V_{P0,n}$ and zero-offset traveltimes τ_n determine the layer thicknesses

$$h_n = V_{P0,n}\,\tau_n\,, \tag{H.1.4}$$

which add up to produce the effective thickness

$$\langle h \rangle = \sum_n h_n \tag{H.1.5}$$

of the stack of layers. Then, the effective vertical velocity is defined as

$$\langle V_{P0} \rangle = \frac{\langle h \rangle}{\langle \tau \rangle} = \frac{\sum_n h_n}{\sum_n \tau_n}\,. \tag{H.1.6}$$

Making use of equation (H.1.4), the effective vertical velocity can be written in the form

$$\left[\frac{1}{\langle V_{P0} \rangle}\right]^{-1} = \langle V_{P0} \rangle = \frac{\langle h \rangle}{\langle \tau \rangle} = \frac{\langle h \rangle}{\sum_n \frac{h_n}{V_{P0,n}}} = \left[\frac{1}{\langle h \rangle} \sum_n \frac{h_n}{V_{P0,n}}\right]^{-1}\,, \tag{H.1.7}$$

which explicitly shows that $\langle V_{P0} \rangle$ is the *harmonic* average of the interval vertical velocities $V_{P0,n}$.

Next, let us introduce the effective anisotropic coefficient $\langle \delta \rangle$ by analogy with equation (H.1.2):

$$\langle V_{P,\mathrm{nmo}} \rangle^2 = \langle V_{P0} \rangle^2 \left(1 + 2\,\langle \delta \rangle\right)\,. \tag{H.1.8}$$

The goal is to find the relationship between the effective $\langle \delta \rangle$ and the interval coefficients δ_n. Substituting equations (H.1.2), (H.1.4), (H.1.6), and (H.1.8) into the Dix formula (H.1.1), one obtains

$$\langle h \rangle \, \langle V_{P0} \rangle \, (1 + 2 \, \langle \delta \rangle) = \sum_n h_n \, V_{P0,n} \, (1 + 2 \, \delta_n) \tag{H.1.9}$$

or

$$\langle V_{P0} \rangle \, (1 + 2 \, \langle \delta \rangle) = \frac{1}{\langle h \rangle} \sum_n h_n \, V_{P0,n} \, (1 + 2 \, \delta_n) \; . \tag{H.1.10}$$

The latter simply says that the product $\langle V_{P0} \rangle \, (1 + 2 \, \langle \delta \rangle)$ is the *arithmetic* average of the interval products $V_{P0,n} \, (1 + 2 \, \delta_n)$. Since the effective vertical velocity $\langle V_{P0} \rangle$ itself, being the harmonic average of the velocities $V_{P0,n}$, cannot be greater than its arithmetic average, the effective $\langle \delta \rangle$, found from equation (H.1.10), always gives some overestimate of the interval δ_n.

The last conclusion can be illustrated rewriting equation (H.1.10) in the following form:

$$1 + 2 \, \langle \delta \rangle = \frac{\frac{1}{\langle h \rangle} \sum_n h_n \, V_{P0,n}}{\langle V_{P0} \rangle} + 2 \, \frac{\frac{1}{\langle h \rangle} \sum_n h_n \, V_{P0,n} \, \delta_n}{\langle V_{P0} \rangle} \; . \tag{H.1.11}$$

Note, since no approximations have been made, this equation is exact. The first term in its right-hand side is the ratio of the arithmetic and harmonic averages of the vertical velocities, therefore, it is always greater or equal than unity. Thus, we arrive to the following inequality

$$\langle \delta \rangle \geq \frac{\frac{1}{\langle h \rangle} \sum_n h_n \, V_{P0,n} \, \delta_n}{\langle V_{P0} \rangle} \; . \tag{H.1.12}$$

In particular, when δ_n in all the layers are equal, i.e.,

$$\delta_1 = \delta_2 = \ldots = \delta_n = \ldots = \tilde{\delta} \, , \tag{H.1.13}$$

inequality (H.1.12) yields

$$\langle \delta \rangle \geq \tilde{\delta} \,. \tag{H.1.14}$$

The equality is reached only if all interval velocities $V_{P0,n}$ are equal, in which case the stack of the layers degenerates into a single layer. In the special case of isotropy, $\tilde{\delta} = 0$, and one has

$$\langle \delta \rangle \geq 0 \,. \tag{H.1.15}$$

Therefore, we are getting some nonzero positive effective δ just due to layering.

The simple math presented here might shed some light on the well known discrepancy between the laboratory measurements on shale cores, which give both positive and negative δ (Thomsen, 1986; Vernik and Liu, 1997), and seismic velocities in sedimentary basins, which always lead to the positive values of δ. While the measurements on the scale of a rock sample can be thought to correspond to the interval values, the seismic data, which always involve averaging over some interval, produce more like effective quantities. Therefore, δ obtained from seismic should be always greater than that measured in the lab.

H.1.1 Two layers

To give an example of the expected values of $\langle \delta \rangle$, consider a stack of two layers that have equal thicknesses

$$h_1 = h_2 \,. \tag{H.1.16}$$

In this case, equation (H.1.11) reduces to

$$1 + 2\,\langle\delta\rangle = \frac{V_{P0,1} + V_{P0,2}}{4\,V_{P0,1}\,V_{P0,2}}\Big[V_{P0,1} + V_{P0,2} + 2\,(V_{P0,1}\,\delta_1 + V_{P0,2}\,\delta_2)\Big]\,. \tag{H.1.17}$$

Introducing the ratio of the vertical velocities

$$\upsilon = \frac{V_{P0,2}}{V_{P0,1}} \tag{H.1.18}$$

leads to the following simplification of equation (H.1.17)

$$1 + 2\,\langle\delta\rangle = \frac{1+\upsilon}{4\,\upsilon}\Big[1 + \upsilon + 2\,(\delta_1 + \upsilon\,\delta_2)\Big]\,. \tag{H.1.19}$$

This finally yields the effective $\langle\delta\rangle$:

$$\langle\delta\rangle = \frac{(1-\upsilon)^2}{8\,\upsilon} + \frac{1+\upsilon}{4\,\upsilon}\,(\delta_1 + \upsilon\,\delta_2)\;, \tag{H.1.20}$$

which can be treated as a function of the velocity ratio υ.

An example of $\langle\delta(\upsilon)\rangle$ is presented in Figure H.1. We see that the values of $\langle\delta\rangle$ are bounded by the interval parameters δ_1 and δ_2 only for relatively mild velocity variations, i.e., when υ is close to one. As the deviation of the interval velocity ratio from unity increases, $\langle\delta\rangle$ grows and at some point exceeds the $\max(\delta_1, \delta_2)$.

Analysis of the dependence (H.1.20) for positive υ shows that the function $\langle\delta(\upsilon)\rangle$ has the only minimum at

$$\upsilon = \sqrt{\frac{1+2\,\delta_1}{1+2\,\delta_2}}\,. \tag{H.1.21}$$

Based on the asymptotic values,

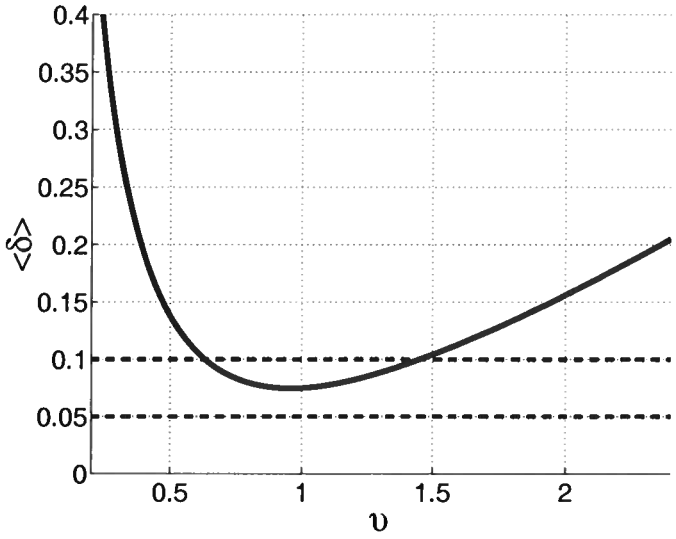

FIG. H.1. The function $\langle\delta(v)\rangle$ for two horizontal VTI layers (solid). The dashed lines indicate the values of interval anisotropic coefficients δ_1 and δ_2.

$$\lim_{v\to+0}\langle\delta(v)\rangle = +\infty \quad \text{and} \quad \lim_{v\to+\infty}\langle\delta(v)\rangle = +\infty\,. \tag{H.1.22}$$

Therefore, the difference between the effective $\langle\delta\rangle$ and the $\max(\delta_1,\delta_2)$ becomes greater with the increase of the absolute difference between the velocities $V_{P0,1}$ and $V_{P0,2}$. Figure H.1 confirms this conclusion. It also shows that $\langle\delta\rangle$ can significantly exceed the interval δ-values for the velocity variability routinely observed in the sedimentary basins.

APPENDIX I

I.1 Derivation of the quartic moveout coefficient

Here, we develop a general analytic expression for the quartic moveout coefficient A_4 by extending the approach employed by Grechka and Tsvankin (2002a) in their analysis of NMO-velocity surfaces. Suppose the traveltime t of a certain pure (non-converted) reflected wave is recorded on a CMP line parallel to the unit vector $\mathbf{L}$. The coordinates of the source $\mathbf{S}$ and receiver $\mathbf{R}$ are defined by the vectors $\mathbf{y}$ - $\mathbf{h}$ and $\mathbf{y} + \mathbf{h}$ (Figure 7.1), where $\mathbf{y}$ corresponds to the midpoint, and the half-offset vector $\mathbf{h}$ can be represented as

$$\mathbf{h} = h\,\mathbf{L} = h\,[L_1, L_2, 0]. \tag{I.1.1}$$

To obtain the quartic moveout coefficient, we expand the two-way traveltime in a Taylor series with respect to the half-offset h in the vicinity of the CMP location (h=0):

$$t(h, \mathbf{L}) = t_0 + \left.\frac{dt}{dh}\right|_{h=0} h + \left.\frac{d^2t}{dh^2}\right|_{h=0} \frac{h^2}{2!} + \left.\frac{d^3t}{dh^3}\right|_{h=0} \frac{h^3}{3!} + \left.\frac{d^4t}{dh^4}\right|_{h=0} \frac{h^4}{4!} + \ldots, \tag{I.1.2}$$

where t_0 is the zero-offset traveltime.

For a pure (non-converted) reflection mode, t is an even function of h because the traveltime remains the same when the source and receiver are interchanged. There-

fore, the odd derivatives of t can be dropped from equation (I.1.2), which leads to

$$t(h,\mathbf{L}) = t_0 + \left.\frac{d^2t}{dh^2}\right|_{h=0} \frac{h^2}{2!} + \left.\frac{d^4t}{dh^4}\right|_{h=0} \frac{h^4}{4!} + \ldots \tag{I.1.3}$$

To find the derivatives in equation (I.1.3), it is convenient to treat reflection traveltime for a fixed CMP location $\mathbf{y}$ as a function of $\mathbf{h}$ and the coordinates $[x_1, x_2, z(x_1, x_2)]$ of the reflection point $\mathbf{x}$ since the specular reflection point is determined by the source and receiver positions, $t = t(\mathbf{h}, \mathbf{x}(\mathbf{h}))$. Using this representation of traveltime and taking into account equation (I.1.1) yields

$$\frac{dt}{dh} = \frac{\partial t}{\partial h_k} L_k + \frac{\partial t}{\partial x_k} \frac{dx_k}{dh}, \qquad (k = 1, 2)\,. \tag{I.1.4}$$

According to Fermat's principle, for the specular ray

$$\frac{\partial t}{\partial x_k} = 0\,, \tag{I.1.5}$$

and equation (I.1.4) takes the form

$$\frac{dt}{dh} = \frac{\partial t}{\partial h_k} L_k\,. \tag{I.1.6}$$

Evaluating the derivative of equation (I.1.6), we obtain

$$\frac{d^2t}{dh^2} = \frac{\partial^2 t}{\partial h_k\, \partial h_m} L_k L_m + \frac{\partial^2 t}{\partial h_k\, \partial x_m} \frac{dx_m}{dh} L_k\,, \tag{I.1.7}$$

where $k = 1, 2$ and $m = 1, 2$.

Differentiating equation (I.1.7) twice gives the following expression for the fourth derivative of t:

$$\frac{d^4t}{dh^4} = \frac{\partial^4 t}{\partial h_p \partial h_k \partial h_m \partial h_n} L_p L_k L_m L_n + 3 \frac{\partial^3 t}{\partial x_n \partial h_k \partial h_m} \frac{\partial^2 x_n}{\partial h^2} L_k L_m$$

$$
\begin{aligned}
&+ \frac{\partial^4 t}{\partial x_p \partial h_k \partial h_m \partial h_n} \frac{\partial x_p}{\partial h} L_k L_m L_n + 2 \frac{\partial^4 t}{\partial h \partial x_n \partial h_k \partial h_m} \frac{\partial x_n}{\partial h} L_k L_m \\
&+ \frac{\partial^4 t}{\partial h \partial x_n \partial x_m \partial h_k} \frac{\partial x_n}{\partial h} \frac{\partial x_m}{\partial h} L_k + \frac{\partial^3 t}{\partial x_n \partial x_m \partial h_k} \frac{\partial}{\partial h} \left(\frac{\partial x_n}{\partial h} \frac{\partial x_m}{\partial h} \right) L_k \\
&+ \frac{\partial^2 t}{\partial x_m \partial h_k} \frac{\partial^3 x_m}{\partial h^3} L_k + \frac{\partial^3 t}{\partial x_n \partial x_m \partial h_k} \frac{\partial x_n}{\partial h} \frac{\partial^2 x_m}{\partial h^2} L_k \,. \qquad \text{(I.1.8)}
\end{aligned}
$$

Since not only the traveltime, but also the ray trajectory, stays the same when the source and receiver are interchanged, the vector $\mathbf{x}$ is an even function of h:

$$
\mathbf{x}(\mathbf{y}, h\mathbf{L}) = \mathbf{x}(\mathbf{y}, -h\mathbf{L}) \,, \qquad \text{(I.1.9)}
$$

and

$$
\left. \frac{d\mathbf{x}}{dh} \right|_{h=0} = \left. \frac{d^3\mathbf{x}}{dh^3} \right|_{h=0} = 0 \,. \qquad \text{(I.1.10)}
$$

Taking equation (I.1.10) into account, the derivative d^4t/dh^4 [equation (I.1.8)] at the CMP location (h=0) becomes

$$
\begin{aligned}
\left. \frac{d^4 t}{dh^4} \right|_{h=0} &= \left. \frac{\partial^4 t}{\partial h_p \partial h_k \partial h_m \partial h_n} \right|_{h=0} L_p L_k L_m L_n \\
&+ 3 \left. \frac{\partial^3 t}{\partial x_n \partial h_k \partial h_m} \right|_{h=0} \left. \frac{\partial^2 x_n}{\partial h^2} \right|_{h=0} L_k L_m \,. \qquad \text{(I.1.11)}
\end{aligned}
$$

Introducing the offset X ($X = 2h$) and the one-way zero-offset traveltime τ_0, and using the results of Fomel and Grechka (2001), we can rewrite equation (I.1.11) as

$$
\begin{aligned}
\left. \frac{d^4 t}{dX^4} \right|_{X=0} = \frac{1}{8} \Bigg[& \frac{\partial^4 \tau_0}{\partial y_p \partial y_k \partial y_m \partial y_n} L_p L_k L_m L_n \\
& + 3 \frac{\partial^3 \tau_0}{\partial x_n \partial y_k \partial y_m} \left(\left. \frac{\partial^2 x_n}{\partial h^2} \right|_{h=0} \right) L_k L_m \Bigg] \,, \qquad \text{(I.1.12)}
\end{aligned}
$$

where the derivatives with respect to x_i and y_i are evaluated at the zero-offset reflection point and the CMP location.

To represent the derivatives $(\partial^2 x_n/\partial h^2)$ in terms of the traveltime, we use Fermat's principle expressed in the following form (Grechka and Tsvankin, 2002a):

$$\frac{\partial t}{\partial x_n} = 0, \quad (n = 1, 2). \tag{I.1.13}$$

Differentiating equation (I.1.13) twice with respect to h yields

$$\frac{\partial^3 t}{\partial h_p \partial h_k \partial x_n} L_p L_k + \frac{\partial^2 t}{\partial x_k \partial x_n} \left(\left. \frac{\partial^2 x_k}{\partial h^2} \right|_{h=0} \right) = 0\,, \tag{I.1.14}$$

and

$$\frac{\partial^3 \tau_0}{\partial y_p \partial y_k \partial x_n} L_p L_k + \frac{\partial^2 \tau_0}{\partial x_k \partial x_n} \left(\left. \frac{\partial^2 x_k}{\partial h^2} \right|_{h=0} \right) = 0\,. \tag{I.1.15}$$

As before, all derivatives in equations (I.1.14) and (I.1.15) are computed for the zero-offset ray. Two equations (I.1.15) corresponding to $n = 1, 2$ can be solved for the derivatives $(\partial^2 x_1/\partial h^2)$ and $(\partial^2 x_2/\partial h^2)$ at $h = 0$. Substituting the result into equation (I.1.12) yields

$$\left. \frac{d^4 t}{dX^4} \right|_{X=0} = \frac{1}{8} \left[\frac{\partial^4 \tau_0}{\partial y_p \partial y_k \partial y_m \partial y_n} L_p L_k L_m L_n \right.$$
$$\left. - 3 \frac{\partial^3 \tau_0}{\partial x_i \partial y_k \partial y_m} \left(\frac{\partial^2 \tau_0}{\partial x_i \partial x_j} \right)^{-1} \frac{\partial^3 \tau_0}{\partial x_j \partial y_p \partial y_n} L_k L_m L_p L_n \right]. \tag{I.1.16}$$

After the fourth traveltime derivative has been derived, the quartic moveout coefficient can be obtained from the Taylor series (I.1.3). Introducing the offset $X = 2h$ into equation (I.1.3) and squaring the first three terms of the series leads to

$$t^2(X,\mathbf{L}) \approx \left(t_0 + \left.\frac{d^2t}{dX^2}\right|_{X=0} \frac{X^2}{2!} + \left.\frac{d^4t}{dX^4}\right|_{X=0} \frac{X^4}{4!} \right)^2 . \tag{I.1.17}$$

Keeping only the quartic and lower-order terms in X transforms equation (I.1.17) into

$$t^2(X,\mathbf{L}) \approx A_0 + A_2X^2 + A_4X^4 . \tag{I.1.18}$$

Here, $A_0 = t_0^2 = 4\tau_0^2$ denotes the squared two-way zero-offset traveltime,

$$A_2 = t_0 \left.\frac{d^2t}{dX^2}\right|_{X=0} = \tau_0 \frac{\partial^2\tau_0}{\partial y_k\,\partial y_m} L_kL_m = \frac{1}{V^2_{\mathrm{nmo}}(\mathbf{L})} \tag{I.1.19}$$

is the quantity reciprocal to the squared NMO velocity on CMP line $\mathbf{L}$ (Grechka and Tsvankin, 1998b), and

$$A_4 = \frac{\tau_0}{6}\left.\frac{d^4t}{dX^4}\right|_{X=0} + \frac{1}{4}\left(\left.\frac{d^2t}{dX^2}\right|_{X=0}\right)^2 . \tag{I.1.20}$$

Substituting the derivatives d^4t/dX^4 from equation (I.1.16) and d^2t/dX^2 from equation (I.1.19) into equation (I.1.20) yields the final expression for the quartic coefficient:

$$\begin{aligned} A_4 = \frac{1}{16} \Bigg[& \frac{\partial^2\tau_0}{\partial y_k\,\partial y_l}\frac{\partial^2\tau_0}{\partial y_m\,\partial y_n} + \frac{\tau_0}{3}\frac{\partial^4\tau_0}{\partial y_k\,\partial y_l\,\partial y_m\,\partial y_n} \\ & - \tau_0 \frac{\partial^3\tau_0}{\partial y_k\,\partial y_l\,\partial x_i}\left(\frac{\partial^2\tau_0}{\partial x_i\,\partial x_j}\right)^{-1}\frac{\partial^3\tau_0}{\partial x_j\,\partial y_m\,\partial y_n}\Bigg] L_kL_lL_mL_n . \end{aligned} \tag{I.1.21}$$

APPENDIX J

J.1 Weak-anisotropy approximation for the P-wave quartic moveout coefficient in tilted TI media, with symmetry axis contained in the dip plane

We consider a homogeneous transversely isotropic layer above a plane dipping reflector and assume that the symmetry axis (unit vector $\mathbf{c}$) lies in the dip plane (Figure J.1). Without losing generality, the x_1-axis can be aligned with the dip direction, so that the vector $\mathbf{c}$ is given by

$$\mathbf{c} = [\sin\nu, 0, \cos\nu]\,. \tag{J.1.1}$$

The zero-offset ray should be confined to the dip plane that represents a vertical plane of symmetry for the whole model (Figure J.1). The two-way traveltime between the common-midpoint $\mathbf{y}$ and the reflector in a homogeneous medium is simply

$$t(y_1, y_2, x_1, x_2) = \frac{2\sqrt{(x_1 - y_1)^2 + (x_2 - y_2)^2 + z^2(x_1, x_2)}}{V_g(y_1, y_2, x_1, x_2)}\,. \tag{J.1.2}$$

Here $z(x_1, x_2)$ defines the reflecting plane, and $V_g(y_1, y_2, x_1, x_2)$ is the group velocity. Using the weak-anisotropy approximations for the P-wave group velocity and group

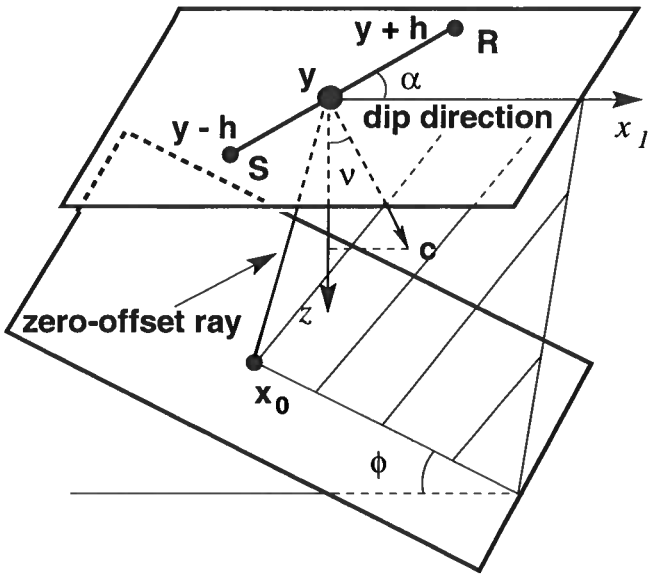

FIG. J.1. The reflected wave is recorded above a homogeneous TI layer with a dipping lower boundary. The symmetry axis is contained in the dip plane $[x_1, x_3]$, but may be tilted away from the vertical at an arbitrary angle ν.

angle in TI media (Tsvankin, 2001), we find

$$V_g = \frac{V_{P0}}{4}[4 + m(-\delta - \epsilon - \eta \sin^2 a \sin^2 b - \eta \cos 2\nu(2\cos^2 b \sin^2 a + \sin^2 a \sin^2 b - 1) + \eta \cos b \sin 2a \sin 2\nu)], \tag{J.1.3}$$

where we have denoted

$$\sin a \equiv \frac{\sqrt{(y_1 - x_1)^2 + (y_2 - x_2)^2}}{\sqrt{(y_1 - x_1)^2 + (y_2 - x_2)^2 + z^2}}, \tag{J.1.4}$$

$$\cos a \equiv \frac{z}{\sqrt{(y_1 - x_1)^2 + (y_2 - x_2)^2 + z^2}}, \tag{J.1.5}$$

$$\sin b \equiv \frac{(y_2 - x_2)}{\sqrt{(y_1 - x_1)^2 + (y_2 - x_2)^2}}, \tag{J.1.6}$$

$$\cos b \equiv \frac{(y_1 - x_1)}{\sqrt{(y_1 - x_1)^2 + (y_2 - x_2)^2}}, \tag{J.1.7}$$

$$m \equiv -1 - \sin^2 a \sin^2 b - \cos 2\nu \left(-1 + 2\sin^2 a \cos^2 b + \sin^2 a \sin^2 b\right) + \cos b \sin 2a \sin 2\nu \,. \tag{J.1.8}$$

The parameters used in equation (J.1.3) are introduced in the main text. Since the zero-offset traveltime needs to satisfy Fermat's principle, the minimum value of t corresponds to the coordinates of the zero-offset reflection point $x_1^{(0)}$ and $x_2^{(0)}$. This implies that the derivatives of $t(y_1, y_2, x_1, x_2)$ with respect to x_1 and x_2 vanish at the point $[x_1^{(0)}, x_2^{(0)}]$:

$$\left.\frac{\partial t(y_1, y_2, x_1, x_2)}{\partial x_1}\right|_{\left[x_1^{(0)}, x_2^{(0)}\right]} = 0\,, \tag{J.1.9}$$

$$\left.\frac{\partial t(y_1, y_2, x_1, x_2)}{\partial x_2}\right|_{\left[x_1^{(0)}, x_2^{(0)}\right]} = 0\,. \tag{J.1.10}$$

Equations (J.1.9) and (J.1.10) can be used to relate the CMP coordinates y_1 and y_2 to the coordinates $x_1^{(0)}$ and $x_2^{(0)}$ of the zero-offset reflection point. Substituting equations (J.1.2) and (J.1.3) into equations (J.1.9) and (J.1.10) and dropping quadratic and higher-order terms in the anisotropic coefficients yields

$$y_1 = z\left[\delta + \eta - \eta \cos 2(\phi - \nu)\right] \frac{\sin 2(\phi - \nu)}{\cos^2 \phi} + z \tan \phi + x_1^{(0)}\,, \tag{J.1.11}$$

$$y_2 = x_2^{(0)}\,. \tag{J.1.12}$$

Using equations (J.1.2), (J.1.11), and (J.1.12) to evaluate the derivatives in equation (I.1.21), we obtain the following linearized approximation for the P-wave quartic moveout coefficient:

$$A_4^{\mathrm{TTI}} = -\frac{2\,\eta}{t_{P0}^2\,V_{P0}^4}\,F(\alpha,\,\phi,\,\nu)\,, \tag{J.1.13}$$

where

$$\begin{aligned} F(\alpha,\,\phi,\,\nu) \;=\; & \frac{9}{64} + \frac{1}{128}\,[-24\cos 2\alpha + 6\cos 4\alpha + 8\cos(6\phi - 4\nu) + 4\cos 2(\alpha - 2\nu) \\ & -4\cos(4\alpha - 2\nu) + 24\cos 2(\phi - 2\nu) + 12\cos 2(\alpha + \phi - 2\nu) \\ & +8\cos 2(\alpha + 2\phi - 2\nu) + 4\cos 2(\alpha + 3\phi - 2\nu) + \cos 4(\alpha - \nu) \\ & +32\cos 2(\phi - \nu) + 32\cos 4(\phi - \nu) - 16\cos 2(\alpha + \phi - \nu) \\ & +8\cos 2\nu + 6\cos 4\nu + \cos 4(\alpha + \nu) - 4\cos 2(2\alpha + \nu) \\ & -16\cos 2(\alpha - \phi + \nu) + 4\cos 2(\alpha + 2\nu) + 4\cos 2(\alpha - 3\phi + 2\nu) \\ & +8\cos 2(\alpha - 2\phi + 2\nu) + 12\cos 2(\alpha - \phi + 2\nu)]\,. \end{aligned} \tag{J.1.14}$$

APPENDIX K

K.1 Weak-anisotropy approximation for the P-wave quartic moveout coefficient in tilted TI media, with symmetry axis out of the dip plane

Here, we obtain the weak-anisotropy approximation (WAA) for the quartic coefficient in general TTI media; the symmetry axis (unit vector **c**) does not lie in the dip plane of the structure (Figure K.1). Without loss of generality, the x_1-axis is aligned with the dip direction, so that the vector **c** is given by

$$\mathbf{c} = [\sin\nu\cos\beta, \sin\nu\sin\beta, \cos\nu]\,, \tag{K.1.1}$$

where β is the azimuth of the symmetry axis measured from the dip plane (Figure K.1). Because the symmetry axis is outside the dip plane of the structure, the zero-offset ray is not confined to the dip plane; the dip plane of the structure is not a vertical symmetry plane. As in the case analyzed in Appendix J, the two-way traveltime between the common-midpoint **y** and the reflector is given by equation (J.1.2). Because the symmetry axis has an arbitrary orientation, however, the P-wave group velocity is given as follows

$$V_g = \frac{V_{P0}}{64}[64 - \frac{1}{16}(-20 + 4\cos 2a + 4\cos(2b - 2\beta)$$

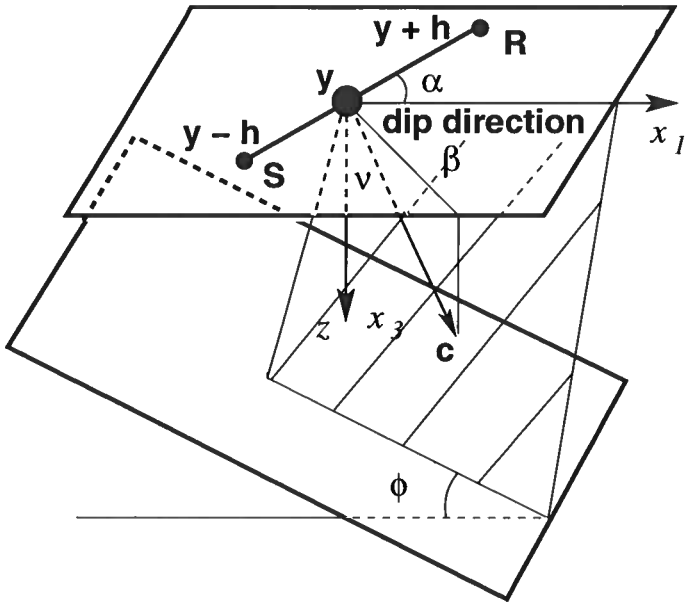

FIG. K.1. The reflected wave is recorded above a homogeneous TI layer with a dipping lower boundary. The symmetry axis is outside of the dip plane $[x_1, x_3]$. The tilt and azimuth of the symmetry axis are ν and β, respectively.

$$
\begin{aligned}
&-2\cos(2a+2b-2\beta)-2\cos(2a-2b+2\beta)\\
&+8\cos a\ \cos(a+b-\beta-2\nu)+8\cos a\ \cos(a-b+\beta-2\nu)\\
&+6\cos(2a-2\nu)-2\cos(2b-2\beta-2\nu)+\cos(2a+2b-2\beta-2\nu)\\
&+\cos(2a-2b+2\beta-2\nu)+4\cos 2\nu+6\cos(2a+2\nu)\\
&-2\cos(2b-2\beta+2\nu)+\cos(2a+2b-2\beta+2\nu)\\
&+\cos(2a-2b+2\beta+2\nu)-8\cos a\ \cos(a+b-\beta+2\nu)\\
&-8\cos a\ \cos(a-b+\beta+2\nu))(12\delta+20\epsilon+4(\delta-\epsilon)\cos 2a\\
&+4(\delta-\epsilon)\cos(2b-2\beta)-2\delta\cos(2a+2b-2\beta)\\
&+2\epsilon\cos(2a+2b-2\beta)-2\delta\cos(2a-2b+2\beta)\\
&+2\epsilon\cos(2a-2b+2\beta)+8\delta\cos a\ \cos(a+b-\beta-2\nu)\\
&-8\epsilon\cos a\ \cos(a+b-\beta-2\nu)+8\delta\cos a\ \cos(a-b+\beta-2\nu)
\end{aligned}
$$

$$
\begin{aligned}
&-8\epsilon\cos a\ \cos(a-b+\beta-2\nu)+6\delta\cos(2a-2\nu)\\
&-6\epsilon\cos(2a-2\nu)-2\delta\cos(2b-2\beta-2\nu)\\
&+2\epsilon\cos(2b-2\beta-2\nu)+\delta\cos(2a+2b-2\beta-2\nu)\\
&-\epsilon\cos(2a+2b-2\beta-2\nu)+\delta\cos(2a-2b+2\beta-2\nu)\\
&-\epsilon\cos(2a-2b+2\beta-2\nu)+4\delta\cos 2\nu-4\epsilon\cos 2\nu\\
&+6\delta\cos(2a+2\nu)-6\epsilon\cos(2a+2\nu)\\
&-2\delta\cos(2b-2\beta+2\nu)+2\epsilon\cos(2b-2\beta+2\nu)\\
&+\delta\cos(2a+2b-2\beta+2\nu)-\epsilon\cos(2a+2b-2\beta+2\nu)\\
&+\delta\cos(2a-2b+2\beta+2\nu)-\epsilon\cos(2a-2b+2\beta+2\nu)\\
&-8\delta\cos a\ \cos(a+b-\beta+2\nu)+8\epsilon\cos a\ \cos(a+b-\beta+2\nu)\\
&-8\delta\cos a\ \cos(a-b+\beta+2\nu)+8\epsilon\cos a\ \cos(a-b+\beta+2\nu))]\,, \qquad \text{(K.1.2)}
\end{aligned}
$$

where $\sin a$, $\cos a$, $\sin b$, and $\cos b$ are given by equations (J.1.4) to (J.1.7).

Since the zero-offset traveltime needs to satisfy Fermat's principle, the minimum value of t corresponds to the coordinates of the zero-offset reflection point $x_1^{(0)}$ and $x_2^{(0)}$. This implies that the derivatives of $t(y_1, y_2, x_1, x_2)$ with respect to x_1 and x_2 vanish at the point $[x_1^{(0)}, x_2^{(0)}]$; these derivatives are defined by equations (J.1.9) and (J.1.10).

As in Appendix J, equations (J.1.9) and (J.1.10) can be used to relate the CMP coordinates y_1 and y_2 to the coordinates $x_1^{(0)}$ and $x_2^{(0)}$ of the zero-offset reflection point. Substituting equations (J.1.2) and (K.1.2) into equations (J.1.9) and (J.1.10) and dropping quadratic and higher-order terms in the anisotropic coefficients yields

$$
\begin{aligned}
y_1 \;=\;& x_1^{(0)}+(z(\sec^2\phi)(-4\delta+20\epsilon+4(\delta-\epsilon)\cos 2\beta\\
&-2(\delta-\epsilon)\cos(2\beta-2\phi)+4\delta\cos(2\phi)
\end{aligned}
$$

$$
\begin{aligned}
&-4\epsilon\cos 2\phi - 2\delta\cos(2\beta+2\phi) + 2\epsilon\cos(2\beta+2\phi)\\
&-2\delta\cos(2\beta-2\nu) + 2\epsilon\cos(2\beta-2\nu)\\
&+\delta\cos(2\beta-2\phi-2\nu) - \epsilon\cos(2\beta-2\phi-2\nu)\\
&+6\delta\cos(2\phi-2\nu) - 6\epsilon\cos(2\phi-2\nu)\\
&+\delta\cos(2\beta+2\phi-2\nu) - \epsilon\cos(2\beta+2\phi-2\nu) + 4\delta\cos 2\nu\\
&-4\epsilon\cos 2\nu - 2\delta\cos(2\beta+2\nu)\\
&+2\epsilon\cos(2\beta+2\nu) + \delta\cos(2\beta-2\phi+2\nu)\\
&-\epsilon\cos(2\beta-2\phi+2\nu) + 6\delta\cos(2\phi+2\nu)\\
&-6\epsilon\cos(2\phi+2\nu) + \delta\cos(2\beta+2\phi+2\nu) - \epsilon\cos(2\beta+2\phi+2\nu)\\
&+64\delta\cos\beta\cos\phi\cos\nu\sin\phi\sin\nu - 64\epsilon\cos\beta\cos\phi\cos\nu\sin\phi\sin\nu)\\
&(-((2-2\cos 2\beta+\cos(2\beta-2\nu)) + 6\cos 2\nu\\
&+\cos(2\beta+2\nu))\sin 2\phi) + 8\cos\beta\cos 2\phi\sin 2\nu))/128 - z\tan\phi\,, \qquad \text{(K.1.3)}
\end{aligned}
$$

$$
\begin{aligned}
y_2 \;=\; & x_2^{(0)} + (z(-4\delta+20\epsilon+4(\delta-\epsilon)\cos 2\beta\\
&-2(\delta-\epsilon)\cos(2\beta-2\phi) + 4\delta\cos 2\phi - 4\epsilon\cos 2\phi\\
&-2\delta\cos(2\beta+2\phi) + 2\epsilon\cos(2\beta+2\phi) + 4\delta\cos(\beta+2\phi-2\nu)\\
&-4\epsilon\cos(\beta+2\phi-2\nu) - 2\delta\cos(2\beta-2\nu) + 2\epsilon\cos(2\beta-2\nu)\\
&+\delta\cos(2\beta-2\phi-2\nu) - \epsilon\cos(2\beta-2\phi-2\nu)\\
&+6\delta\cos(2\phi-2\nu) - 6\epsilon\cos(2\phi-2\nu)\\
&+\delta\cos(2\beta+2\phi-2\nu) - \epsilon\cos(2\beta+2\phi-2\nu) + 4\delta\cos 2\nu\\
&-4\epsilon\cos 2\nu - 2\delta\cos(2\beta+2\nu) + 2\epsilon\cos(2\beta+2\nu)\\
&+\delta\cos(2\beta-2\phi+2\nu) - \epsilon\cos(2\beta-2\phi+2\nu)
\end{aligned}
$$

$$
\begin{aligned}
&+6\delta\cos(2\phi+2\nu)-6\epsilon\cos(2\phi+2\nu)\\
&+\delta\cos(2\beta+2\phi+2\nu)-\epsilon\cos(2\beta+2\phi+2\nu)\\
&+4\delta\cos(\beta-2\phi+2\nu)-4\epsilon\cos(\beta-2\phi+2\nu)\\
&-4\delta\cos(\beta-2\phi+2\nu)+4\epsilon\cos(\beta-2\phi+2\nu)\\
&-4\delta\cos(\beta+2\phi+2\nu)+4\epsilon\cos(\beta+2\phi+2\nu))\\
&\sec\phi\sin\beta\sin\nu(\cos\phi\cos\nu+\cos\beta\sin\phi\sin\nu))/8\,, \qquad \text{(K.1.4)}
\end{aligned}
$$

where z is the depth of the zero-offset reflection point. Using equations (J.1.2), (K.1.2), (K.1.3), and (K.1.4) to evaluate the derivatives in equation (I.1.21), we obtain the following linearized approximations for the x_1- ($\alpha = 0°$) and x_2-line ($\alpha = 90°$) P-wave quartic coefficients when the dip of the reflector is 0°:

$$
\begin{aligned}
A^{\mathrm{TTI}}_{4,x_1}(\alpha=0°) \;=\;& -(\epsilon-\delta)(18-24\cos 2\beta+6\cos 4\beta+28\cos(2\beta-4\nu)\\
&-4\cos(4\beta-2\nu)-16\cos(2\beta-2\nu)+\cos(4\beta-4\nu)\\
&+40\cos 2\nu+70\cos 4\nu-16\cos(2\beta+2\nu)+\cos(4\beta+4\nu)\\
&-4\cos(4\beta+2\nu)+28\cos(2\beta+4\nu))/(256(V_{P0}z)^2)\,, \qquad \text{(K.1.5)}
\end{aligned}
$$

$$
\begin{aligned}
A^{\mathrm{TTI}}_{4,x_2}(\alpha=90°) \;=\;& -(\epsilon-\delta)(18+24\cos 2\beta+6\cos 4\beta-28\cos(2\beta-4\nu)\\
&-4\cos(4\beta-2\nu)+16\cos(2\beta-2\nu)+\cos(4\beta-4\nu)\\
&+40\cos 2\nu+70\cos 4\nu+16\cos(2\beta+2\nu)+\cos(4\beta+4\nu)\\
&-4\cos(4\beta+2\nu)-28\cos(2\beta+4\nu))/(256(V_{P0}z)^2)\,. \qquad \text{(K.1.6)}
\end{aligned}
$$

If the reflector is dipping, the expressions are more complicated, and it is impossible to write them in one page. Equations (K.1.5) and (K.1.6) show that the dependence of A_4 on the tilt (ν) and azimuth (β) of the symmetry axis is nonlinear. These

equations also tell us that regardless of the tilt and azimuth of the symmetry axis, the only anisotropic parameter that can be constrained is the parameter η. Moreover, if the medium has elliptical anisotropy, the quartic coefficient becomes equal to zero.

These equations also show that the dependencies of the x_1- and x_2-line quartic coefficients on the tilt (ν), and azimuth (β) of the symmetry axis differ. In addition, equations (K.1.5) and (K.1.6) illustrate that the x_1- and x_2-line quartic coefficients may be zero for some combinations of ν and β.

We used *Mathematica* to get the linearized expressions shown in this appendix.

APPENDIX L

L.1 Quartic coefficient for a homogeneous orthorhombic layer overlaying a plane dipping reflector

First, we review notation and some relevant properties of wave propagation for orthorhombic models. Seismic signatures in orthorhombic media can be conveniently described in terms of the two vertical velocities,

$$V_{P0} = \sqrt{\frac{c_{33}}{\rho}} \quad \text{and} \quad V_{S0} = \sqrt{\frac{c_{55}}{\rho}}, \tag{L.1.1}$$

and Thomsen-style anisotropic coefficients $\epsilon^{(1,2)}$, $\delta^{(1,2,3)}$, and $\gamma^{(1,2)}$ introduced by Tsvankin (1997c); c_{ij} are the components of the stiffness tensor and ρ is the density. The coefficients $\epsilon^{(i)}$, $\delta^{(i)}$, $\gamma^{(i)}$ $(i = 1, 2)$ defined in the vertical symmetry planes $[x_2, x_3]$ and $[x_1, x_3]$ (Figure L.1) have the same meaning as Thomsen's (1986) parameters ϵ, δ, and γ for transverse isotropy. The coefficient $\delta^{(3)}$ plays the role of Thomsen's δ in the horizontal plane $[x_1, x_2]$.

The kinematics of wave propagation in the symmetry planes of orthorhombic media is practically identical to that in VTI media. The only notable difference is caused by the so-called singularity directions in orthorhombic media (the point A in Figure L.1), where the phase velocities of two shear waves coincide. The S_2-wavefront near a singularity usually becomes multi-valued, while the wavefront of the fast S_1-wave

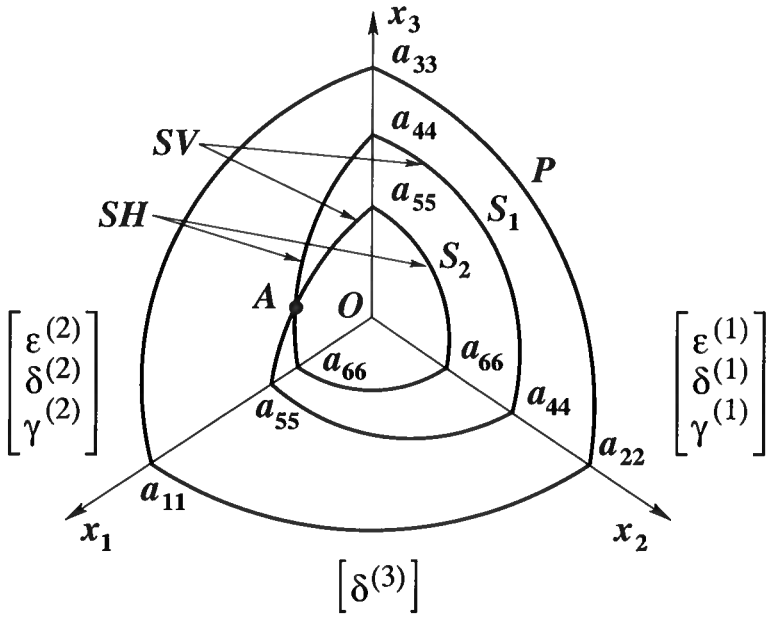

FIG. L.1. Sketch of body-wave phase-velocity surfaces in orthorhombic media (after Grechka et al., 1999b). The coefficients $\epsilon^{(1)}$, $\delta^{(1)}$ and $\gamma^{(1)}$ are defined in the symmetry plane $[x_2, x_3]$, while $\epsilon^{(2)}$, $\delta^{(2)}$ and $\gamma^{(2)}$ correspond to the plane $[x_1, x_3]$ (Tsvankin, 1997c). $a_{ij} \equiv \sqrt{c_{ij}/\rho}$, where c_{ij} are the stiffness coefficients and ρ is the density.

develops an elliptical hole. Those complicated phenomena are outside of the scope of this paper; here, we assume that the singularities are located outside of the fan of ray directions used for velocity analysis.

Here, we study the character of the quartic coefficient in a model that contains an orthorhombic layer overlaying a plane dipping reflector (Figure L.2); the orthorhombic layer contains one horizontal symmetry plane and two orthogonal vertical symmetry planes. One of the vertical symmetry planes coincides with the dip plane of the reflector. Thus, the zero-offset ray has to be confined to the dip plane that represents a vertical plane of symmetry for the whole model (Figure L.2).

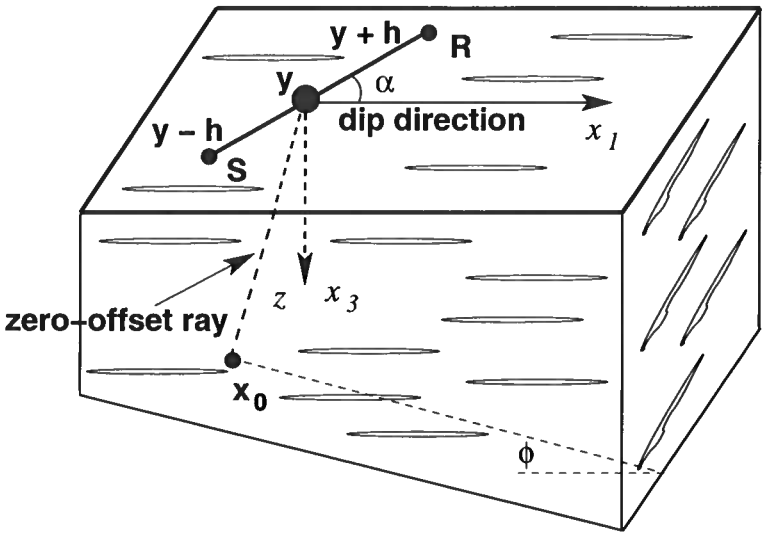

FIG. L.2. The reflected wave is recorded above a homogeneous orthorhombic layer with a dipping lower boundary. The dip plane $[x_1, x_3]$ is a vertical symmetry plane for the whole model.

Using the weak-anisotropy approximations for the P-wave group velocity (V_g) and group angle in orthorhombic media (Tsvankin, 2001), we get

$$\begin{aligned} V_g &= V_{P0}(1 - (\delta_2 - \epsilon_2)(\cos b \sin a)^4 + \delta_1(\sin a \sin b)^2 - (\delta_1 - \epsilon_1)(\sin a \sin b)^4 \\ &\quad + \cos^2 b(\delta_2 \sin^2 a - (\delta_1 + \delta_2 - \delta_3 - 2\epsilon_2) \sin^4 a \sin^2 b)), \end{aligned} \tag{L.1.2}$$

where $\sin a$, $\cos a$, $\sin b$, and $\cos b$ are given by equations (J.1.4) to (J.1.7).

By substituting equations (J.1.2) and (L.1.2) into equations (J.1.9) and (J.1.10) and dropping quadratic and higher-order terms in the anisotropic coefficients, we relate the coordinates y_1 and y_2 to the coordinates of the zero-offset reflection point ($x_1^{(0)}$,$x_2^{(0)}$)

$$y_1 = z\,[\delta_2 + (\epsilon_2 - \delta_2) - (\epsilon_2 - \delta_2)\cos 2(\phi - \nu)]\,\frac{\sin 2(\phi - \nu)}{\cos^2 \phi} + z \tan \phi + x_1^{(0)}, \tag{L.1.3}$$

$$y_2 = x_2^{(0)} \,. \tag{L.1.4}$$

Using equations (J.1.2), (L.1.2), (L.1.3), and (L.1.4) to evaluate the derivatives in equation (I.1.21), we obtain the following linearized approximation for the P-wave quartic moveout coefficient in orthorhombic media:

$$\begin{aligned} A_4^{\mathrm{ORT}} \;=\; & -(\cos^2\phi(-8\delta_1 - 4\delta_3 + 12\epsilon_1 - 4\epsilon_2 + 4(2\delta_1 - \delta_2 + 2\delta_3 - 4\epsilon_1 + 3\epsilon_2)\cos 2\alpha \\ & -4(\delta_3 - \epsilon_1 + \epsilon_2)\cos 4\alpha - \delta_2\cos(2\alpha - 6\phi) + \epsilon_2\cos(2\alpha - 6\phi) \\ & -2\delta_2\cos(2\alpha - 4\phi) + 2\epsilon_2\cos(2\alpha - 4\phi) + 4\delta_1\cos(2\alpha - 2\phi) - 3\delta_2\cos(2\alpha - 2\phi) \\ & -4\delta_3\cos(2\alpha - 2\phi) - \epsilon_2\cos(2\alpha - 2\phi) - 8\delta_1\cos 2\phi \\ & -6\delta_2\cos 2\phi + 8\delta_3\cos 2\phi + 14\epsilon_2\cos 2\phi \\ & -8\delta_2\cos 4\phi + 8\epsilon_2\cos 4\phi - 2\delta_2\cos 6\phi + 2\epsilon_2\cos 6\phi \\ & +4\delta_1\cos(2\alpha + 2\phi) - 3\delta_2\cos(2\alpha + 2\phi) - 4\delta_3\cos(2\alpha + 2\phi) \\ & -\epsilon_2\cos(2\alpha + 2\phi) - 2\delta_2\cos(2\alpha + 4\phi) + 2\epsilon_2\cos(2\alpha + 4\phi) - \delta_2\cos(2\alpha + 6\phi) \\ & +\epsilon_2\cos(2\alpha + 6\phi)))/(64(V_{P0}z)^2) \,. \end{aligned} \tag{L.1.5}$$

Rewriting equation (L.1.5) in terms of $\eta_1 \approx \epsilon_1 - \delta_1$, $\eta_2 \approx \epsilon_2 - \delta_2$, and $\eta_3 \approx \epsilon_1 - \delta_3 - \epsilon_2$ (Al-Dajani, Tsvankin and Toksoz, 1998), we get

$$\begin{aligned} A_4^{\mathrm{ORT}} \;=\; & -\frac{\eta_2}{2\,t_{P0}^2\,V_{P0}^4}\cos^2\phi\,[2\cos 2\phi\,(1 + \cos 2\alpha\cos 2\phi) + \cos 4\phi - 1] \\ & -\frac{2\,\eta_1}{t_{P0}^2\,V_{P0}^4}\cos^2\phi\,\sin^2\alpha + \frac{\eta_3}{t_{P0}^2\,V_{P0}^4}\sin^2\alpha\,[\cos 2\alpha + \cos 2\phi] \,. \end{aligned} \tag{L.1.6}$$

From equation (L.1.5), we obtain the dip- ($\alpha = 0°$) and strike-line ($\alpha = 90°$) quartic coefficients

$$A_{4,\mathrm{dip}}^{\mathrm{ORT}}(\alpha = 0°) \;=\; -\frac{2\,(\epsilon_2 - \delta_2)}{t_{P0}^2\,V_{P0}^4}\cos^4\phi\left(1 - 4\,\sin^2\phi\right) \,, \tag{L.1.7}$$

$$A_{4,\text{strike}}^{\text{ORT}}(\alpha = 90^\circ) = \frac{1}{4\, t_{P0}^2\, V_{P0}^4}[4\delta_1 - \delta_2 + 4\delta_3 - 8\epsilon_1 + 5\epsilon_2 + 4(\delta_1 - \delta_3 - \epsilon_2)\cos 2\phi + (\delta_2 - \epsilon_2)\cos 4\phi]\,, \tag{L.1.8}$$

where t_{P0} is the two-way zero offset traveltime. Rewriting equation (L.1.8) in terms of η_1, η_2, and η_3 yields

$$A_{4,\text{strike}}^{\text{ORT}} = -\frac{2}{t_{P0}^2\, V_{P0}^4}[\eta_1 \cos^2\phi - \eta_2 \cos^2\phi \sin^2\phi + \eta_3 \sin^2\phi]\,. \tag{L.1.9}$$

If $\phi = 90^\circ$, the strike-line quartic coefficient becomes

$$A_{4,\text{strike}}^{\text{ORT}}(\alpha = 90^\circ) = -\frac{2\,\eta_3}{t_{P0}^2\, V_{P0}^4}\,. \tag{L.1.10}$$

If we set $\delta_1 = \delta_2 = \delta$, $\epsilon_1 = \epsilon_2 = \epsilon$, and $\delta_3 = 0$ in equation (L.1.5), we obtain the linearized expression for A_4 valid for VTI media

$$A_4^{\text{VTI}} = -\frac{2\,(\epsilon - \delta)}{t_{P0}^2\, V_{P0}^4}\cos^4\phi\,\left(1 - 4\,\sin^2\phi\,\cos^2\alpha\right)\,. \tag{L.1.11}$$

By setting $\alpha = 0^\circ$ and $\alpha = 90^\circ$ in equation (L.1.11), we obtain the dip- and strike-line quartic coefficients

$$A_4^{\text{VTI}}(\alpha = 0^\circ) = -\frac{2\,(\epsilon - \delta)}{t_{P0}^2\, V_{P0}^4}\cos^4\phi\,\left(1 - 4\,\sin^2\phi\right)\,, \tag{L.1.12}$$

$$A_4^{\text{VTI}}(\alpha = 90^\circ) = -\frac{2\,(\epsilon - \delta)}{t_{P0}^2\, V_{P0}^4}\cos^4\phi\,. \tag{L.1.13}$$

Equation (L.1.7) has the same meaning as equation (L.1.12). From equation (L.1.7), it is clear that the dip-line quartic coefficient vanishes when $\phi = 30^\circ$. On the other hand, from equation (L.1.8), we can see that due to the presence of the plane dipping

reflector the strike-line quartic coefficient depends on the parameters δ_3, δ_2, and ϵ_2. By setting $\delta_1 = \delta_2 = \delta$, $\epsilon_1 = \epsilon_2 = \epsilon$, and $\delta_3 = 0$ in equation (L.1.8), equation (L.1.8) reduces to equation (L.1.13).

If the dip of the reflector is zero ($\phi = 0°$), from equation (L.1.5) we obtain the linearized version of Al-Dajani's solution (Al-Dajani, Tsvankin and Toksoz, 1998). This approximation is given as follows

$$\begin{aligned} A_4^{\mathrm{ORT}} &= -\frac{1}{4\,t_{P0}^2\,V_{P0}^4}[-4\delta_1 - 4\delta_2 + \delta_3 + 3\epsilon_1 + 5\epsilon_2 + 4(\delta_1 - \delta_2 - \epsilon_1 + \epsilon_2)\cos 2\alpha \\ &\quad -(\delta_3 - \epsilon_1 + \epsilon_2)\cos 4\alpha]\,. \end{aligned} \tag{L.1.14}$$

Rewriting equation (L.1.14) in terms of η_1, η_2, and η_3 yields

$$A_4^{\mathrm{ORT}} = -\frac{2}{t_{P0}^2\,V_{P0}^4}[\eta_2\cos^2\alpha - \eta_3\cos^2\alpha\sin^2\alpha + \eta_1\sin^2\alpha]\,. \tag{L.1.15}$$

Although equation (L.1.15) is an approximation, it has the exact azimuthal dependence.

APPENDIX M

M.1 Time field derivatives

The expression (I.1.21), Appendix I, is not valid if the medium contains more than one layer. If the medium is horizontally layered and it has a horizontal symmetry plane, it is possible to apply the technique developed by Al-Dajani and Tsvankin (1998). Here, we describe a more general approach to model the quartic coefficient in layered media, which can be used even if the medium contains heterogeneous anisotropic layers separated by plane dipping or irregular interfaces. This method was developed by Blyas, Gritsenko and Chernyak (1984) and later was used by Fomel (1994).

The key idea of this approach is to express partial derivatives measured at the surface of the earth in terms of traveltime derivatives that are function of the interval model parameters. Consider, for example, a model that has only two inhomogeneous anisotropic layers separated by an irregular interface (see Figure M.1).

In this medium, the traveltime $t(s,r)$ between the source s and receiver r can be written as

$$t(s,r) = F(s,x_1,x_2,x_3,r) = F(x_0,x_1,x_2,x_3,x_4)\,, \tag{M.1.1}$$

where

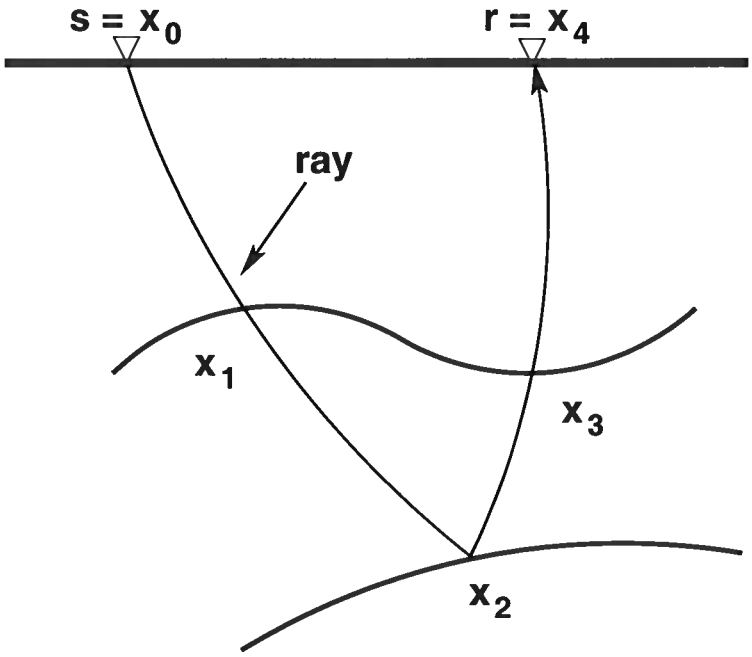

FIG. M.1. Two layer model. The layers are anisotropic and heterogeneous, and are separated by an irregular interface.

$$F(x_0, x_1, x_2, x_3, x_4) = \sum_{i=1}^{4} t_i(x_{i-1}, x_i)\,, \tag{M.1.2}$$

x_i define the intersections between the rays and the layer boundaries ($s = x_0$ and $r = x_4$), and t_i is the traveltime in the $i - th$ layer.

From Fermat's principle, the ray trajectory must correspond to an extremum of all possible paths between the source and receiver. Thus

$$\frac{\partial F}{\partial x_j} = 0, \tag{M.1.3}$$

where $j = 1, 2, 3$. Fermat's principle allows to express derivatives of $t(s, r)$ recorded at the surface of the earth in terms of traveltime derivatives of the individual layers.

Consider the derivative $\frac{\partial^2 t}{\partial s \partial r}$ (Gritsenko, 1984; Blyas, Gritsenko and Chernyak, 1984).

Differentiating equation (M.1.3) with respect to the source location s

$$\frac{\partial^2 F}{\partial s \partial x_j} = \sum_{l=0}^{4} \frac{\partial^2 F}{\partial x_l \partial x_j} \frac{\partial x_l}{\partial s}. \tag{M.1.4}$$

Expanding equation (M.1.4) gives

$$\frac{\partial^2 F}{\partial x_1 \partial x_j} \frac{\partial x_1}{\partial s} + \frac{\partial^2 F}{\partial x_2 \partial x_j} \frac{\partial x_2}{\partial s} + \frac{\partial^2 F}{\partial x_3 \partial x_j} \frac{\partial x_3}{\partial s} = -\frac{\partial^2 F}{\partial x_j \partial s}. \tag{M.1.5}$$

Then

$$\begin{aligned}
\frac{\partial^2 F}{\partial x_1 \partial x_1} \frac{\partial x_1}{\partial s} + \frac{\partial^2 F}{\partial x_2 \partial x_1} \frac{\partial x_2}{\partial s} + \frac{\partial^2 F}{\partial x_3 \partial x_1} \frac{\partial x_3}{\partial s} &= -\frac{\partial^2 F}{\partial x_1 \partial s} \\
\frac{\partial^2 F}{\partial x_1 \partial x_2} \frac{\partial x_1}{\partial s} + \frac{\partial^2 F}{\partial x_2 \partial x_2} \frac{\partial x_2}{\partial s} + \frac{\partial^2 F}{\partial x_3 \partial x_2} \frac{\partial x_3}{\partial s} &= 0 \\
\frac{\partial^2 F}{\partial x_1 \partial x_3} \frac{\partial x_1}{\partial s} + \frac{\partial^2 F}{\partial x_2 \partial x_3} \frac{\partial x_2}{\partial s} + \frac{\partial^2 F}{\partial x_3 \partial x_3} \frac{\partial x_3}{\partial s} &= 0.
\end{aligned} \tag{M.1.6}$$

On the other hand, using the chain-rule, the derivative $\frac{\partial^2 t}{\partial s \partial r}$ can be expressed as follows

$$\frac{\partial^2 t}{\partial s \partial r} = \frac{\partial^2 t_4}{\partial r \partial x_3} \frac{\partial x_3}{\partial s}. \tag{M.1.7}$$

Thus in equation (M.1.7), we need to express $\frac{\partial x_3}{\partial s}$ in terms of traveltime derivatives of the individual layers. This can be achieved by solving the system of equations (M.1.6). Solving this system, we obtain

$$\frac{\partial x_3}{\partial s} = \left(\frac{\frac{\partial^2 F}{\partial x_3 \partial x_2}}{\frac{\partial^2 F}{\partial x_3 \partial x_3}} \right) \left(\frac{\frac{\partial^2 F}{\partial x_1 \partial s}}{\frac{\partial^2 F}{\partial x_1 \partial x_1}} \right) \left(\frac{1}{\left(\frac{\frac{\partial^2 F}{\partial x_1 \partial x_2}}{\frac{\partial^2 F}{\partial x_1 \partial x_1}} \right) - \left(\frac{\frac{\partial^2 F}{\partial x_2 \partial x_3}}{\frac{\partial^2 F}{\partial x_2 \partial x_1}} \right) \left(\frac{\frac{\partial^2 F}{\partial x_2 \partial x_2}}{\frac{\partial^2 F}{\partial x_2 \partial x_3}} - \frac{\frac{\partial^2 F}{\partial x_3 \partial x_2}}{\frac{\partial^2 F}{\partial x_3 \partial x_3}} \right)} \right). \tag{M.1.8}$$

Substituting equation (M.1.8) into (M.1.7), gives

$$\frac{\partial^2 t}{\partial s \partial r} = \frac{\frac{\partial^2 t_4}{\partial r \partial x_3}\left(\frac{\frac{\partial^2 F}{\partial x_3 \partial x_2}}{\frac{\partial^2 F}{\partial x_3 \partial x_3}}\right)\left(\frac{\frac{\partial^2 F}{\partial x_1 \partial s}}{\frac{\partial^2 F}{\partial x_1 \partial x_1}}\right)}{\left(\frac{\frac{\partial^2 F}{\partial x_1 \partial x_2}}{\frac{\partial^2 F}{\partial x_1 \partial x_1}}\right) - \left(\frac{\frac{\partial^2 F}{\partial x_2 \partial x_3}}{\frac{\partial^2 F}{\partial x_2 \partial x_1}}\right)\left(\frac{\frac{\partial^2 F}{\partial x_2 \partial x_2}}{\frac{\partial^2 F}{\partial x_2 \partial x_3}} - \frac{\frac{\partial^2 F}{\partial x_3 \partial x_2}}{\frac{\partial^2 F}{\partial x_3 \partial x_3}}\right)}. \tag{M.1.9}$$

In the case of higher order mixed derivatives, a similar technique can be applied (Blyas et al., 1984).

The method described above can be used to obtain the azimuthally varying quartic coefficient for layered media. Thus, the quartic coefficient can be combined with the NMO ellipse to invert for the medium parameters in an efficient way. The main advantage of this combination is that it is necessary to trace only the zero-offset ray to reconstruct the azimuthally varying NMO velocity and quartic coefficient.

The approach illustrated above can also be used to model the moveout of converted waves (C-waves).